Doctoral Dissertation

Development of FSW and LFW Joints with High Ductile and Fatigue Strength for Weathering Steels

(耐候性鋼に対する高い延性と疲労性能を達成する

FSW および LFW 継手の開発)

WANG YIXUN

June 2022

Division of Global Architecture,
Graduate School of Engineering,
Osaka University

Abstract

Corrosion is one of the most severe diseases in engineering, which brings about significant damage to the safety and durability especially for steel bridges, and causes huge economic losses. Weathering steel has been developed and widely used to improve the anti-corrosion performance of steel bridges in harsh environment, while the high wt.% P in weathering steels often result in solidification cracks if joined by conventional fusion welding technologies. The friction stir welding (FSW) and linear friction welding (LFW) can join steels at low temperature (as low as A_1), which are expected to inhibit the P segregation and solidification cracks. The main purpose of this study is to investigate the possibility of joining the high wt.% P weathering steels by FSW and LFW, and ensure no solidification cracks. The microstructure, residual stress, geometry characteristics, ductile properties and fatigue strength of FSWed and LFWed weathering steels are studied to serve as a reference in structural design.

This study is composed of six chapters as follows:

(1) In Chapter 1, a brief overview of weathering steels, including the development history, mechanism to protect steel structures from corrosion, and limitations to be applied in the real engineering was presented. The welding process of friction welding was also introduced to highlight its advantages of joining weathering steels with high wt.% P. A state-of-art of review on microstructure and mechanical properties of conventional steels joined by FSW and LFW was conducted. The problems and challenges of joining high wt.% P weathering steels were summarized, and the originalities and objectives of this study were introduced.

(2) In Chapter 2, the optimization process of FSW and LFW parameters to achieve the target welding temperature and welded joints with no defects was introduced. The welding parameters of FSW and LFW to join conventional weathering steels (SMA490AW and SPA-H) at low temperature were first proposed. The new weathering steels (Steel1, Steel2 and Steel3) with higher wt.% P were developed and also joined by FSW after the successful joining of conventional weathering steels. The anti-corrosion properties of conventional and high-phosphorus weathering steels

assessed by the corrosion resistance index were Steel3 > Steel2 > SPA-H > Steel1 > SMA490AW. The experimental procedure to measure and test the residual stress, geometry, metallography, ductile properties and fatigue strength was described. The mechanism and accuracy of measuring methods were also explained. The global and local strain was measured by digital image correlation (DIC) method in this study, featuring a spatial resolution of about 7.1×10^{-3} mm^2/pixel and 1.1×10^{-5} mm^2/pixel, respectively.

(3) In Chapter 3, the conventional weathering steels SMA490AW and SPA-H were successfully joined by FSW below the A_1 temperature. The geometry and residual stress of FSW joints were measured, and the basin-shaped weldment with fine-grained ferrite and strengthening phase cementite was observed by scanning electron microscope (SEM). The high microhardness was measured at the weldment without heat affected zone (HAZ) softening. The yield and fracture characteristics of FSW joints under the monotonic loading were monitored by DIC, and the FSW joints experienced two steps of yield due to the high microhardness of weldment. The yield and fracture mechanisms were explained with the aid of finite element method (FEM). The joint efficiency of FSWed SMA490AW and SPA-H was as high as 100%. The fatigue tests were conducted on the FSW and BM specimens under a stress ratio of 0.1. The base metal (BM) and FSW specimens of weathering steels had almost identical fatigue strength due to the absence of HAZ softening and notches, indicating a favorable weldability. The fatigue strength of the FSW joints was higher than the design curve FAT112. The ratcheting behaviors and strain accumulation in different welded regions of FSW joints were also analyzed.

(4) In Chapter 4, the new weathering steels with higher wt.% P, *i.e.*, stronger anti-corrosion performance, than conventional weathering steels, were developed and also successfully joined by FSW below the A_1 temperature. The FSW joints with no solidification cracks and HAZ softening were obtained for all steels. Influence of wt.% P and other alloying elements on the microstructure characteristics and microhardness of FSW joints was discussed. Specifically, the increasing of wt.% P improved the microhardness and strength of the FSW joints but weakened the ductile elongation.

The solid solution of alloying elements (Ni, Cr and Nb) into the ferrite could enhance the ductile elongation and mechanical strength at the same time. The monotonic and fatigue tests showed that FSW could achieve a joint efficiency of 100% for three new weathering steels with high wt.% P. The fatigue strength of FSW and BM specimens was almost the same because the fatigue fracture occurred at the BM region of the FSW specimens. The ductile and fatigue tests were also conducted on the FSW joints with solidification cracks due to the inadequate welding parameters. The weld defects resulted in the fatigue fracture at the weld nugget and decreased the fatigue life by as long as 14.7 times, but they barely had no influence on the tensile strength.

(5) In Chapter 5, the conventional weathering steels SMA490AW and SPA-H were successfully joined by LFW above the A_3 temperature. The residual stress was measured and compared to other conventional steels joined by LFW, thus a general residual stress distribution of LFW joints was proposed. The stress concentration corresponding to various flash shapes and plate thickness was assessed by FEM. The microstructure of LFW joints was observed and its influence on the microhardness was discussed. Specifically, due to the higher welding temperature than FSW, the bainites with high microhardness were formed at the weld center zone (WCZ) of LFW joints. The area fraction of the bainites was obviously decreased and that of the ferrites was increased at a very small distance from the WCZ, indicating a large welding temperature gradient. The monotonic test was conducted on the finely polished and as-welded LFW specimens, and the yield and fracture characteristics were monitored and compared with the aid of DIC. Similar to the FSW joints, the LFW joints also experienced two steps of yield. The tensile strength of polished and as-welded specimen was very close to that of BM, resulting in a joint efficiency close to 100%. The fatigue test was also conducted on the finely polished and as-welded LFW specimens, and the influence of flash shape on the fatigue strength was discussed. The fatigue strength of the polished LFW specimens was close to that of the BM specimens and much higher than the design curve, while that of the as-welded LFW specimens was greatly decreased due to the local stress concentration. In addition, the possible unbonded flash at the edge caused the quick crack initiation and propagation at the

weld interface, and it is suggested to remove the flash near the edge to ensure the high fatigue strength.

(6) Chapter 6 summarized the main works and conclusions of this research. The further works that might promote the application of FSWed and LFWed weathering steels to the steel structures were also proposed.

Table of Contents

List of Abbreviations and Symbols

Abbreviations

AOI	Area of interest
AS	Advancing side
ASTM	American Society for Testing and Materials International
BM	Base metal
DBTT	Ductile-to-brittle transition temperature
DIC	Digital image correlation
DRX	Dynamic recrystallization
EBSD	Electron backscatter diffraction
EDM	Electrical discharge machining
FAT	Fatigue strength
FEM	Finite element method
FSW	Friction stir welding
GMA	Gas metal arc
HAZ	Heat affected zone
IIW	International Institute of Welding
IPF	Inverse pole figure
JIS	Japanese Industry Standard
LFFW	Low force friction welding
LFW	Linear friction welding
MAG	Metal active gas
MIG	Metal inert gas
ND	Normal direction
RFW	Rotary friction welding
RS	Retreating side
SAW	Submerged arc welding
SCF	Stress concentration factor

SEM	Scanning electron microscope
SMAW	Shielded metal arc welding
SZ	Stir zone
TD	Transverse direction
TIG	Tungsten inert gas
TMAZ	Thermo-mechanically affected zone
TWI	The Welding Institute
WCZ	Weld center zone
WD	Welding direction
XRD	X-ray diffraction

Symbols

a	Crack length
d	Grain size
F	Monotonic or fatigue load
f_1	Oscillation frequency of LFW
f_2	Loading frequency of fatigue experiment
H	Height of flash of LFW joints
Hv	Microhardness
I	Corrosion resistance index
K_t	Stress concentration factor
m	Slope of the S-N curve
N_f	Fatigue fracture life
n	Fatigue loading cycles
P	Applied pressure of LFW
Pr	Confidence interval
R	Stress ratio
R_a	Roughness
t	Plate thickness
U	Oscillation amplitude of LFW
u	Displacement of chucks during the monotonic or fatigue loading
Y	Distance from the weld center
α	Angular distortion
$\Delta\sigma$	Stress range
δ	Eccentric misalignment
ε_F	Elongation
ε_n	Nominal strain
ε_p	Plastic strain
ε_t	True strain measured by DIC
η	Pearlite contents

ρ	Weld toe radius
σ_B	Tensile strength
σ_n	Nominal stress
$\sigma_{R,TD}$	Residual stress perpendicular to the welding direction of FSW joints
$\sigma_{R\text{-}X}$	Residual stress in the X directions of LFW joints
$\sigma_{R\text{-}Y}$	Residual stress in the Y directions of LFW joints
σ_t	True stress
σ_{YU}	Upper yield stress
σ_y	Yield stress corresponding to 0.2% plastic strain

Chapter 1.

Introduction

1.1. Corrosion and weathering steel

1.1.1. Corrosion of steel bridge

Steel bridge is known for its light weight, rapid construction, favorable continuity and high bearing capacity [1-4], and has been widely applied in bridge engineering on highways, railways, and overpasses [5-6]. The world-renowned long-span bridges including the Tatara Bridge, Akashi Kaikyo Bridge, Jiangyin Yangtze River Bridge, Golden Gate Bridge, etc., are all steel bridges [7-10]. With the development of high performance structural steels, steel bridge is expected to achieve a longer span and stronger bearing capability, playing a more important role in infrastructure construction [11-12].

The long span bridges which cross the river, lake and ocean are often characterized by the steel structure [13-14]. As steel bridge is exposed to the harsh environment near the ocean or in the field, the durability is a significant factor to be considered in the bridge design [15-16]. The chemical and electric chemical reactions are prone to occur between the steel and surrounding media (such as water and salt), damaging the coating and resulting in the corrosion of steels [17-18]. The typical corroded surface of steel bridge is shown in Figure 1.1 [19-20]. Corrosion of steel bridge can give rise to direct and indirect economic losses, because a remarkable investment is required to prevent or delay further corrosion of steel bridge. It is reported that economic losses due to corrosion accounts for about 3.4% of gross domestic

product of countries around the world in 2016 [21].

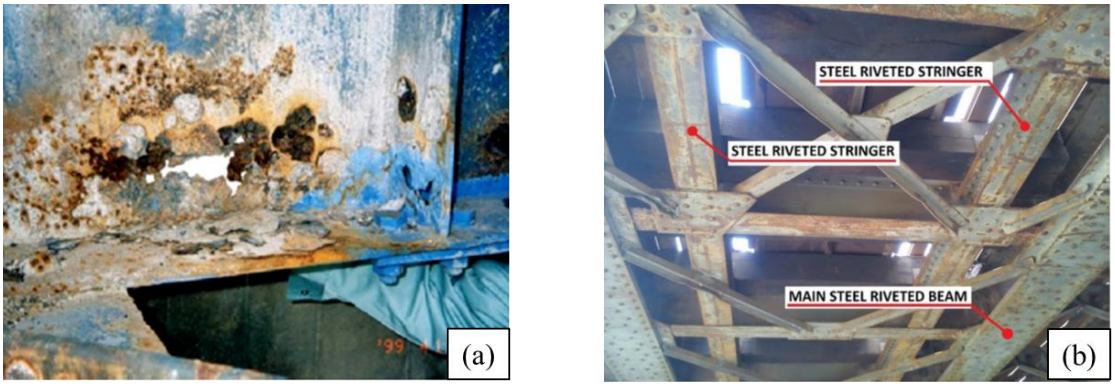

Figure 1.1 Typical corroded surface of steel bridge (a) corroded web and stiffener [19]; (b) corroded truss and stringer [20]

In addition to economic losses, corrosion brings about serious damage to the safety and durability of steel bridge [22]. With increasing service years, corrosion of steel bridge inevitably occurs and causes losses of bearing capability [23]. Due to the reduction of plate thickness and local stress concentration, the crack initiation and propagation in steel bridge is accelerated under the cyclic loading such as vehicles and wind, resulting in the structure fracture [24-25]. Some security incidents of steel bridge due to corrosion are listed below to show the serious consequence of corrosion.

On December 15, 1967, the Silver Bridge in USA collapsed under the weight of rush-hour traffic as seen Figure 1.2(a), resulting in the deaths of 46 people. A small crack formed in a single eye-bar due to the stress corrosion, which was the source of this catastrophe. The collapse of the Silver Bridge led to the intensified inspection protocols and numerous replacements of old bridges in USA [26]; The I-35W Mississippi River Bridge also in USA had a catastrophic failure during the evening rush hour on August 1, 2007 as seen Figure 1.2(b), killing 13 people and injuring 145. Corrosion and fatigue cracks in its bearings and girders were reported before the collapse, while this tragedy still failed to be prevented [27]; The world-renowned London Tower Bridge was forced to close for up to six months in June, 1993 to repair corroded steel girders under its two main towers. Corrosion and the daily volume of 40,000 vehicles weakened the service life of this 99-year-old bridge, originally designed for

horse, carriages and pedestrians [28]; The cables of Köhlbrand Estuary Bridge in Germany were forced to be completely replaced due to the serious corrosion and breakage of wires after only three years of operation [29]. The construction cost was increased by three times compared to the original budget. Above all, corrosion of steel bridge poses a great threat to the safe operation of steel bridge and causes a large economic investment.

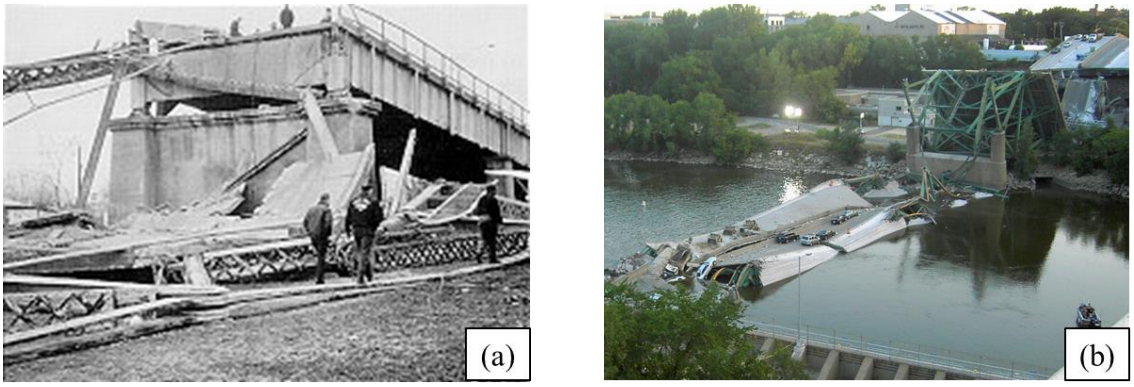

Figure 1.2 Collapse of steel bridges due to corrosion (a) Silver Bridge [30] (b) I-35W Mississippi River Bridge [31]

The conventional method to prevent the corrosion of steel bridge is to coat on the steel surface [32]. Since the first application of coating to steel bridge in 18th century, coating is still one of the most effective way to protect steel bridge from corrosion nowadays [33]. The alkyd coating material was widely used before 1960s, after which zinc-rich coating was prevalent because a longer anti-corrosion life can be achieved [34]. Coating plays an important role in protecting steel bridges from harsh environment [35-36], while the coating diseases such as chalking, cracking, rusting and falling off are often observed due to the long-term oxidation [37-38]. The base metal is directly exposed to the moisture, oxygen and corrosive medium (such as impurities, dust, deposits, etc.) after the failure of coating, resulting in a fast corrosion and significant loss of bearing capacity [39-40]. Therefore, in addition to developing coating technology which can contribute to a higher anti-corrosion performance and longer service life, the anti-corrosion property of steel itself should also be improved in case the coating fails.

1.1.2. Development of weathering steel

Weathering steel was originally developed to increase the anti-corrosion performance of steel so that steel bridge itself can have the strong anti-corrosion property without coating [41-43]. Compared to conventional structural steel, weathering steel has a higher amount of alloying elements including the Cu, Cr, P, etc., so that a dense rust layer can easily form on the steel surface as seen in Figure 1.3, which protects itself from further corrosion [44-45]. The illustration of corrosion rate of weathering steel compared to that of common steel is shown in Figure 1.4. Curve A-B-C shows the relationship of corrosion weight to corrosion time of weathering steel, and curve A-B'-C' is common steel. It is observed that a large amount of rust accumulates from exposure time A to B (also A to B'), while the slope of curve B-C (also B'-C') is obviously decreased, indicating that the generation of rust is slowed down. But the corrosion rate of common steel at curve B'-C' is much higher than that of weathering steel at curve B-C. This phenomenon indicates that weathering steel has a much more favorable anti-corrosion performance than common steel.

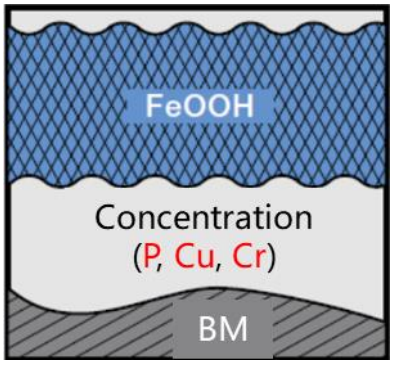

Figure 1.3 Dense rust formed on the steel surface [46]

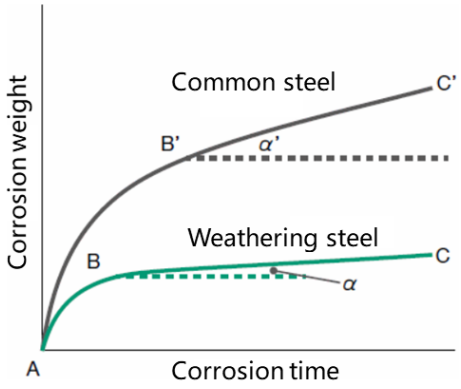

Figure 1.4 Relationship of corrosion weight to corrosion time for weathering steel and common steel [46]

Weathering steel was first developed by the United States Steel Corporation in 1933 by the trademark of COR-TEN [47]. The name COR-TEN refers to the high anti-corrosion performance and high tensile strength of this steel [48]. Weathering indicates that these steels

are allowed to rust in order to form the protective coating, which exhibits increased resistance to atmospheric corrosion compared to other steels [49]. Since invention of weathering steel by the United States Steel Corporation, the manufacturing was introduced to countries around the world [50]. The industry standards concerning the manufacturing and application of weathering steel have also been established. For example, the weathering steels are a family of American Society for Testing and Materials International (ASTM) specifications, named by A588, A242, A606-4, A847, A871-65 and A709-50W [51-56]. The Japanese Industry Standard (JIS) stipulates the weldable weathering steel SMA490 series and non-weldable SPA-H series for steel structure [57]. The NH series of weathering steel used in China cover structural steels with yield strength ranging from 345 MPa to 550 MPa [58]. Weathering steel is now popularly used in bridge engineering, marine transportation, architecture, sculpture, etc. [59]. The New River Gorge Bridge illustrated in Figure 1.5 is one of the highest vehicular bridges in the world. It is made from COR-TEN steel, which presented the notable challenge to ensure the welded joints weathered at the same rate as the rest of the steel [60].

Figure 1.5 The New River Gorge Bridge [60]

The higher amount of alloying elements including the Cu, Cr, P, etc., contributes to a dense rust on the steel surface. The contradiction is that the increase of alloying elements weakens the weldability of the steel, and the solidification hot crack has a higher possibility to occur due to the segregation of P and S as seen Figure 1.6 (weathering steel with 0.1%P joined by TIG) [61]. The solidification crack, which might have limited influence on the tensile strength of the

weld, drastically decreases the fatigue life of the welded joints, as there is often a high stress on the crack tip [62]. The crack initiation, which covers a high proportion of fatigue life, is skipped due to the existence of the solidification crack, and the fast crack propagation begins as soon as the cyclic loading is applied [63]. To prevent the solidification crack of weathering steel during the welding, the content of the alloying elements is strictly controlled, as are the heat input and plate thickness [64]. The existing weathering steels which can be used for welding usually have a wt.% P smaller than 0.035% according to the JIS [57]. Further, the weathering steels which are not developed for welding, are stipulated to have a wt.% P smaller than 0.15%.

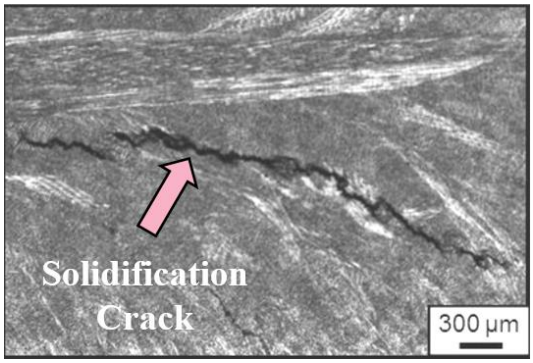

Figure 1.6 Solidification crack of weathering steel with 0.1% P by TIG [61]

So far, the microstructure and mechanical properties of weathering steels welded by the conventional welding methods including the metal inert gas (MIG) welding [65], tungsten inert gas (TIG) welding [66], metal active gas (MAG) welding [67], etc., have been widely studied. Ravikumar [68] studied the CortenA steel welded by TIG with different welding parameters. The optimized welding parameters were suggested and the TIG was proved to provide better welding performance than MIG. The influence of post heat treatment on the weld quality of CortenA and CortenB steel by MAG welding was investigated by Vairamani [69]. The ductility and strength were compared between Corten steels with different grades, and no defects occurred in the weld based on the proposed welding procedure. Kondo [70] compared the corrosion performance and fatigue properties of the fillet welded joints made of SMA490 weathering steel and SM490 common steel under the same exposure corrosion environment. The corrosion pit of the common steel illustrated larger depth than the weathering steel, which

resulted in the obvious reduction of fatigue life. The wt.% P of above - mentioned weathering steels are strictly controlled. For the steel bridges in the corrosive environment like the offshore, the existing weathering mild steels might fail to meet the requirements of anti-corrosion property due to the limit of wt.% P and other alloying elements.

However, a stronger durability of steel bridges requires a stronger anti-corrosion performance of weathering steel. In other words, weathering steel is supposed to have a higher wt.% P and other alloying elements while no occurrence of the solidification crack should be guaranteed after welding, which is a great challenge for the conventional fusion welding technologies.

1.2. Friction welding technologies

1.2.1. Development history

Friction welding is a solid-state welding process that generates heat through mechanical friction between welding pieces in relative motion to one another [71-73]. The materials near the weld interface are plasticized and joined together under a certain pressure [74-75]. Because no melting occurs, friction welding is not a fusion welding process, but a solid-state welding technique [76-77]. Friction welding can be used to join a wide variety of metals and thermoplastics, and widely applied in aviation and automotive industries [78-79]. In recent years, reports of friction welding to join structures in the civil engineering are also found [80-81]. It is the essence of solid-state joining of friction welding that provides a more promising way to join weathering steels, because the P segregation is possible to be inhibited under the low welding temperature, so as to prevent the occurrence of the solidification crack.

The invention of friction welding can be dated back to the early 20th century when the Rotary Friction Welding (RFW) was developed as seen in Figure 1.7, but the first description and experiments related to RFW took place in 1956 [82]. W. Richter patented the method of Linear Friction Welding (LFW) process in 1924 in England and 1929 in Germany [83].

However, the description of the process was vague and H. Klopstock proposed the same process in the USSR 1924 [84]. Another friction welding technology named Friction Stir Welding (FSW) was invented and experimentally proven by The Welding Institute (TWI) in the UK and patented in 1991, which uses a non-consumable tool to join two facing workpieces [85-86]. An improved modification of the conventional friction welding is named Low Force Friction Welding (LFFW) [87], which uses an external energy source to raise the interface temperature of the two workpieces to be joined, thereby reducing the process forces required to make a solid-state weld compared to traditional friction welding. The RFW has an advantage to join cylindrical components such as gas turbine, truck axles, piston rods, etc. [88-89], while it is difficult to join plates with a rectangular section, which greatly limits the further application of RFW in engineering. The welding process and characteristics of FSW and LFW which are less affected by the section shape will be elaborated in the following chapters.

Figure 1.7 Historical photo of rotary friction welding (RFW) [82]

Since the invention of friction welding, it has experienced continuous improvement and widely used in the industry and engineering nowadays. Friction welding can be used to build more favorable industrial rollers, tubes, and shafts [90-91]. The process is also used to join components for industrial printers, material handling equipment, as well as automotive, aerospace, marine, and oil applications [92-93]. Other examples of assemblies include engines, air valves, motors, wheel hubs, etc. [94-96].

1.2.2. Friction stir welding (FSW)

Friction stir welding (FSW), which was developed by TWI in 1991 [85-86], offers the great capability to join weathering steel with a lower heat input, compared to the conventional fusion welding techniques. FSW is a solid-state thermo-mechanical welding process, in which a rotating cylindrical welding tool moves along the welding region of the workpiece to be joined as seen in Figure 1.8 and Figure 1.9. The steel can be joined by FSW at a temperature below the melting point, characterized by high thermal efficiency, low residual stress and small distortion of the welded joints [97]. The weld formed by FSW is generally free of defects that are often observed in fusion welding [98]. The FSW process is also free of fumes and does not consume filler materials [99].

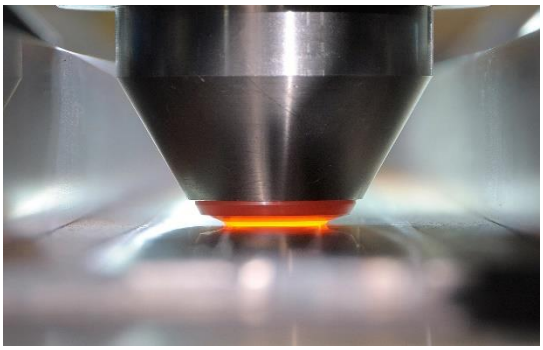

Figure 1.8 View of FSW [100]

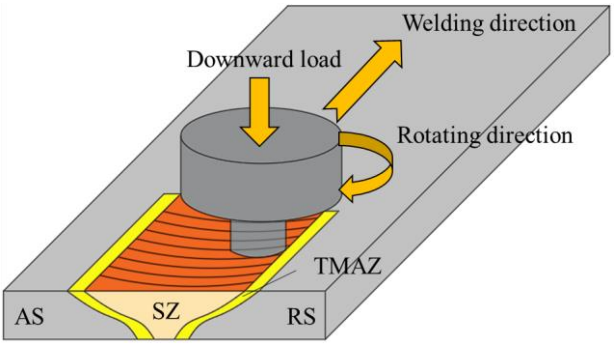

Figure 1.9 Welding process of FSW [101]

Since its invention, FSW has been widely used in soft alloys such as aluminum alloys and magnesium alloys in vehicle engineering and mechanical engineering [102]. In recent years, with the development of high-strength welding tools, the study of the FSW joined metals with high hardness such as steel has also been carried out. The first example of welding general steels without any transformation was successfully conducted by Fujii [103], and the control of the temperature enabled the steels to be welded in various regions. Just the same as fusion welding, the welding parameters have significant influence on the weld quality of FSW joints. Tiwari [104] optimized the welding parameters of low carbon steel joined by FSW. The FSW joints with high quality and poor quality are shown in Figure 1.10, which was controlled by the

rotating speed and welding speed.

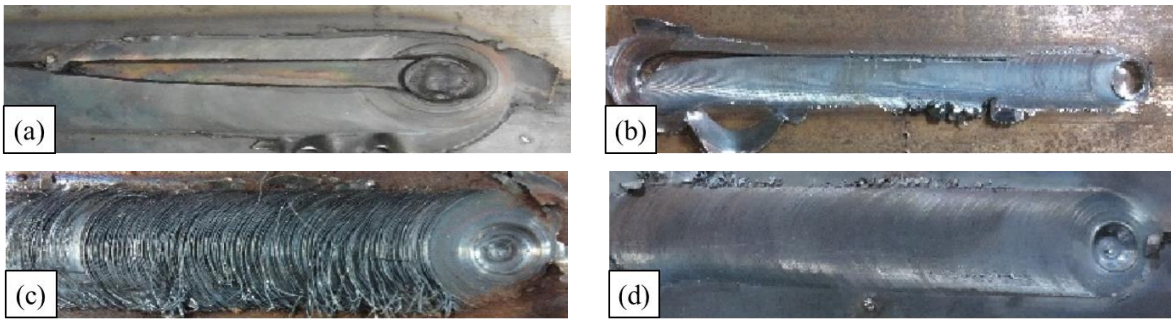

Figure 1.10 Appearance of FSW joints (a) poor quality due to excessive wear of tool pin; (b) poor quality due to improper consolidation; (c) poor quality due to excessive flash; (d) high quality [104]

So far, FSW is mainly used in industry to join soft metals such as Al, Mg, Ti, etc. The wide engineering application of FSW includes the shipbuilding, aerospace, railway, automotive and electronics. In recent years, application of FSW to civil engineering such as joining aluminum bridges is reported as seen Figure 1.11, indicating the great potential of FSW [105].

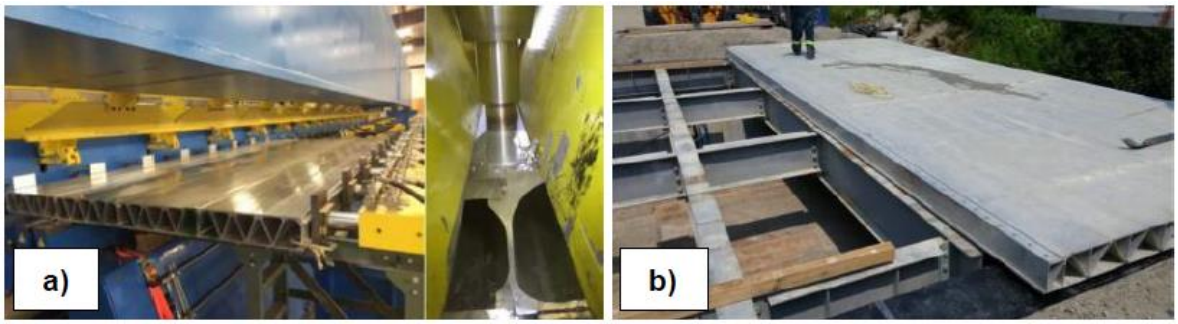

Figure 1.11 Aluminum bridge deck (a) extrusions joined by FSW (b) installation [105]

1.2.3. Linear friction welding (LFW)

The linear friction welding (LFW) is also a solid-state joining process as seen Figure 1.12 [106] and Figure 1.13 [107], which works by oscillating one sample to another under a high compressive force [108-109]. The interface materials are plasticized and joined together by the friction heats [106,110]. The process operates at a lower temperature than the fusion welding

[111], thus the P segregation can be inhibited. The factors have major influence on the weld quality and property of LFW joints include the applied pressure, oscillation frequency and amplitude. Figure 1.14 shows flash geometry of LFWed titanium alloys under various oscillation amplitudes, and it is obviously observed that the larger oscillation amplitude results in longer flash [109].

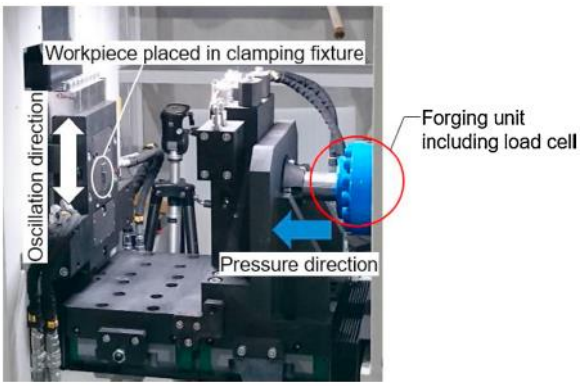

Figure 1.12 Setup of the workpiece in the LFW machine [106]

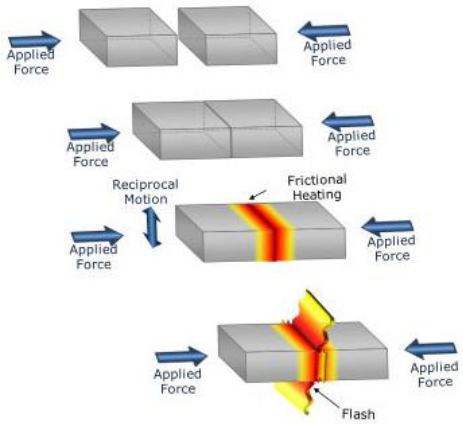

Figure 1.13 Welding process of LFW [107]

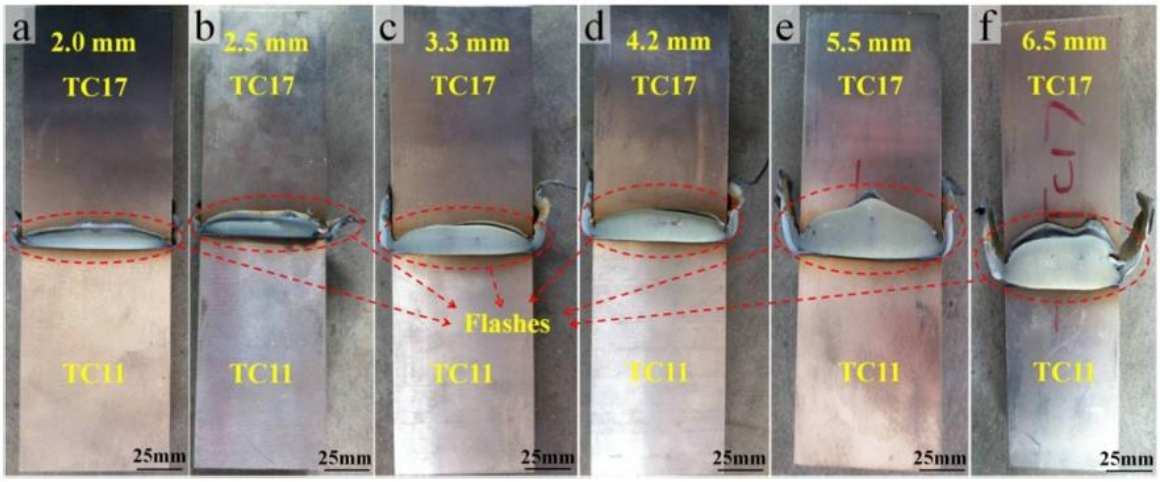

Figure 1.14 Flash geometry under different oscillation amplitudes (a) 2.0 mm; (b) 2.5 mm; (c) 3.3 mm; (d) 4.2 mm; (e) 5.5 mm; (f) 6.5 mm [109]

As a solid-state joining process, LFW can avoid many of the defects associated with the melting and solidification during the fusion welding [112-113]. Compared to the fusion welding and the FSW, the LFW requires no shielding gas and consumes no welding tool, also

making it a promising way to join the engineering structures and components. LFW was initially developed to join titanium alloys in aeroengines [114-116]. In recent years, the application of LFW has been extended to steels to explore new potentials.

1.3. Characteristics and properties of FSW and LFW joints

1.3.1. Microstructure

Different from fusion welding, the etched weld section of FSW joints usually shows a basin shape, which is shown in Figure 1.15. During the FSW process, the material is removed from the leading edge of the rotating side of the tool, which is in the traversing direction of the tool. This side of the weld is called the advancing side (AS). The extracted material is retrieved back into the weld zone at the other end of the rotating tool, which is opposite to the traversing direction and called the retreating side (RS) [102]. For convenience, the coordinates of FSW joints is usually defined by the normal direction (ND), transverse direction (TD) and welding direction (WD). The basin shape is consistent with the geometry of welding tool, as the area of tool shoulder on the top surface is larger than that of probe pin which is plunged into the bottom of workpieces.

Figure 1.15 Etched weld section of FSW joints [117]

Similar to the fusion welding, the FSW joints can also be divided into several distinct regions including the base metal (BM), stir zone (SZ), heat affected zone (HAZ). Besides, due to the combined effects of high temperature and shear strain on the boundary of welding tool, a narrow transition region is often found and named thermo-mechanically affected zone (TMAZ). As the welded joints have both advancing and retreating sides, the TMAZ and HAZ

can be furtherly divided into HAZ-AS, HAZ-RS, TMAZ-AS and TMAZ-RS. Sometimes HAZ is not obvious because welding temperature is low and growth of grain is inhibited. The friction heat is usually influenced by the tool shoulder geometry, downward load, tool rotation rate and welding speed. The various welding parameters often result in a wide range of temperature from below A_1 to above A_3, which furtherly have significant influence on the microstructures of FSW joints. The A_1 temperature refers to the temperature when austenite begins to crystallize from the ferrite during the heating or austenite completely transforms to the ferrite and pearlite during the cooling. The A_3 temperature refers to the temperature when ferrite begins to crystallize from the austenite during the cooling or ferrite completely transforms to the austenite during the heating. Figure 1.16 shows SZ of low carbon steel S12C joined by FSW above A_3, between A_3 and A_1, and below A_1. When S12C steel was welded at temperature above A_3, i.e., in the austenite single-phase region, the high temperature and lack of second phase resulted in the coarse grain with an average ferrite grain size of about 5 μm. For FSW joints of S12C steel welded in the austenite + ferrite two-phase region, the recrystallized austenite and ferrite grains worked as the second phase for each other. The ferrite grain was significantly refined and about 3 μm, which was even smaller than that joined below A_1 [118].

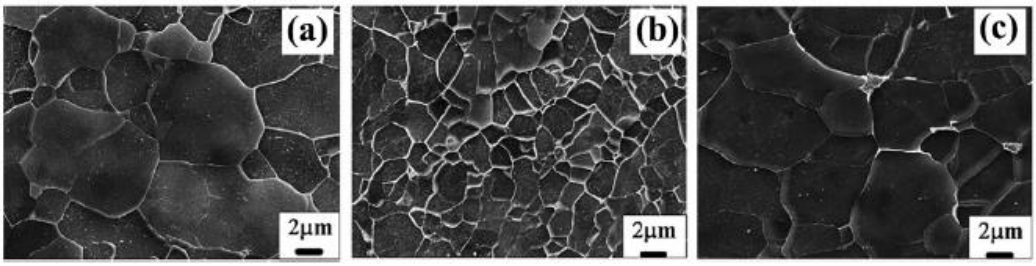

Figure 1.16 SZ of S12C steel joined by FSW (a) above A_3; (b) between A_3 and A_1; (c) below A_1 [118]

It has been concluded by many studies that the amount of strain and heat produced on AS is often higher than those on RS [119-120]. The different microstructures can often be observed for TMAZ-AS and TMAZ-RS. Figure 1.17 shows microstructure of TMAZ of FSWed AZ91 magnesium alloy [121]. It can be observed that TMAZ-AS, though very narrow, has a distinct border against BM and SZ. However, TMAZ-RS has a wider region and the inclined grains are

spread in a larger area. The border of TMAZ-RS against BM and SZ is not so clear as that of TMAZ-AS. One explanation for this phenomenon is that due to the higher strain and temperature on AS, the recrystallization occurs while the combination of strain and temperature is not effective enough for the recrystallization on RS.

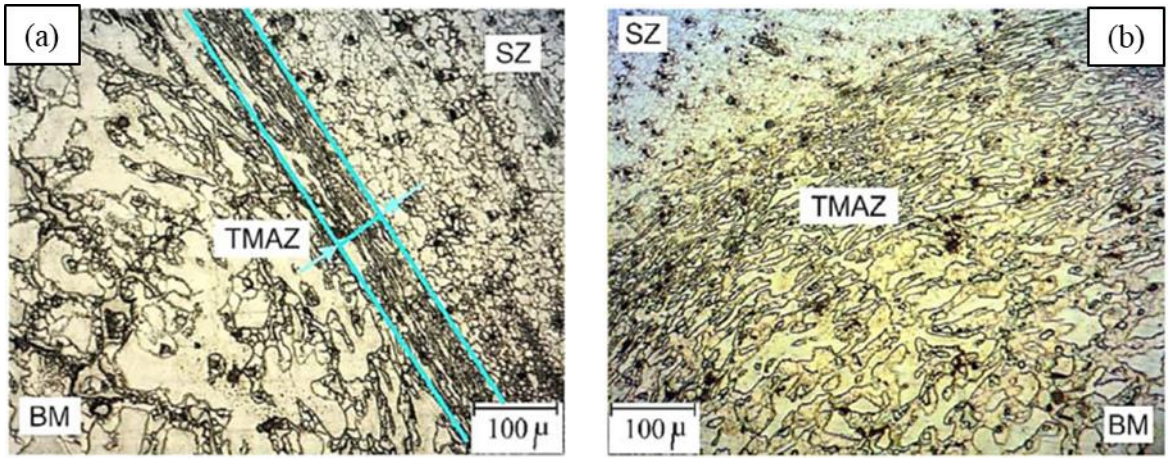

Figure 1.17 Microstructure of TMAZ on (a) AS and (b) RS [121]

The weldment of LFW joints is much narrower compared to conventional fusion welded joints due to the large temperature gradient, which is shown in Figure 1.18 [111]. Similar to FSW joints, the LFW joints can also be divided into several distinct regions including the BM, weld center zone (WCZ), HAZ and TMAZ. The various welding parameters often result in a wide range of temperature from below A_1 to above A_3, which furtherly have significant influence on the microstructures of LFW joints. According to current studies [122-123], the lower applied pressure induces a higher welding temperature, while the increasing oscillation frequency and amplitude contribute to a higher welding temperature. Figure 1.19 shows the microstructure evolution of LFW joints of a medium carbon steel from WCZ to BM under various welding parameters [122]. It is observed that weldment width of five LFW joints is no more than 2.0 mm. The area fraction of strengthening phase such as martensite and cementite is significantly decreased even with a very small distance from the weld center. A large area fraction of martensite accompanied with ferrite is observed under the high oscillation frequency and low applied pressure for Joint1 and Joint4. The martensite transformation was completely suppressed for Joint5 fabricated at 15 Hz and 400 MPa. The equiaxed ferrite grains

accompanied with uniformly distributed spherical cementite are observed at WCZ.

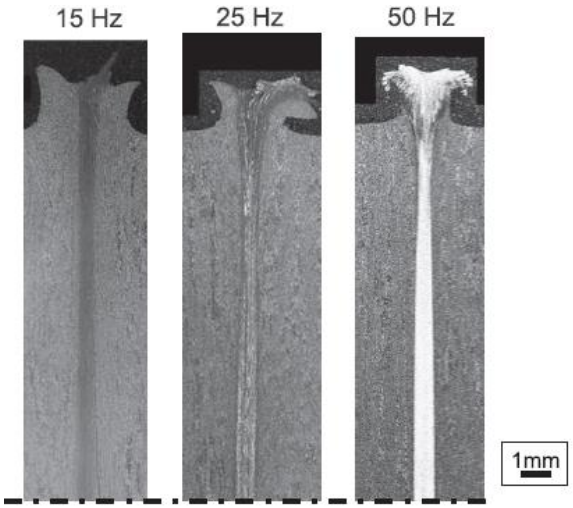

Figure 1.18 Etched weldment under different oscillation frequency [111]

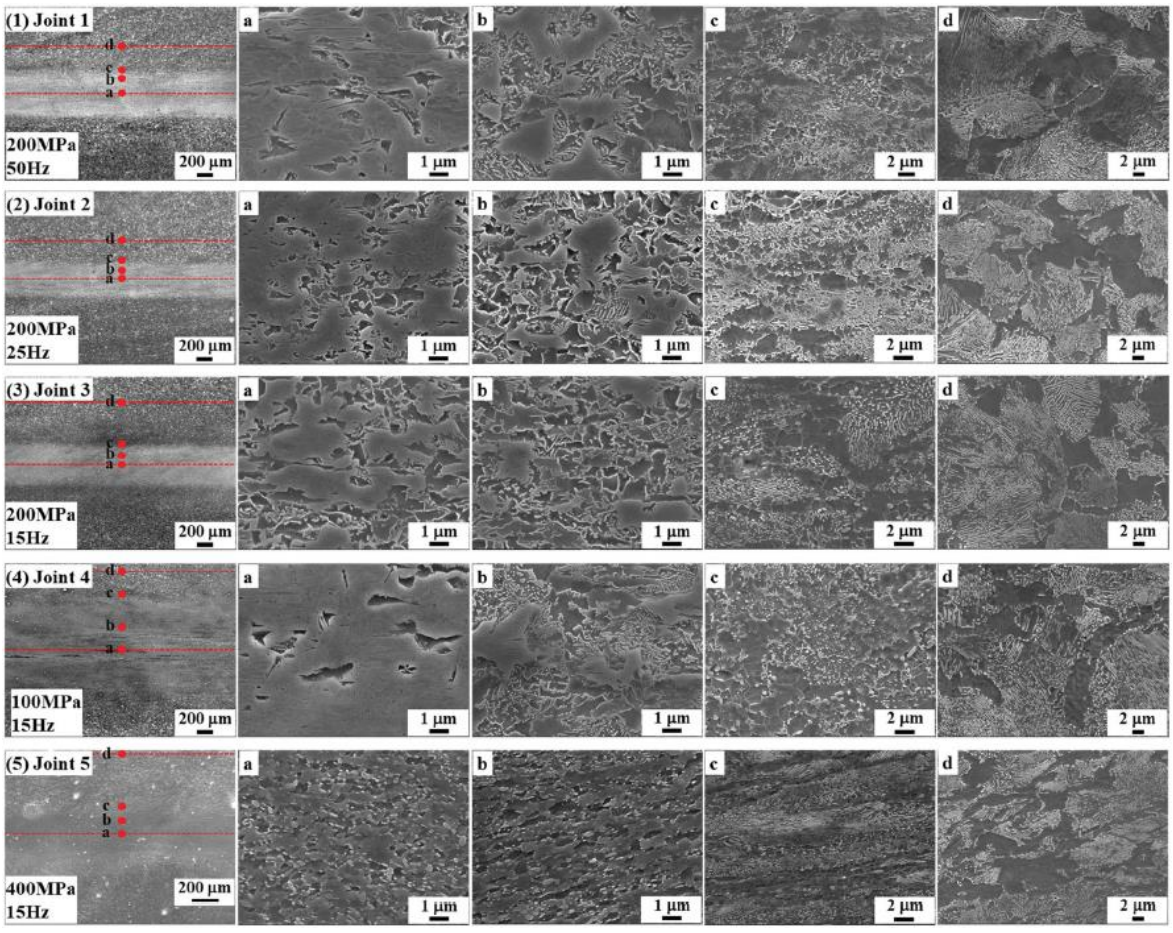

Figure 1.19 Microstructure from WCZ to BM under various welding parameters [122]

The crystallographic directions of LFW joints are significantly influenced by the effects of thermal-mechanical coupling. Figure 1.20 illustrates the electron backscatter diffraction

(EBSD) maps of BM, WCZ, HAZ and TMAZ of LFWed rail steel joints [124]. It is observed in Figure 1.20(c) and (d) that the microstructure of HAZ is very similar to that of BM with pearlite grains of bcc structure and a large number of low-angle grain boundaries. The WCZ in Figure 1.20(a) is composed of fine grains with the main crystal orientations of <101> and <001> due to the sufficient dynamic recrystallization. Figure 1.20(b) shows the grains of TMAZ which are smaller than those of BM and elongated along the shear direction under the combined thermal and mechanical effects.

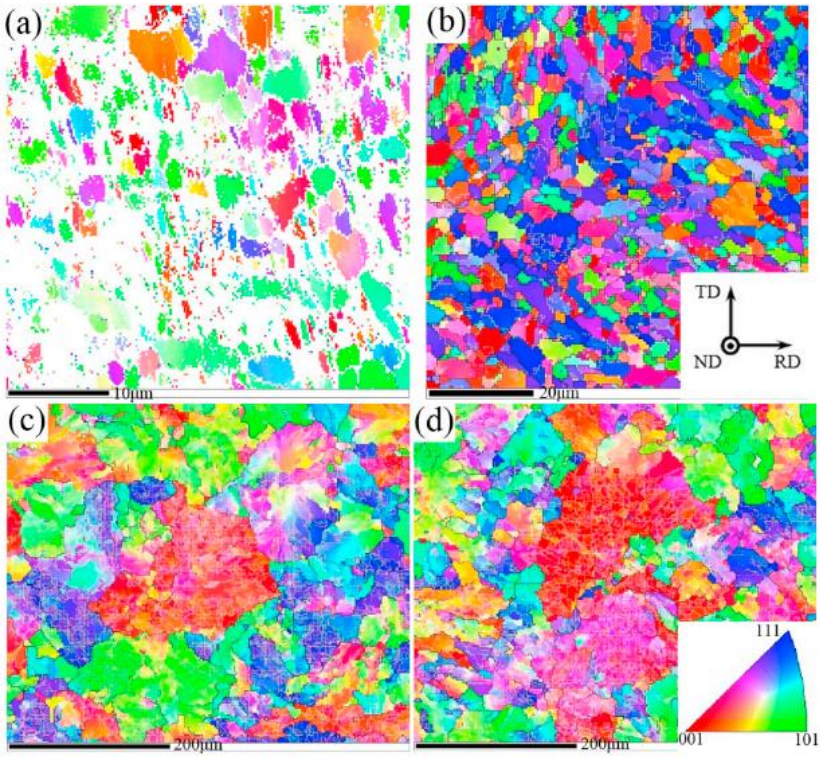

Figure 1.20 EBSD maps of LFWed rail steel joints (a) WCZ; (b) TMAZ; (c) HAZ; (d) BM [124]

1.3.2. Microhardness and residual stress

One of the most significant advantages of FSW and LFW is that the HAZ softening can be inhibited due to the low welding temperature. Although some reports of FSW joints with HAZ softening can still be found as seen Figure 1.21(a), FSW joints conducted under the

optimized welding parameters often show no HAZ softening as seen Figure 1.21(b) [125]. The basin-shaped high microhardness at SZ is consistent to the basin shape of etched weld section as seen Figure 1.15.

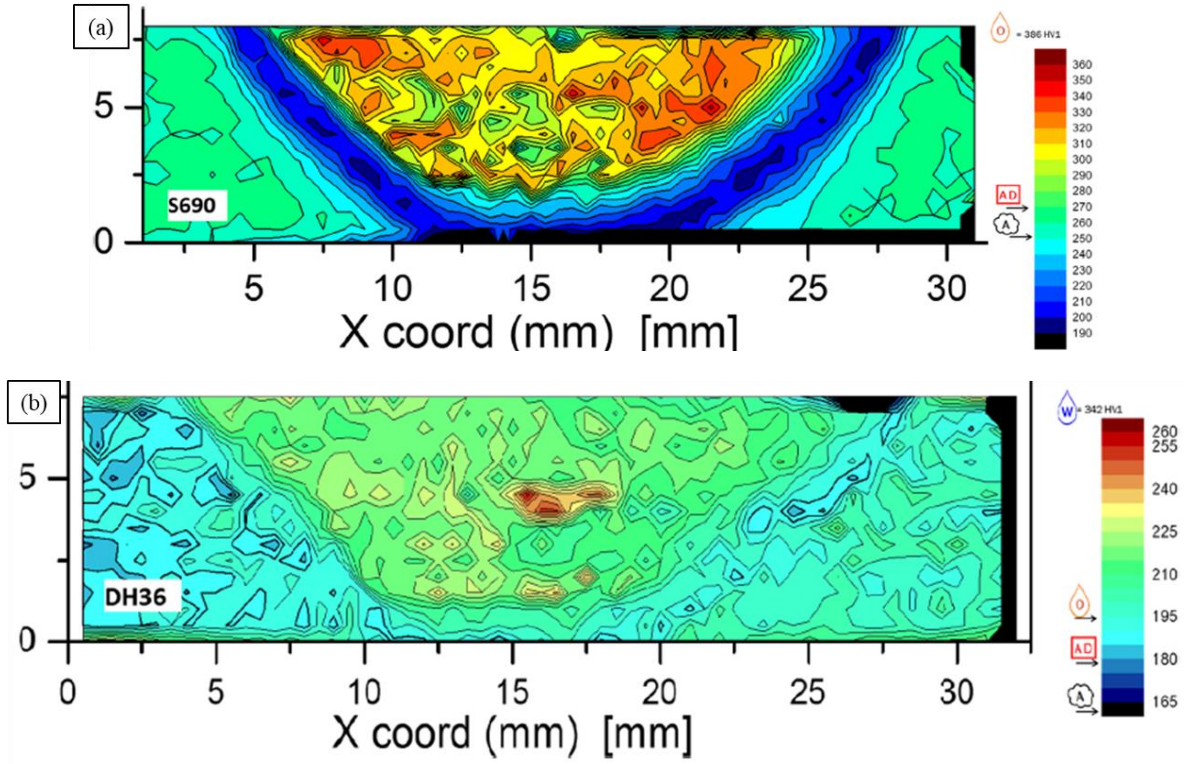

Figure 1.21 Microhardness of FSW joints (a) S690 steel with HAZ softening; (b) DH36 steel without HAZ softening [125]

The microhardness of a certain structural steel joined by autogenous TIG welding and FSW was compared by Chaurasia [126] and shown in Figure 1.22. For TIG joints in Figure 1.22(a), the microhardness of BM is approximately 135HV and the weld fusion zone illustrates a microhardness ranging from 180 - 200HV. However, the microhardness of HAZ varies from 170-180HV which is lower than weld fusion zone, indicating a HAZ softening. For FSW joints in Figure 1.22 (b), the maximum microhardness at SZ is close to that of TIG joints. A little higher microhardness is observed on AS than RS probably due to the higher heats on AS. The similar microhardness distribution for FSW joints is also reported by Sharma [127].

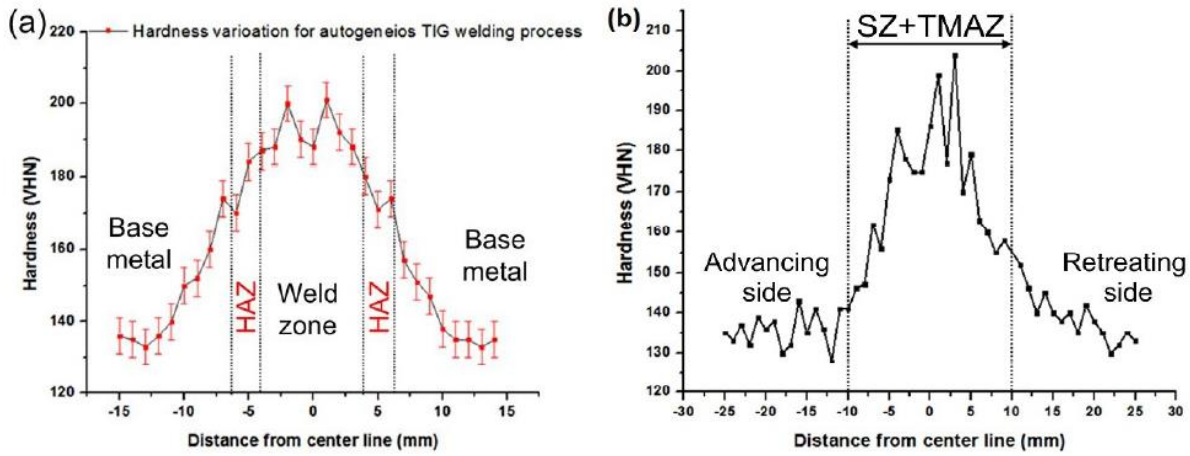

Figure 1.22 Microhardness distribution along the transverse direction (a) autogenous TIG welding; (b) FSW [126]

Due to the sharp temperature gradient and narrow weldment as seen in Figure 1.18, the microhardness of LFW joints often shows a rapid change from the WCZ to BM [111,122,128-129]. The welding parameters also have significant influence on the microhardness distribution. As seen in Figure 1.23 [122] which shows microhardness distribution of LFWed medium carbon steel, for case (50 Hz, 200 MPa), the WCZ consisting of a large area fraction of martensite is featured by very high microhardness. With decreasing frequency to 25 Hz and 15 Hz with constant applied pressure of 200 MPa, the microhardness also decreases. In the case of a constant frequency of 15 Hz and various pressures, the microhardness of SZ decreases with the pressure increasing. No obvious HAZ softening is observed for all welding conditions.

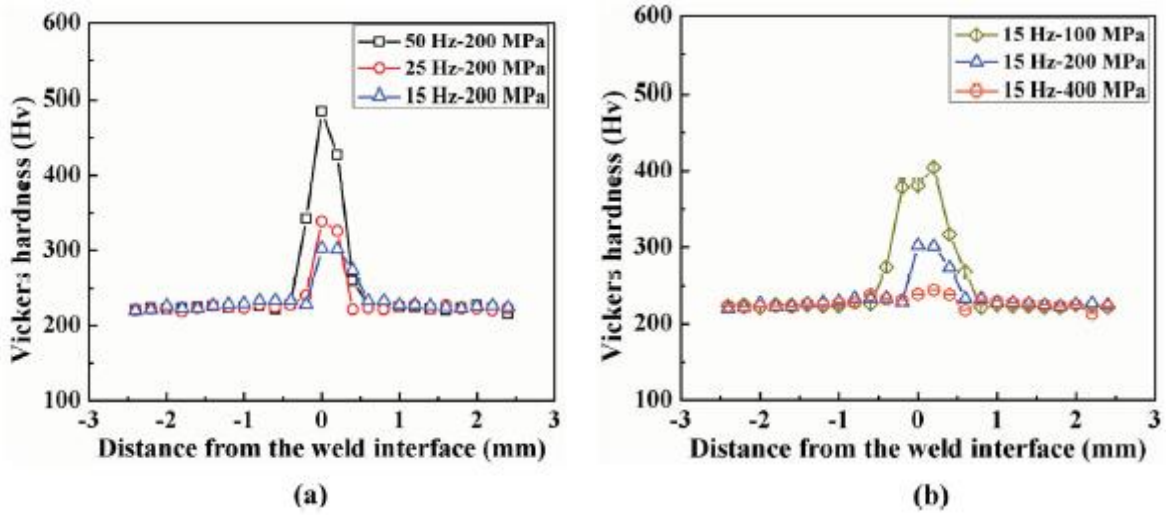

Figure 1.23 Influence of welding parameters on microhardness distribution of LFW joints

(a) oscillation frequency; (b) applied pressure [122]

The residual stress is one of the most significant factors having influence on the mechanical properties of welded joints. Various welding parameters can result in different residual stress distributions. Taking the 304L stainless steel joined by FSW as an example, the longitudinal and transverse residual stress under rotation speed of 300 and 500 rpm is shown in Figure 1.24 [130]. The distribution of longitudinal residual stress is typical of many fusion welding process in austenite stainless steels [131]. The region of high residual stress is wider for FSW joints joined at a rotation speed of 500 rpm than those at 300 rpm. The transverse residual stress is much lower than the longitudinal residual stress, which is similar to that of fusion welding.

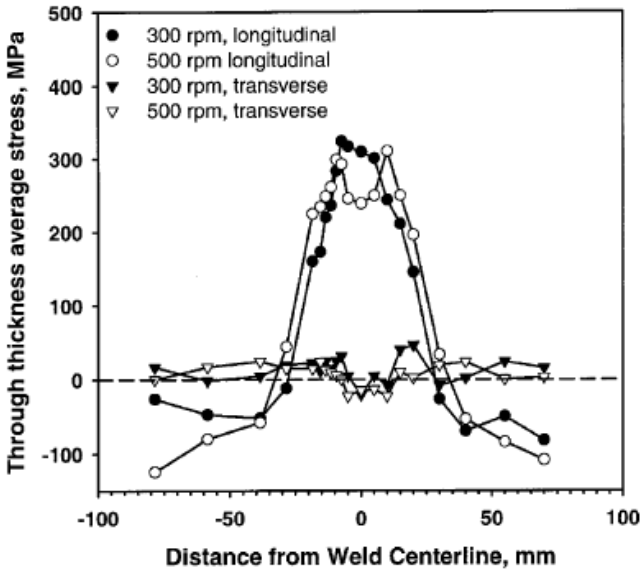

Figure 1.24 Longitudinal and transverse residual stress under rotation speed of 300 rpm and 500 rpm. [130]

The residual stress of transverse direction and welding direction of SUS490 steel corresponding to SZ, BM, TMAZ-AS and TMAZ-RS is also shown in Figure 1.25 [132]. The residual stress of BM can be neglected compared to the welded region, as the residual stress involved from the rolling process was removed due to the fully annealing in the step of heat treatment. The low tensile residual stress and high compressive residual stress were formed at

SZ, which is very different from the results of the TIG joint. The tensile residual stress is usually formed in the fusion zone of the TIG joint according to previous studies [133]. The residual stress distribution of TMAZ-AS and TMAZ-RS is quite different from that of SZ. The tensile residual stress was measured on TMAZ-RS near the surface, and the compressive residual stress on TMAZ-RS is larger than that on TMAZ-AS.

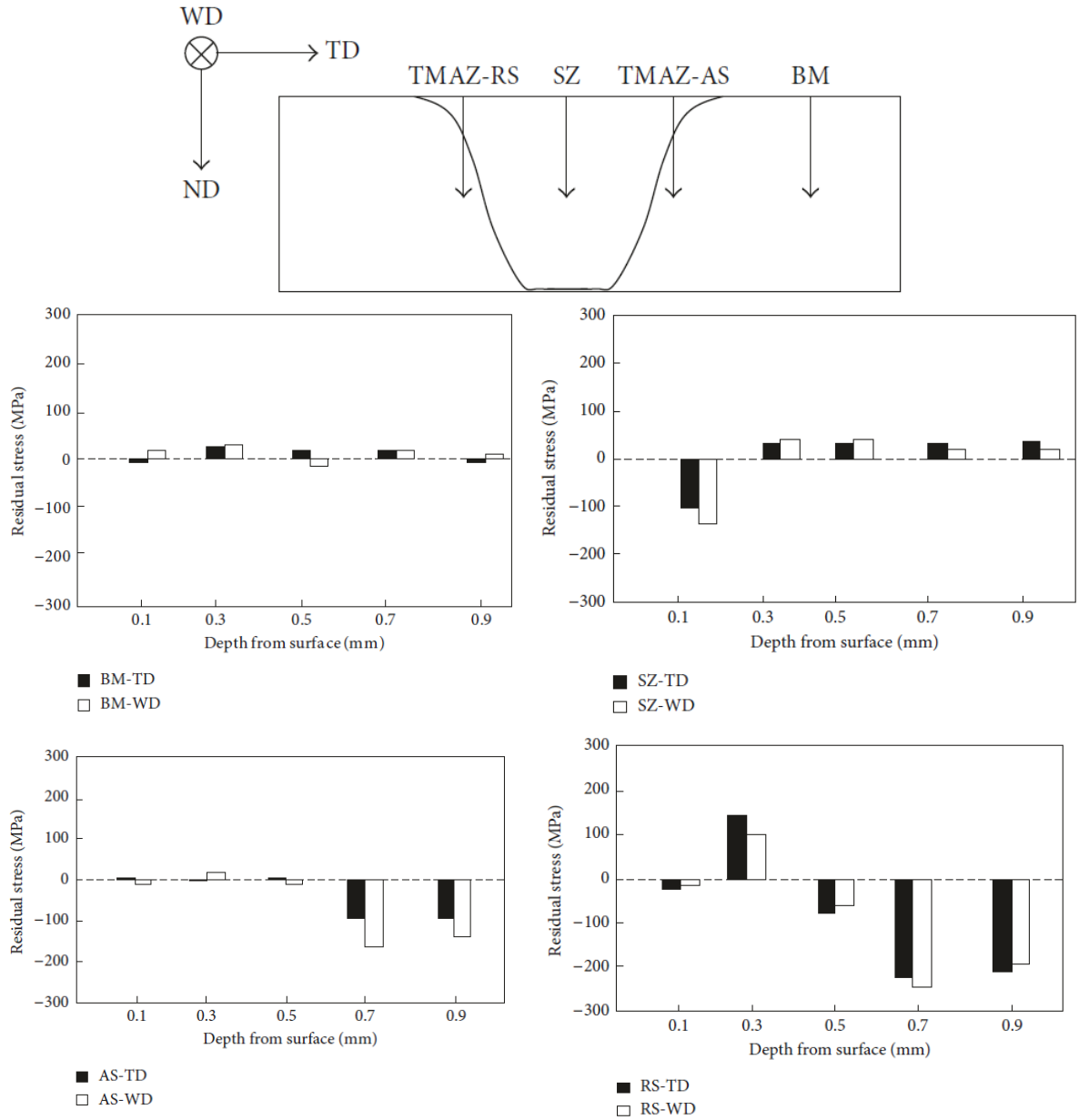

Figure 1.25 Residual stress of LFW joints corresponding to different regions [132]

The welding parameters of applied pressure, oscillation frequency and oscillation amplitude also have significant influence on the residual stress distribution of LFW joints. The

influence of applied pressure on the residual stress of LFWed S45C medium carbon steel measured by X-ray diffraction (XRD) was reported by Gadallah [106], which is illustrated in Table 1.1 and Figure 1.26. The residual stress in the oscillation direction shows a typical residual stress behavior, where the highest tensile stress occurs at the weld center, and the residual stress is drastically decreased to the compressive stress before converging to zero. The residual stress in the pressure direction shows a different distribution compared to that in the oscillation direction. It is observed that the peak residual tensile stress is located at about 4-5 mm from the weld center for all welding conditions. The peak residual tensile stress in the pressure direction is lower than that in the oscillation direction. Overall, the increasing applied pressure results in the decreasing residual stress in the oscillation direction, while the peak residual tensile stress in the pressure direction is increased with increasing applied pressure.

Table 1.1 Welding parameters used the LFW experiment [106]

Welded sample	Frequency (Hz)	Amplitude (mm)	Applied pressure (MPa)	Total length loss (mm)
1	20	1.5	100	3
2	20	1.5	200	3
3	20	1.5	300	3
4	20	1.5	400	3

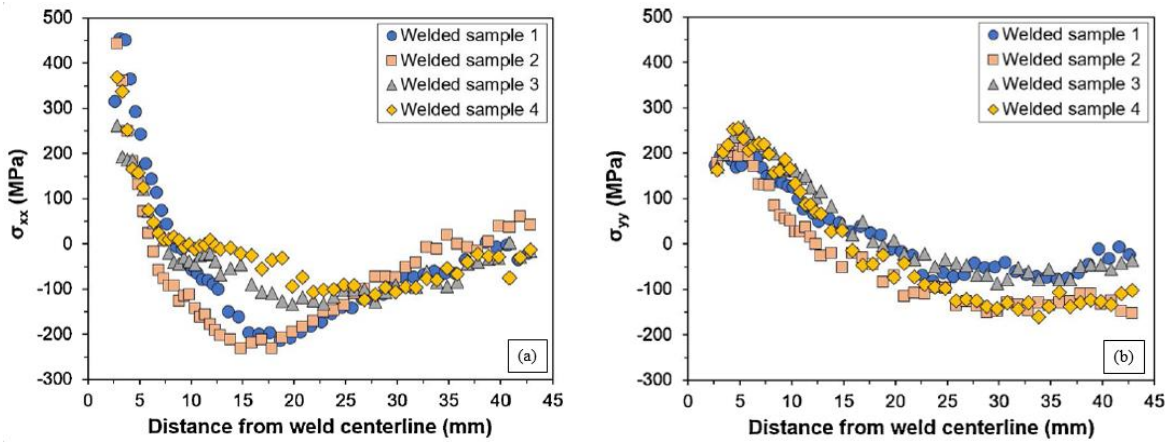

Figure 1.26 Effects of the applied pressure on the residual stress of LFW joints (a) in the oscillation direction; (b) in the pressure direction [106]

1.3.3. Mechanical properties

The FSW and LFW can join steels at a low temperature, which contributes to the favorable toughness, ductility and fatigue strength of welded joints. Nathan [134] compared the mechanical properties of naval grade DMR 249A steel joined by shielded metal arc welding (SMAW), gas metal arc welding (GMA) and FSW. The FSW process was proved to ease the problems due to the fusion welding process including the root flaws, high residual tensile stress and large angular distortion, which contributed to a superior hardness, toughness and tensile strength. Sorger [135] investigated the microstructure and fatigue properties of a FSWed high-strength plate, and it was found that the cracks usually initiated at the interface between the SZ and HAZ where the hardness gradient was steepest. A noticeable change in grain size and grain distribution of the welding tool was also observed. The fatigue behavior of high-yield strength steel welded by FSW and submerged arc welding (SAW) was compared by Beaudet [136], and the FSWed steel was found to have a comparatively higher fatigue strength. However, the defects at the weld root due to the FSW resulted in lower fatigue life and required further improvement of the welding process. Wang [137] studied the corrosion fatigue behavior of FSWed interstitial free steel. The results indicated that the grain refinement induced by FSW enhanced the corrosion fatigue performance by increasing the nucleation and growth resistance of fatigue cracks. The novel *S-N* curve parameters for FSWed mild steel were proposed by Polezhayeva [138], as the experimental results showed a shallower slope compared to that recommended by International Institute of Welding (IIW) for a fusion weld. Although minor surface breaking flaws were observed, the overall fatigue strength of FSW joints was still considerably higher than the design curve FAT80. Lakshminarayanan [139] studied the fatigue strength and crack propagation behavior of ferrite stainless steel joined by FSW. The fatigue strength was increased by 24% and the threshold of crack propagation was by 28% compared to the base metal.

So far, the studies of FSW are mostly conducted on the common steel with favorable weldability even joined by the conventional welding technologies. The application of FSW to the weathering steel with comparatively poor weldability still remains to be investigated and

verified. A study of FSWed weathering steel with high wt.% P was conducted by Kawabubo [97]. As seen Figure 1.27, compared to the BM, the ductile-to-brittle transition temperature (DBTT) of the SZ decreased for steels with both 0.1% P and 0.3%P. In particular, the brittle fracture did not occur for the SZ of the 0.1% P steel obtained below A_1 temperature even at a boiling temperature of liquid nitrogen. In addition, the SZ of the 0.3% P steel joined below A_1 temperature shows favorable toughness with a DBTT as low as -175°C. In spite of outstanding mechanical properties as described in above studies, the yield and fracture mechanism of FSWed weathering steels with high wt.% P are not fully understood. Moreover, the improvement of the mechanical properties can also be expected considering an optimization of the chemical compositions of the alloying elements.

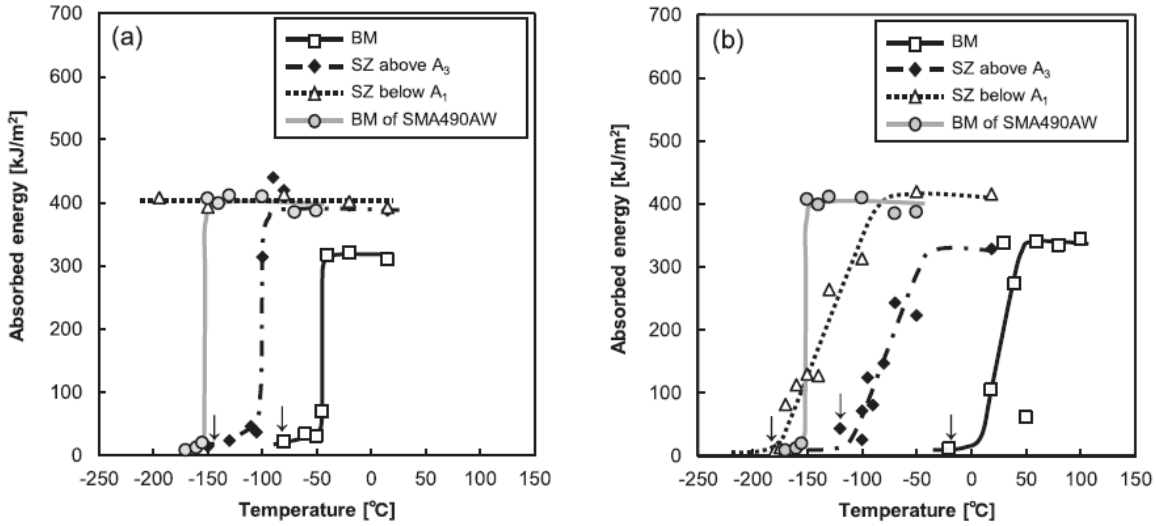

Figure 1.27 Relationship of temperature to absorbed impact energy of SZ above A_3 temperature and below A_1 temperature (a) 0.1% P steel; (b) 0.3% P steel [97]

The mechanical properties of LFWed steels are also widely studied. Aoki [111] joined medium carbon steels at different frequencies and applied pressures. The welded joints were reported to fracture at BM which was far from the weld line as seen Figure 1.28. Su [124] studied the microstructure and mechanical properties of LFW joined high carbon rail steel. A large amount of martensite was formed in the weld center zone (WCZ) where brittle fracture usually occurred, and the tensile strength of the welded joints was 78.5% of the BM. Geng [129] optimized the welding parameters of LFW to join the 1015 mild steel. Well-formed and defect-free joints were obtained, and the tensile strength of the joints could reach up to 90% that of the BM. Kuroiwa [122] performed the LFW process on medium-carbon steels, and

demonstrated that the welding temperature was decreased with the increasing applied pressure. The processing parameters were optimized to achieve a temperature as low as the A_1, and welded joints with high toughness and no brittle martensitic transformation were obtained. Li [128] joined the S31042 heat-resistant steel by LFW and a sound joint free of cracks and pores was obtained. The dynamic recrystallization of the austenitic grains resulted in an improvement of the mechanical properties, and the tensile strength of the joint was comparable to that of the base metal. The parameters of LFW process for the AISI 316L stainless steel were optimized by Bhamji [123]. Variation in the welding parameters was proved to have a significant impact on the microstructure of welds while it had no obvious influence on the tensile strength of welded joints in most cases. In spite of the outstanding mechanical properties as described in the above researches, the studied steels all featured a low wt.% P. For the weathering steels with high wt.% P, it is still unclear whether the inhibition of P segregation and solidification cracks can be achieved by LFW.

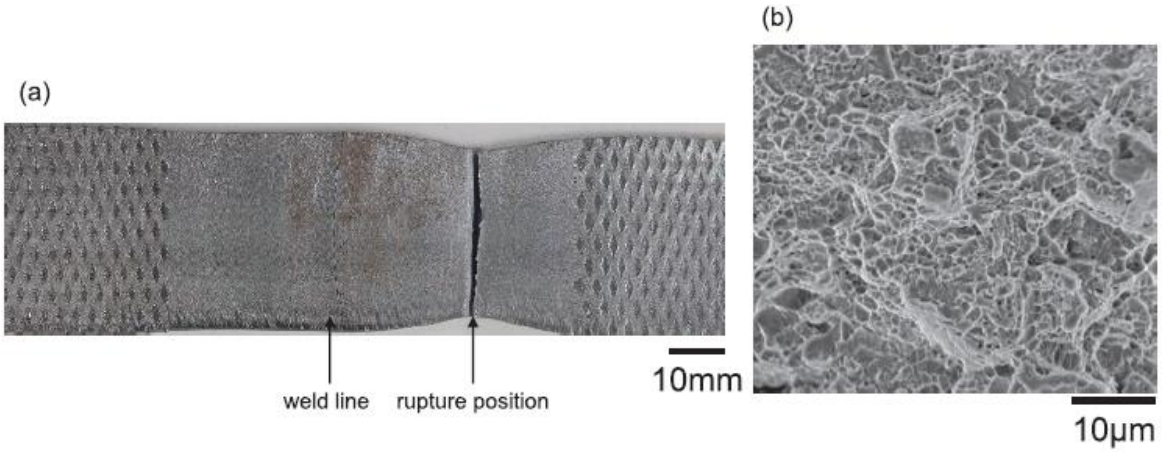

Figure 1.28 Fracture of LFW specimen (a) fracture position; (b) fractography [111]

The fatigue strength of LFW joined steels, which is one of the most significant factors considered in structural design, is barely reported in existing references. Currently, the assessment of the fatigue strength of LFW joints has mostly focused on the titanium alloys and their dissimilar welds. Rajan [140] joined the dissimilar titanium alloys of Ti64 and Ti6243 by LFW and assessed the fatigue strength of the welded joints in both the low and high cycle fatigue regimes. The fatigue failure always occurred at the base metal of the welded joints,

indicating a high fatigue strength of weldment. To improve the fatigue strength of LFW joints of Ti17, a post-weld heat treatment (PWHT) was conducted by García [141]. The weak zones of the weld were remarkably recrystallized into β grains with α after the PWHT, and the fatigue strength of the LFW joints was comparable to that of the base metals. Wen [142] studied the dissimilar joints of TC4 and TC11 titanium alloys by LFW and the welded joints with no soft zone were obtained. The fatigue fracture of LFW specimens occurred at the base metal far from the weld line, and illustrated a high durable and sound dissimilar joint. So far, only one publication [143] was found on the fatigue cracking behaviors of LFW joined steels to the best of authors' knowledge, while it aimed to establish the relationship between fracture location, crack morphology and material condition in the weld. The basic information of fatigue strength of LFW joints assessed by the stress or strain method was not available. The fatigue performance of LFW joined steels, especially for the weathering steels with high wt.% P, is far from a total understanding. Also, the existing studies were conducted on finely polished specimens with no geometry discontinuities, while the welded joints in steel structures often work with local stress concentration and residual stress. The influence of flash formed during the LFW process on the fatigue strength of LFW joints is far from well understood. To fully explore the application of LFW to joining the weathering steels in steel structures, further investigation is required to understand the cracking behaviors and fatigue strength of LFW joints by considering the geometry discontinuities.

1.4. Faced problems and challenges

The previous sections described the advantages of weathering steel to improve the anti-corrosion properties of steel structures, and the promising potentials of FSW and LFW to be applied in engineering. Despite the outstanding merits of weathering steel, the solidification crack due to P segregation can easily occur if joined by conventional fusion welding. However, increasing service time of the steel structures requires a stronger anti-corrosion performance [144]. In other words, a higher wt.% P and other alloying elements are necessary in weathering steel, while no occurrence of the solidification crack should be guaranteed after welding, which

is a great challenge for the conventional fusion welding technologies.

The FSW and LFW which can join materials at low temperature are possibly the effective ways to join weathering steel with high wt.% P. Various kinds of steels have been successfully joined by FSW and LFW, showing favorable mechanical properties. But studies of FSW and LFW are limited to the common steel with favorable weldability even by the conventional fusion welding technologies. There are barely no reports of weathering steel with high wt.% P joined by FSW and LFW. Whether the P segregation and solidification crack can be inhibited during the FSW and LFW process is still unknown. The microstructure and ductile properties of FSWed and LFWed weathering steel should be assessed to serve as a reference for engineering application. Moreover, the steel structures are often prone to fatigue cracks under the cyclic loadings, thus fatigue strength of FSWed and LFWed weathering steel should also be figured out, considering the influence of high wt.% P. The fatigue performance of FSWed common steels has been widely studied, while there is still no information of weathering steels. On the other hand, the assessment of the fatigue strength of LFW joints has mostly focused on the titanium alloys and their dissimilar welds. The fatigue strength of LFWed steels is barely reported in the existing references. The fatigue performance of FSWed and LFWed weathering steels with high wt.% P is far from a total understanding.

1.5. Objectives and structure of this study

Weathering steel is featured by the strong anti-corrosion performance, and friction welding is an effective technology to join steels at low temperature and inhibit solidification cracks. The main purpose of this study is to investigate the possibility of joining weathering steel with high wt.% P by FSW and LFW at low temperature, so that solidification cracks which prevent the further application of weathering steel to the steel structures can be inhibited. Based on the successful joining of the conventional weathering steels, the new weathering steels with higher wt.% P, i.e., stronger anti-corrosion performance, are also developed and joined by FSW. The microstructures, geometry characteristics, residual stress and mechanical properties of FSWed and LFWed weathering steels are also studied to serve as a reference in structural design.

The structure of this dissertation is shown in Figure 1.29.

In Chapter 1, the risks of corrosion to steel structures were introduced, and the advantages and difficulties of weathering steels applied to steel structures were elaborated. A brief overview of friction welding, including development history, conceptualization, characteristics, potential industrial applications, and advantages of joining weathering steels, was conducted.

In Chapter 2, the optimization of welding parameters and process of FSW and LFW were introduced. The anti-corrosion properties of conventional and high-phosphorus weathering steels were compared and assessed by the corrosion resistance index. The experimental procedure of this research, including the measurement of residual stress, geometry and microhardness, observation of metallography, monotonic testing and fatigue experiment, was described. The precisions of measurement methods, such as XRD and digital image correlation (DIC), were also explained.

In Chapter 3, conventional weathering steels SMA490AW and SPA-H were joined by FSW below the A_1 temperature. The geometry characteristics and residual stress were measured and compared. The microstructure of different regions of welded joints was observed, and the corresponding microhardness distribution was analyzed. The yield and fracture characteristics of FSW joints under the monotonic loading were observed by DIC, and their mechanisms were speculated and explained by finite element method (FEM). The fatigue strength of FSW specimens was compared to that of BM specimens and design curves. The ratcheting behaviors and strain accumulation in different welded regions were also measured by DIC and analyzed.

In Chapter 4, new weathering steels with higher wt.% P, i.e., stronger anti-corrosion performance, were developed and joined by FSW below the A_1 temperature. The geometry characteristics and residual stress of FSWed new weathering steels were compared. Influence of wt.% P and other alloying elements on microstructure characteristics was discussed, corresponding to the variation of microhardness, ductile strength and fatigue strength of conventional and high-phosphorus weathering steels. To investigate the influence of solidification cracks on the ductile and fatigue strength of FSW joints, the monotonic and fatigue tests were also conducted on the FSW joints with defects which were caused by the inadequate welding parameters.

In Chapter 5, conventional weathering steels SMA490AW and SPA-H were joined by LFW above the A_3 temperature. The residual stress was measured and compared to conventional steels joined by LFW, thus a general residual stress distribution of LFW joints was summarized. The stress concentration corresponding to various flash shapes was assessed by FEM. The microstructure of LFW joints was observed and its influence on the microhardness was discussed. The monotonic test was conducted on the finely polished and as-welded LFW specimens, and the yield and fracture characteristics were monitored and compared by DIC. The fatigue test was also conducted on the finely polished and as-welded LFW specimens, and the influence of flash shape on the cracking characteristics and fatigue strength was discussed.

In Chapter 6, the conclusions of this dissertation were presented and future works were proposed.

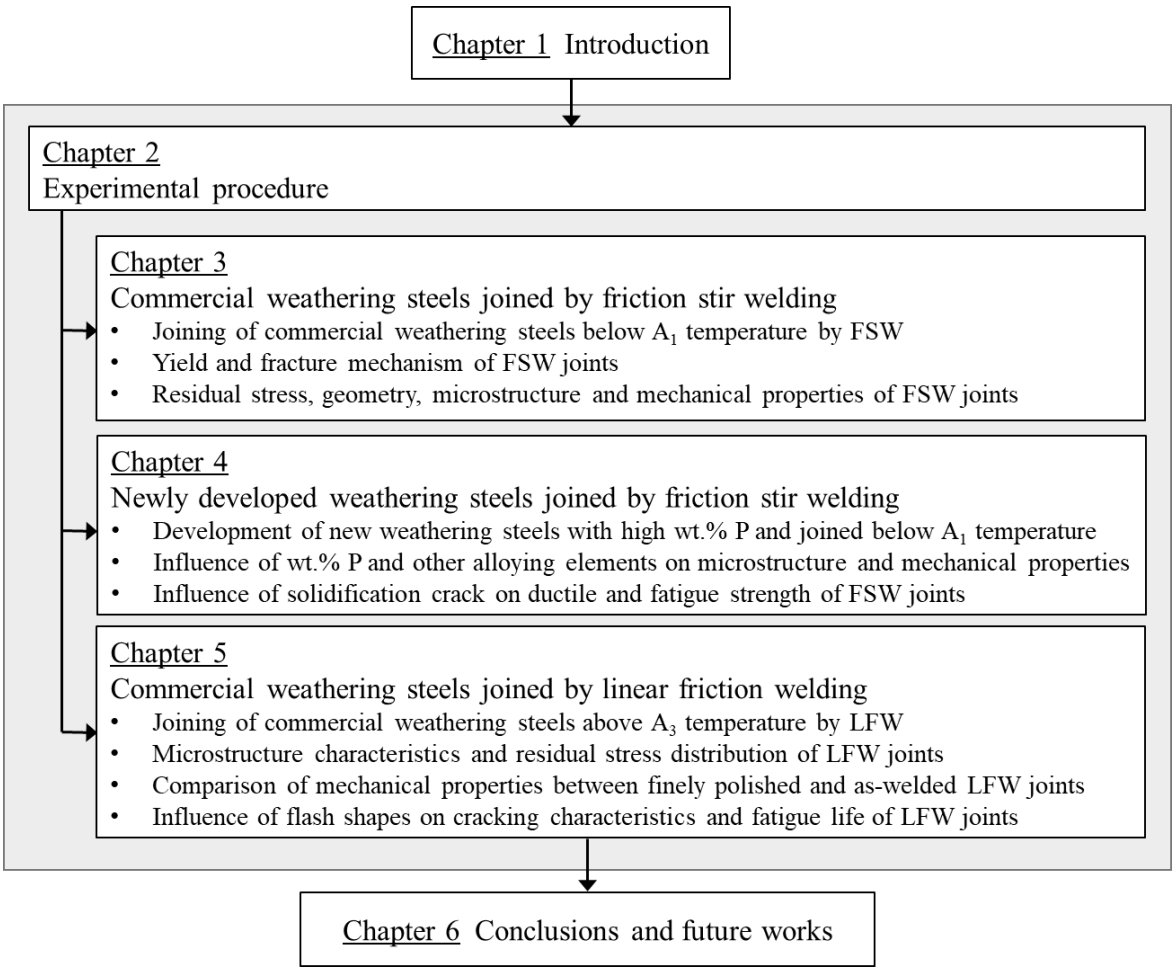

Figure 1.29 Structure of this dissertation

Chapter 2.

Experimental procedure

2.1. Introduction

The welded joints in the real engineering require not only the favorable ductility and toughness, but also the high tensile and fatigue strength. The previous studies by the research team have confirmed the favorable toughness of the weldable weathering steel SMA490AW joined by FSW below A_1 temperature [97]. Therefore, the efforts were also devoted to the non-weldable weathering steel SPA-H to achieve a welding temperature below A_1 in this research. After the successful joining of conventional weathering steels, new weathering steels with higher wt.% P were also developed to give full play to the potentials of FSW. Due to the difficulties in joining weathering steels by LFW below A_1 temperature, the conventional weathering steels were joined by LFW above A_3 temperature in this research. The welding parameters were optimized based on previous studies [103,111,122,145] to ensure no welding defects.

To investigate the welding quality of FSW and LFW to join weathering steels with high wt.% P, a comprehensive study of microstructure, geometry, residual stress, ductile behavior and fatigue performance of FSWed and LFWed joints was conducted. The detailed experimental procedure including the welding parameters, testing methods and measurement methods was described. The theories and precisions of measurement methods such XRD and DIC were also elaborated for better understanding.

2.2. Materials and welding conditions

2.2.1. Friction stir welding (FSW)

The target welding temperature of FSW is below the A_1 point of the weathering steels in this research. The welding temperature and quality of FSW are mainly decided by the downward load, welding speed and rotation speed. A large downward load results in a higher welding temperature, making it difficult to control the temperature below A_1. However, the welding tool cannot be fully plunged into the BM if a low downward load is applied. The friction heats generated between the tool shoulder and the BM are not sufficient, resulting in the possible fracture of the welding tool. The microhardness of BM has a large influence on the decision of an proper downward load, thus the downward load of this research (42kN for SMA490AW, SPA-H, Steel1 and Steel2; 52kN for Steel3) was initially determined according to the welding of metals with similar microhardness in previous research [61,145]. Then the downward load was properly optimized (45kN for SMA490AW, SPA-H, Steel1 and Steel2; 55kN for Steel3) to achieve the FSW joints without welding defects.

The lower welding speed and higher rotation speed often contribute to the higher welding temperature. The attempts in this research were made on the welding speed at a range of 100-150 mm/min and rotation speed at a range of 80-400 rpm, resulting in the welding temperature below A_1. The optimization of welding parameters of FSW is shown in Table 2.1. The welding speed and rotation speed were finally decided to be 150 mm/min and 80 rpm for all weathering steels in this research.

Table 2.1 Optimization of welding parameters of FSW

Welding parameters	Welding speed	Rotation speed	Downward load
Ranges	100-150 mm/min	80-400 rpm	42(52) kN→ 45(55) kN

The conventional weathering steels SMA490AW and SPA-H were first joined by FSW. The weldable weathering steel SMA490AW has a wt.% P of about 0.01%, and the non-

weldable weathering steel SPA-H has a wt.% P of about 0.1%. The chemical compositions of SMA490AW and SPA-H are shown in Table 2.2. The FSW was conducted on the steel plates with a dimension of 320mm×150mm×3mm. The butt weld was performed by the FSW machine below the A_1 temperature. The low welding temperature inhibited the P segregation so as to avoid the occurrence of solidification cracks. Besides, the formation of HAZ softening, which was usually induced by high heat input, could also be prevented. The welding tool rotated clockwise and travelled in the rolling direction at a constant welding speed of 150 mm/min and rotation speed of 80 rpm. The welding tool was made of tungsten-carbide, with a concave shoulder diameter of 15mm and a flat pin diameter of 6 mm. The length of the pin was 2.9 mm. The plates were fixed by a backing plate to reduce possible bending deformation. FSW was conducted with a tilt angle of 3° and shielded by Ar gas with a flow rate of 20 L/min to protect the joints and welding tool from oxidation. The initial downward load was controlled at 45 kN during the welding process. The joining process and parameters of FSW are shown in Figure 2.1.

The appearances of FSW joints of SMA490AW and SPA-H are shown in Figure 2.2(a) and (b). The welded plates were visually inspected and exhibited smooth top surfaces with continuously spaced striates. It is observed that the steel plates are perfectly welded without any welding defects such as macroscopic inclusions, undercuts and pores on the surface. Small pieces of specimens were cut from both AS and RS, and observed to ensure there were no interior cracks.

Table 2.2 Chemical composition of weathering steels for FSW (wt.%) and the corrosion resistance index *I*

Material	C	Si	Mn	P	S	Cu	Ni	Cr	Nb	N	O	Al	*I*
SMA490AW	0.12	0.20	1.14	0.012	0.002	0.32	0.10	0.48	0.02				6.13
SPA-H	0.08	0.43	0.38	0.094	0.003	0.31	0.18	0.67					8.06
Steel1	0.098	0.012	0.20	0.10	0.005	0.50				0.003	0.0021	0.011	6.40
Steel2	0.095	0.012	0.20	0.28	0.005	0.51				0.003	0.0021	0.010	9.44
Steel3	0.103	0.37	0.41	0.32	0.003	0.30	0.20	0.70	0.021	0.003	0.0014	0.012	11.48

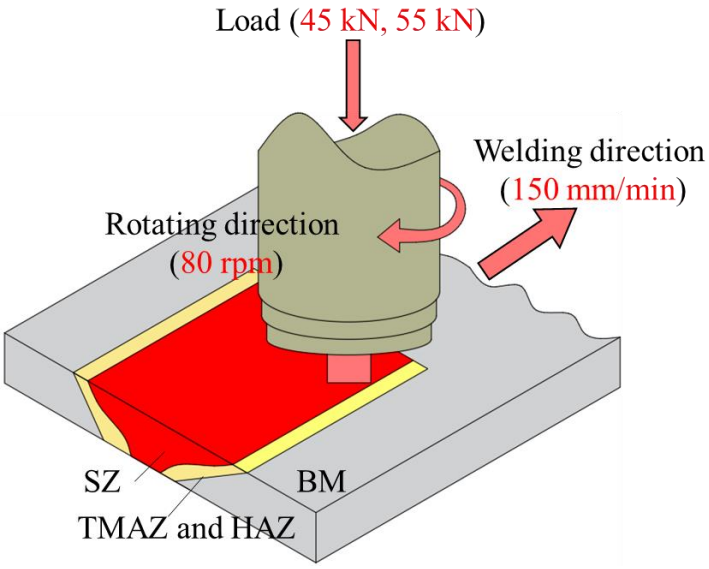

Figure 2.1 Joining process and parameters of FSW

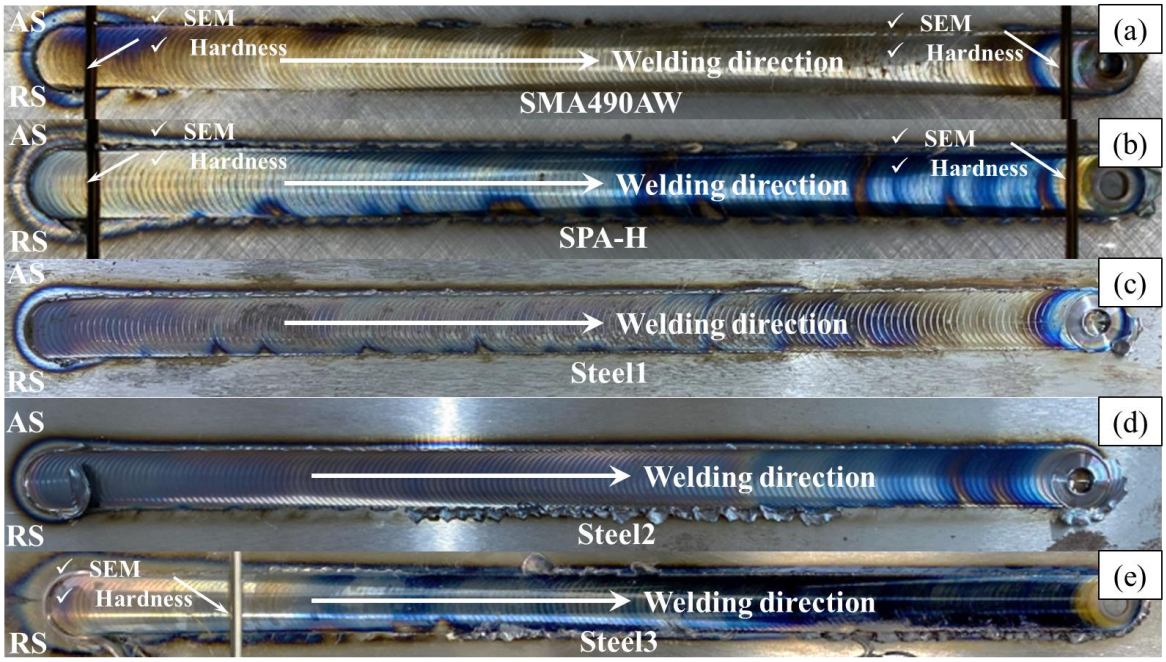

Figure 2.2 Appearance of FSW joints of different steels (a) SMA490AW; (b) SPA-H; (c) Steel1; (d) Steel2; (e) Steel3

After the successful joining of conventional weathering steels SMA490AW and SPA-H, three kinds of weathering steels with high wt.% P were newly developed and also joined by FSW. The chemical compositions of the new weathering steels are shown in Table 2.2. The influence of wt.% P on the microstructure and mechanical properties of FSW joints was studied by comparison of Steel1 and Steel2. The alloying elements (Ni, Cr and Nb) were added to Steel3 to achieve refinement of the microstructure and increase the toughness. The anti-

corrosion performance can be assessed by the corrosion resistance index *I* as calculated by Equation (2.1) and the higher index *I* indicates better corrosion resistance. The sequence of anti-corrosion performance of five steels assessed by the corrosion resistance index *I* is: Steel3 > Steel2 > SPA-H > Steel1 > SMA490AW. The base metal of new weathering steels was melted in a vacuum induction furnace. The ingot of Steel1 and Steel2 was hot-rolled at the expected temperature of 1000℃ followed by heat treatment at 1000℃ for 15 minutes. The ingot of Steel3 was hot-rolled at the expected temperature of 1200℃ without heat treatment, because the addition of Nb was expected to achieve refinement of the microstructure. All ingots of new weathering steels were cut into steel plates with a dimension of 320 mm × 150 mm × 3mm, the same as that of the conventional weathering steels SMA490AW and SPA-H.

$$I = 26.01(\%Cu) + 3.88(\%Ni) + 1.20(\%Cr) + 1.49(\%Si) + 17.28(\%P) - 7.29(\%Cu)(\%Ni) - 9.10(\%Ni)(\%P) - 33.39(\%Cu)^2 \quad (2.1)$$

2.2.2. Linear friction welding (LFW)

The target welding temperature of LFW is above the A_3 point of the weathering steels in this research. The welding temperature and quality of LFW are mainly decided by the frequency, applied pressure and amplitude. The displacement amplitude was controlled at 1.5 mm in this research based on previous references [111][122]. The higher frequency often results in faster increasing of the welding temperature. The attempts were made on the frequency at a range of 15-50 Hz in this research. The strength of materials at the weld interface is degraded with friction heat input, and the materials are extruded as flash when the shear strength is lower than the applied shear force. Therefore, the higher applied pressure can extrude the flash even when the materials are still strong and the temperature is low. However, the solidification cracks can easily occur for the weathering steels if joined at the low temperature. The applied pressure varied from 50 MPa and 250 MPa during the optimization process. The optimization of welding parameters of LFW is shown in Table 2.3. The frequency and applied pressure were finally decided to be 50 Hz and 50 MPa for weathering steels with different plate thickness in this

research.

Table 2.3 Optimization of welding parameters of LFW

Welding parameters	Frequency	Applied pressure	Displacement amplitude
Ranges	15-50 Hz	50-250 MPa	1.5 mm

The weldable and unweldable weathering steels SMA490AW and SPA-H were joined by LFW above the A_3 temperature. Although the same grade of conventional weathering steels as in Section 2.2.1 was used, the chemical compositions of two weathering steels for LFW were slightly different as shown in Table 2.4, because the steels were bought from different retailers. Two workpieces of SMA490AW and SPA-H with the dimensions of 63 mm × 30 mm × 12 mm were butt joined by LFW. To investigate the mechanical performance of as-welded LFW joints, the workpieces of SPA-H with smaller thickness (63 mm × 30 mm × 3 mm) were also joined. The same welding condition (frequency f_1 = 50 Hz, displacement amplitude U = 1.5 mm and applied pressure P = 50 MPa) was used for two weathering steels based on previous studies, resulting in a welding temperature above A_3. The joining process and parameters of FSW are shown in Figure 2.3. The oscillation direction was defined as X-axis, the direction of the applied force was defined as Y-axis and the direction of the plate thickness was defined as Z-axis.

Table 2.4 Chemical composition of conventional weathering steels for LFW (wt.%)

Material	C	Si	Mn	P	S	Cu	Ni	Cr	Nb	V
SMA490AW	0.12	0.20	1.14	0.010	0.003	0.31	0.09	0.46	0.02	0.04
SPA-H	0.08	0.44	0.39	0.087	0.003	0.27	0.17	0.64		

2.3. Testing method

2.3.1. Measurement of weld geometry and welding residual stress

The global geometry of FSW and LFW joints was measured to assess the angular

distortion α and eccentric misalignment δ, using VL-500 geometry scanning machine with a precision of 10 μm as seen Figure 2.4(a). The definition of the angular distortion α and eccentric misalignment δ is shown in Figure 2.4(b). The weld profile of LFW joints was measured using a VR-5000 geometry scanning machine with a precision of 1.0 μm as seen Figure 2.4(b), based on which the weld toe radius ρ and stress concentration factor (K_t) could be assessed.

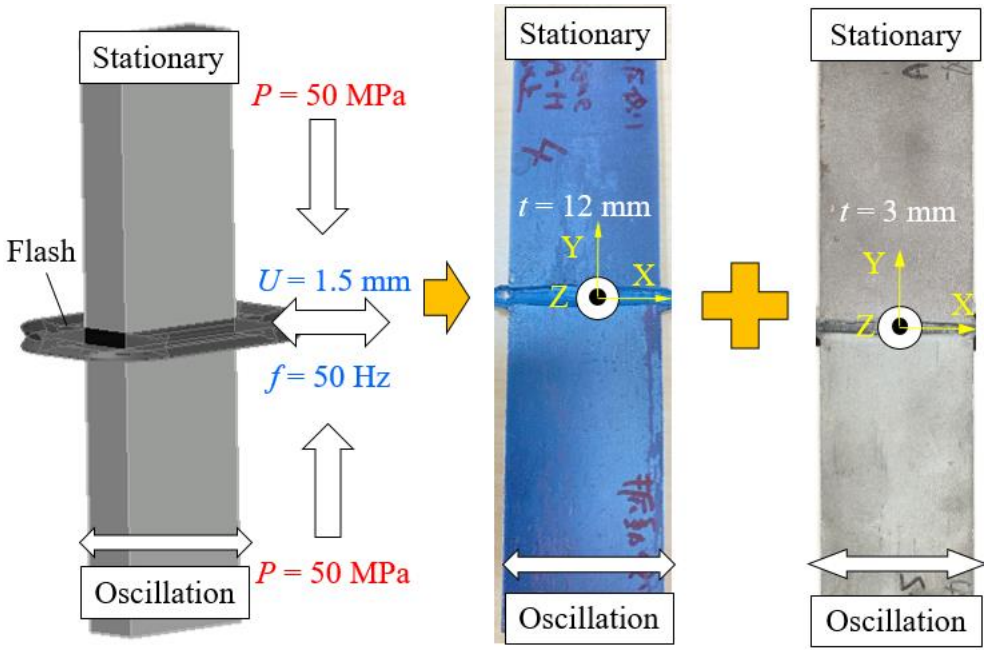

Figure 2.3 Joining process of FSW

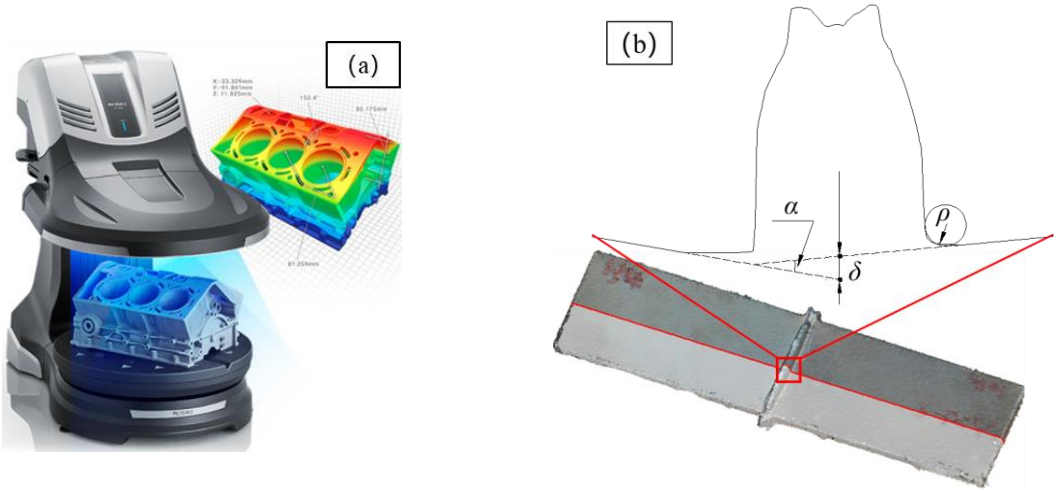

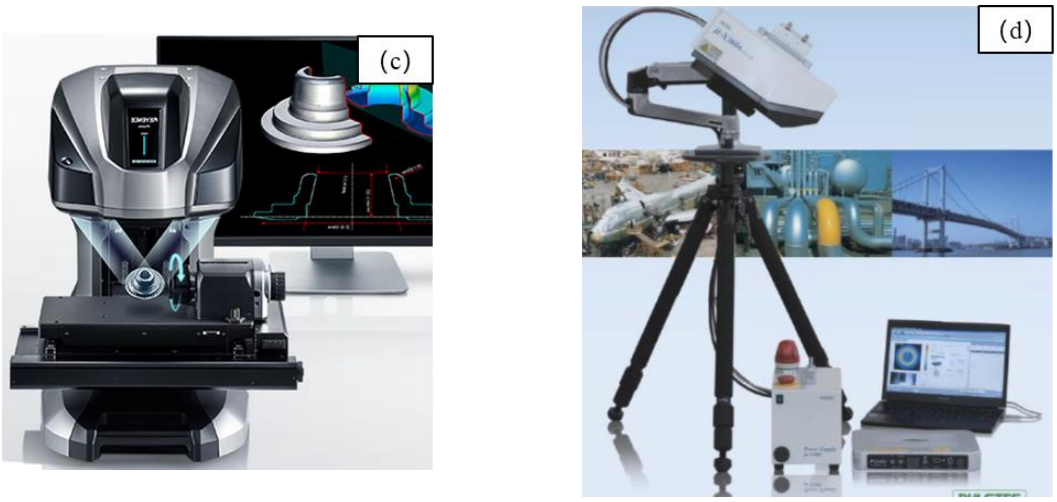

Figure 2.4 Instruments for measurement of weld geometry and welding residual stress (a) VL-500; (b) definition of the angular distortion and eccentric misalignment; (c) VR-5000; (d) XRD

The residual stress of FSW joints and LFW joints was measured by XRD as seen Figure 2.4(c). The measurement was conducted at an interval of 0.5 mm near the weldment and 1.0 mm far from the weldment within the error of ±40 MPa. For FSW joints, the residual stress perpendicular to the welding direction ($\sigma_{R\text{-}Y}$) was measured along the centerline for each weathering steel. For LFW joints, the residual stress in the oscillation direction ($\sigma_{R\text{-}X}$) and perpendicular to the oscillation direction ($\sigma_{R\text{-}Y}$) was measured along the centerline for both weathering steels.

2.3.2. Metallographic, ductile and fatigue tests

To investigate the microstructure characteristics of FSW joints, the metallographic samples for each weathering steel were fabricated as shown in Figure 2.5. The WD, TD and ND constitute the principal coordinates of FSW. The metallographic samples were sliced perpendicular to the WD by electrical discharge machining (EDM). Before the microstructure analysis, the metallographic samples were ground with sandpaper (SiC) of up to 2000 grit, and the acidic alumina up to 1 μm R_a was used for final polishing. In order to display the microstructure of the transverse cross section, the samples were etched using 2% nital solution, and observed by scanning electron microscope (SEM) and EBSD.

Taking the center of the section of the metallographic samples as the ordinate origin, the microhardness was measured at three different depths from the FSW-processed surface (i.e., the top side, the section center and the bottom side) in the normal-transverse (ND-TD) plane. The measurement was conducted at every 0.3 mm interval under the force of 0.1N.

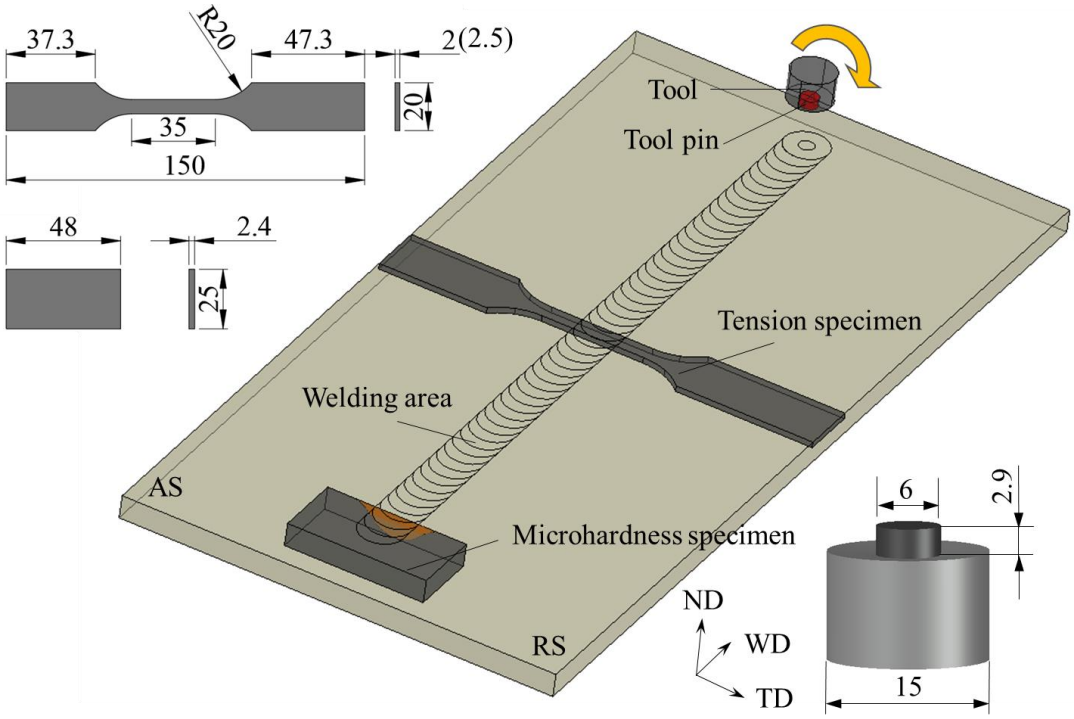

Figure 2.5 Fabrication of metallographic samples, tension and fatigue specimens for FSW joints

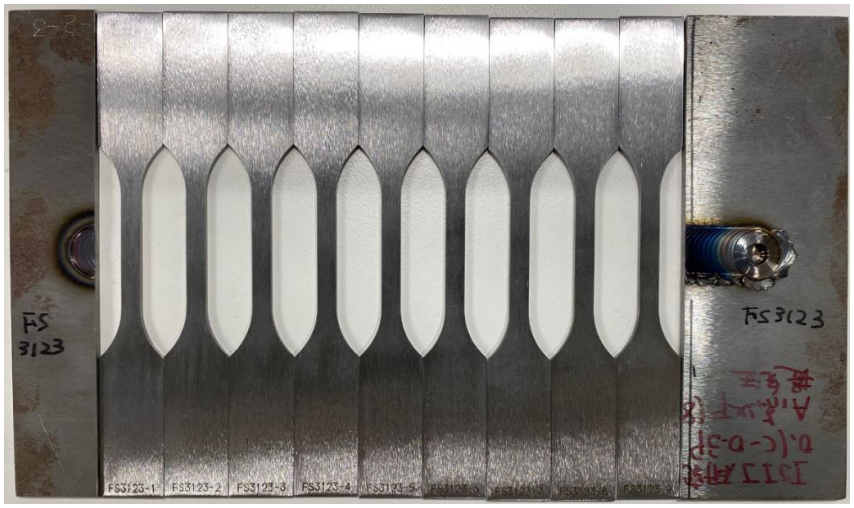

Figure 2.6 Appearance of tension and fatigue specimens (unit: mm)

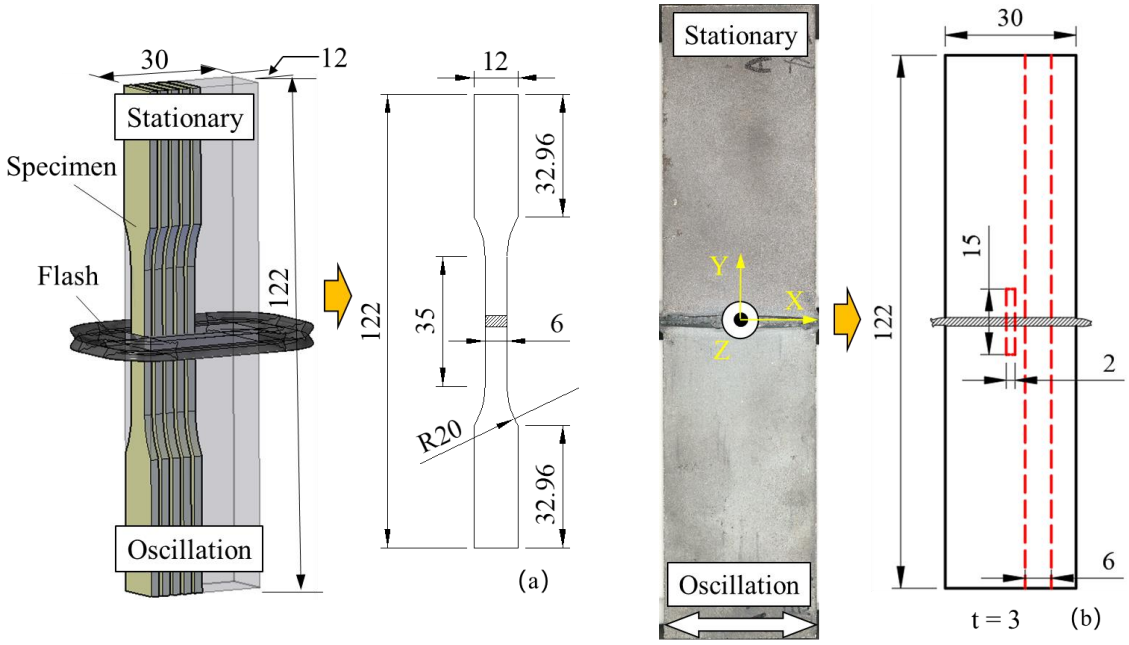

Figure 2.7 Fabrication of metallographic samples, tension and fatigue specimens for LFW joints. (a) SMA490AW and SPA-H with thickness of 12 mm (b) SPA-H with thickness of 3 mm (unit: mm)

The specimens for tension and fatigue tests were machined perpendicular to WD from the welded plates. The welded plates were first sliced from the top and bottom surface to reduce the influence of welding angular distortion, and the FSW processing side of fatigue specimens was ground to remove the surface ripples and notches. Because the fatigue strength is very sensitive to the surface roughness, the FSW specimens were then polished by the sandpapers up to 1000 grits. The specimens of the base metal were also made for comparison. The plate thickness was decided as 2 mm for FSW specimens and 2.5 mm for BM specimens. The geometry size was decided following JIS [146] as shown in Figure 2.5, and appearance of tension and fatigue specimens is shown in Figure 2.6.

For LFW joints, the metallographic samples for SMA490AW and SPA-H were cut from the center of the welded joints in the thickness direction with a size of 15 mm × 12 mm × 2 mm. The metallographic samples were ground by sandpaper (SiC) of up to 2000 grits, and acidic alumina up to 1 μm R_a was used for final polishing. The measurement of the microhardness was conducted on half of the polished surface at every 0.3 mm interval under the force of 0.1 N. The other half of the surface was etched using 2% nital solution for the

microstructure analysis and observed using SEM.

The ductile and fatigue performance of finely polished LFW specimens and as-welded LFW specimens were studied respectively. The finely polished LFW specimens for SMA490AW and SPA-H were fabricated from the LFW joints with thickness of 12 mm, as seen in Figure 2.7(a). The as-welded specimens were sliced from LFW joints with a geometry of 122 mm × 6 mm × 3.2 mm as shown in Figure 2.7(b). The cut section was finely polished by sandpaper (SiC) of up to 1000 grits, while the flash on the surface (X-Y plane) was kept to investigate the influence of geometry discontinuities on the fatigue strength.

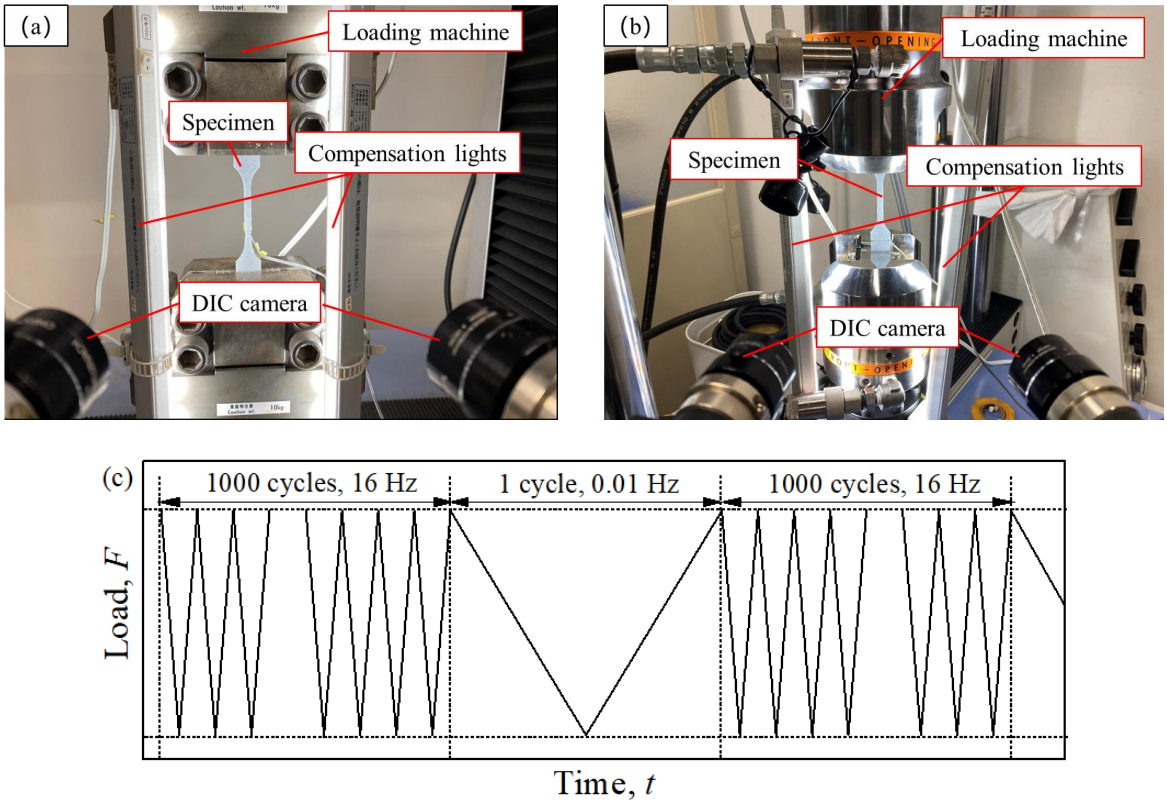

Figure 2.8 Setup of experiment (a) monotonic experiment; (b) fatigue experiment; (c) fatigue loading spectrum

The monotonic experiment setup is shown in Figure 2.8(a). The monotonic loading was conducted by a Shimadzu 50 kN testing machine under the loading rate of 0.1 mm/min. The fatigue experiment was carried out by a servo 4830 hydraulic testing machine, as seen in Figure 2.8(b). The stress ratio R was equal to 0.1 and the loading frequency f_2 was constant at 16 Hz.

The DIC method was used to measure the strain distribution during the monotonic and fatigue experiment. In order to obtain sufficient data of strain distribution on the surface of the specimen during the fatigue loading, the loading frequency f_2 was decreased to 0.01 Hz every 1000 cycles. The loading spectrum is shown in Figure 2.8(c)

2.3.3. Measurement of strain by digital image correlation (DIC)

For the global strain measurement of FSW specimens and LFW specimens during the monotonic loading, the DIC system used in this study for strain monitoring includes a pair of CCD cameras with a fixed 50mm lens mounted on the 3-axis stage and two LED lights to compensate for illumination in the room. The exposure and aperture settings were adjusted to achieve a favorable focus when the confidence interval *Pr* was as close to zero as possible. All images were taken by 2736 × 2192 pixels, resulting in a spatial resolution of about 7.1×10^{-3} mm^2/pixel within the area of interest (AOI) of approximately 915mm^2. The AOI in this research refers to the surface of the specimen where the strain distribution is measured. The local crack propagation during the fatigue loading was measured by cameras with a much smaller AOI of approximately 56 mm^2, resulting in higher spatial resolution of about 1.1×10^{-5} mm^2/pixel [147].

The VIC-3D (Correlated Solutions) software with the measurement resolution ranging from 1/50 to 1/100 pixels was used for the strain analysis. Each image was compared to the initial reference image captured under zero load. The subset size, which controlled the area of the image used to track the displacement between the images, was set to 29 × 29 pixels as suggested by the software. The step size (the distance between two consecutive displacement vectors) was set to 1/4 of the subset size, in order to achieve independent and non-repetitive data. A high-order interpolation scheme of optimized 8-tap spline was used to achieve sub-pixel accuracy and ensure analysis efficiency. The correlation criterion was set to the normalized squared differences, which usually offered the best combination of flexibility and results. The confidence interval *Pr* at the correlated points was calculated in pixel for each match. The illumination, camera mount, surface treatment, subset size and step size were set, so that the confidence interval was generally lower than 0.01 pixel (i.e., 1% of a pixel) in all analyses reported here, except for the lower part of the specimen, which was slightly greater.

One example of the confidence interval is shown in Figure 2.9(a) [148]. The reason for the higher confidence interval on the lower part is that the cameras were set to look up to the specimen, while some of the lights scattered from the lower part of the specimen to the cameras were impeded by the lower chuck. Nonetheless, the confidence interval of the lower part was only about 0.2% higher, as seen in Figure 2.9(a), indicating a favorable precision.

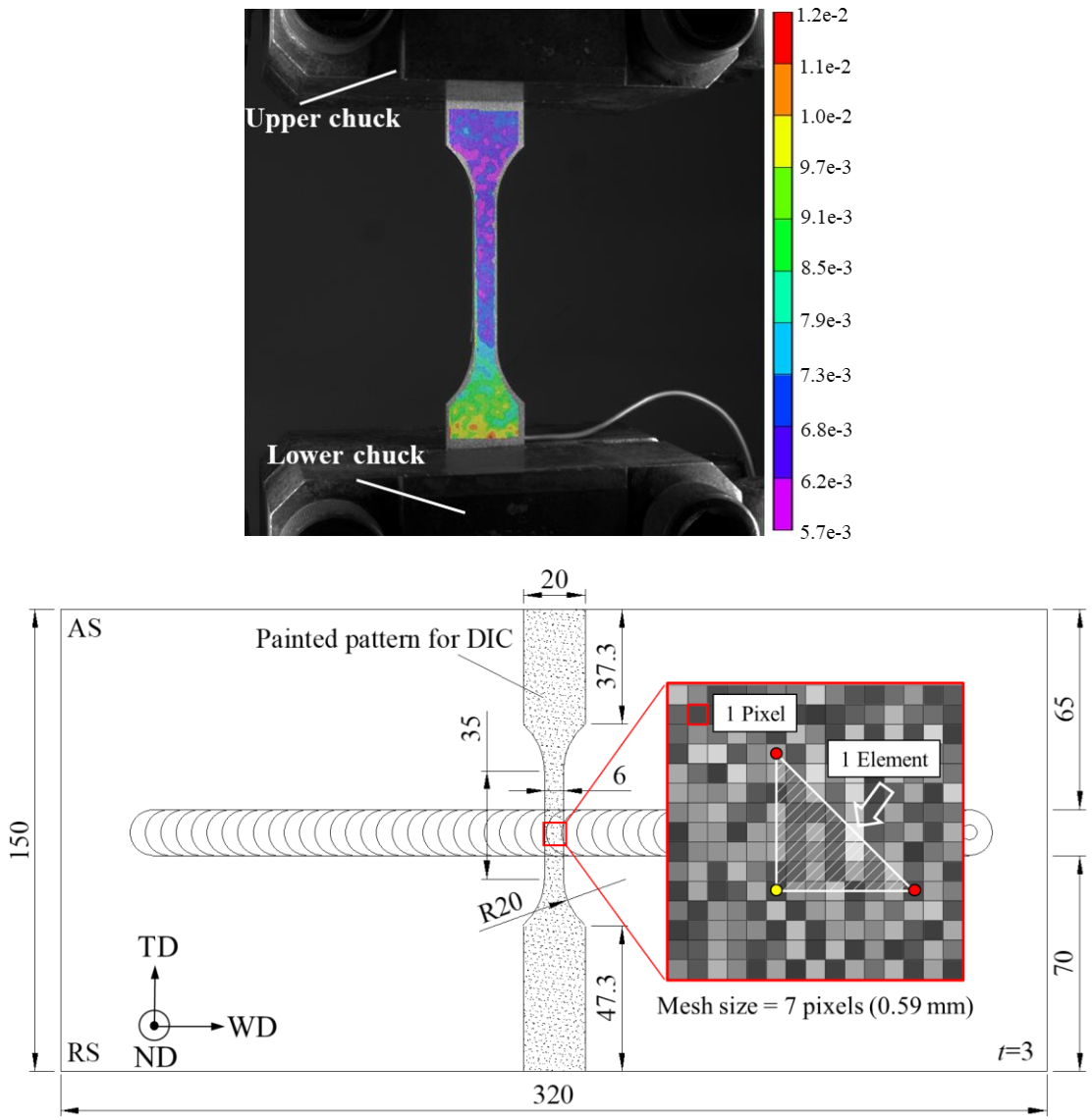

Figure 2.9 Strain measurement by DIC (a) confidence interval, *Pr* (pixel); (b) calculation method of DIC

For the finely polished specimens, the nominal strain in this research was defined by the total elongation of the parallel part of the specimen (35 mm). To investigate the plastic

deformation of different zones (BM, SZ and HAZ), the axial strain was also defined based on the correlation methods of DIC, as illustrated in Figure 2.9(b) [149]. The specimen surface is actually divided by a large number of pixels, which are illustrated by the grids with different gray levels. The identical grid before and after deformation can be recognized based on the gray value so as to calculate the displacement based on the spatial relationship calibrated during the setup of the experiment. If strain of the pixel marked by yellow is to be calculated, this pixel together with the surrounding pixels can constitute a triangle mesh by which the strain can be obtained. The strain within the pixels can be interpolated by the polynomial function. The gap between the studied pixel (marked by yellow) and surrounding pixels (marked by red) which covers several pixels is the triangle length, and should be determined considering the computational efficiency and precision. Similar to finite element analysis, the smaller step size can result in better precision, but much longer computation time. In this study, the step size of 7 pixels was used for the strain calculation; thus, the global axial strain was calculated by a mesh size of 0.59 mm, and the local axial strain for crack propagation measurement was 0.023 mm.

2.4. Conclusions

In this chapter, the optimization of welding parameters of FSW and LFW was elaborated. The welding process of FSW and LFW on the conventional weathering steels SMA490AW and SPA-H was described in details. After the successful joining of conventional weathering steels, the new weathering steels with higher wt.% P were developed and also joined by FSW. The theories and precisions of measurement method were also explained. The specific conclusions are as follows:

(1) To achieve the FSW joints without welding defects below the A_1 temperature, the welding speed and rotation speed were optimized to be 150 mm/min and 80 rpm for all weathering steels in this research. The downward load was 45 kN for SMA490AW, SPA-H, Steel1 and Steel2, and 55 kN for Steel3 with higher microhardness.

(2) To achieve the LFW joints without welding defects above the A_3 temperature, the

frequency and applied pressure were optimized to be 50 Hz and 50 MPa for weathering steels with different plate thickness in this research. The displacement magnitude was controlled at 1.5 mm.

(3) The conventional weathering steels SMA490AW and SPA-H were successfully joined by FSW below A_1 temperature and LFW above A_3 temperature. The new weathering steels with higher wt.% P were developed to achieve stronger anti-corrosion performance, and also joined by FSW below A_1 temperature. The sequence of anti-corrosion performance of five steels assessed by the corrosion resistance index *I* is: Steel3 > Steel2 > SPA-H > Steel1 > SMA490AW.

(4) The general geometry of welded joints was measured with a precision of 10 μm, and the weld profile with a much smaller scale was measured with a precision of 1.0 μm. The residual stress was measured within the error of ±40 MPa.

(5) The global strain was measured by DIC by a spatial resolution of about 7.1×10^{-3} mm^2/pixel within the AOI of approximately 915mm^2. The local crack propagation during the fatigue loading was measured by cameras with a much smaller AOI of approximately 56 mm^2, resulting in a higher spatial resolution of about 1.1×10^{-5} mm^2/pixel.

Chapter 3.

Conventional weathering steels joined by friction stir welding

3.1. Introduction

The conventional weathering steels SMA490AW and SPA-H were successfully joined by FSW below A_1 temperature. The testing and measurement method were elaborated in details (see Chapter 2). In this chapter, influence of the microstructure characteristics on the microhardness, ductile properties and fatigue behaviors was discussed. The geometry and residual stress of FSWed weldable and non-weldable weathering steels were compared. The yield and fracture processes of FSW joints under the monotonic loading were monitored by DIC, the mechanism of which was speculated and verified by FEM. The fatigue behaviors including the fatigue strength, ratcheting behaviors and strain accumulation in different regions of FSW joints were also investigated with the aid of DIC. The fractography under the monotonic loading and fatigue loading was also compared and analyzed, which helped to explain the ductile and fatigue fracture characteristics of FSW joints.

3.2. Residual stress, microstructure and microhardness

3.2.1. Geometry and residual stress

The global geometry of FSW joints was scanned by VL-500, and the weld shape

perpendicular to the welding direction in the centerline is shown in Figure 3.1. Both the weld shape of the welding surface and opposite the welding surface was measured. It is observed that the weld shape shows a concave shape on the welding surface due to the downward load during the welding process. The weld shape opposite the welding surface is convex because of the angular distortion. The angular distortion of SMA490AW with smaller wt.% P is smaller than that of SPA-H.

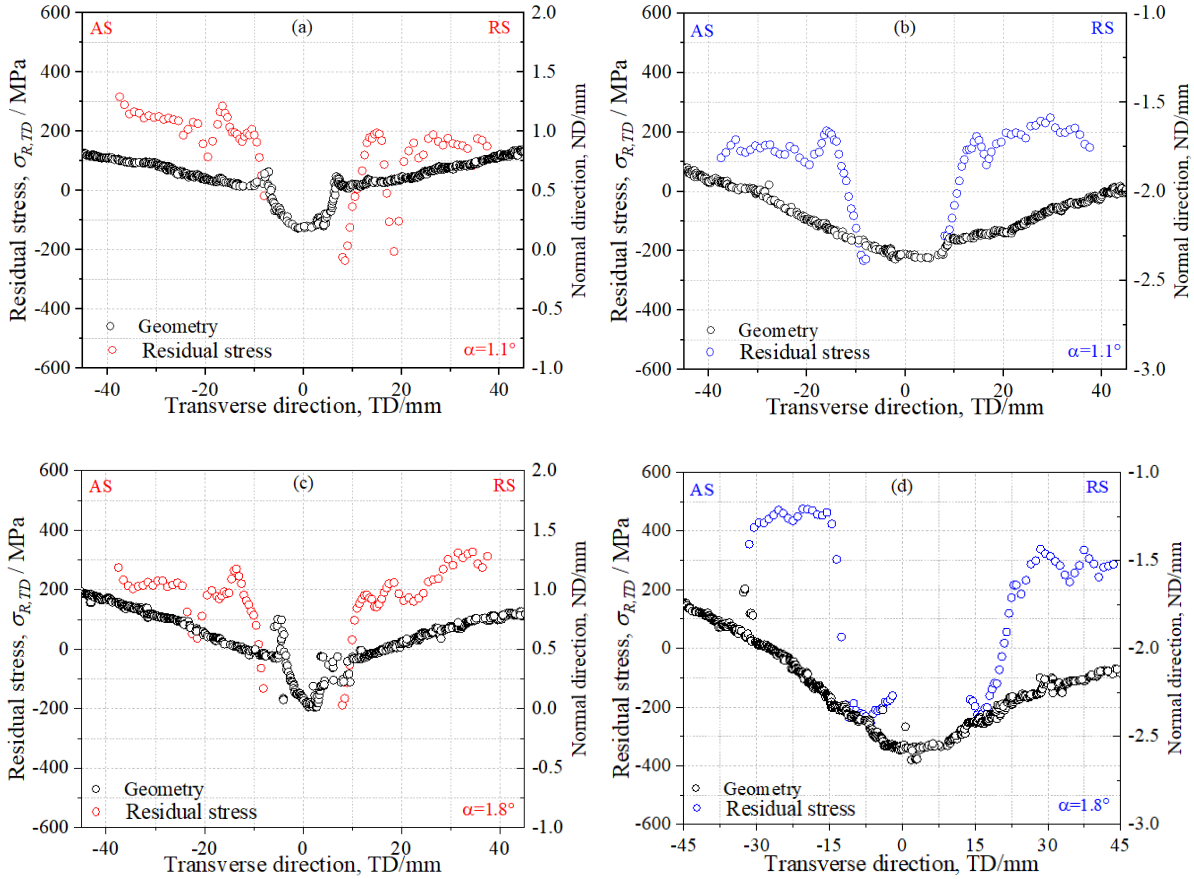

Figure 3.1 Geometry and residual stress along the center of FSW joints perpendicular to the welding direction: (a) SMA490AW on the welding surface; (b) SMA490AW opposite the welding surface; (c) SPA-H on the welding surface; (d) SPA-H opposite the welding surface;

The residual stress perpendicular to the welding direction $\sigma_{R,TD}$ was measured by XRD as seen in Figure 3.1. The residual stress distribution of SMA490AW and SPA-H on the welding surface and opposite the welding surface is very similar. The high residual compressive stress is observed near the weld, while the residual stress is increased drastically and converged in

the state of high tensile stress at the BM. The high residual tensile stress at the BM is speculated to be induced by the high heat input during the fabrication of steel plates, as the steel plates were sliced from an original thickness of 12 mm to 3 mm before welding.

3.2.2. Microstructure characteristics

Figure 3.2 shows overviews of the transverse cross sections of FSW samples of SMA490AW and SPA-H. Similar cross sections can be observed for FSW joints of both SMA490AW and SPA-H. The weldment profiles appear “basin-shaped”, which is consistent with the size of the tool probe. In each case, the joints can be split into regions including the BM, SZ, and TMAZ-AS, TMAZ-RS. The HAZ is not clear due to the low welding temperature. The steel plates were welded with fine penetration, without internal welding defects such as cracks, pores and cavities. It can be concluded that the welding speed and downward load used in this research are appropriate to provide sufficient heat input to promote the plastic flow of materials around the tool probe. The borderline between the SZ and BM can be roughly determined, and TMAZ-AS and TMAZ-RS are not perfectly symmetrical by the nugget zone. The ring vortex deformation path of material and typical onion rings of FSW welded joints can also be observed in the center of the SZ for the SMA490AW and SPA-H in this research.

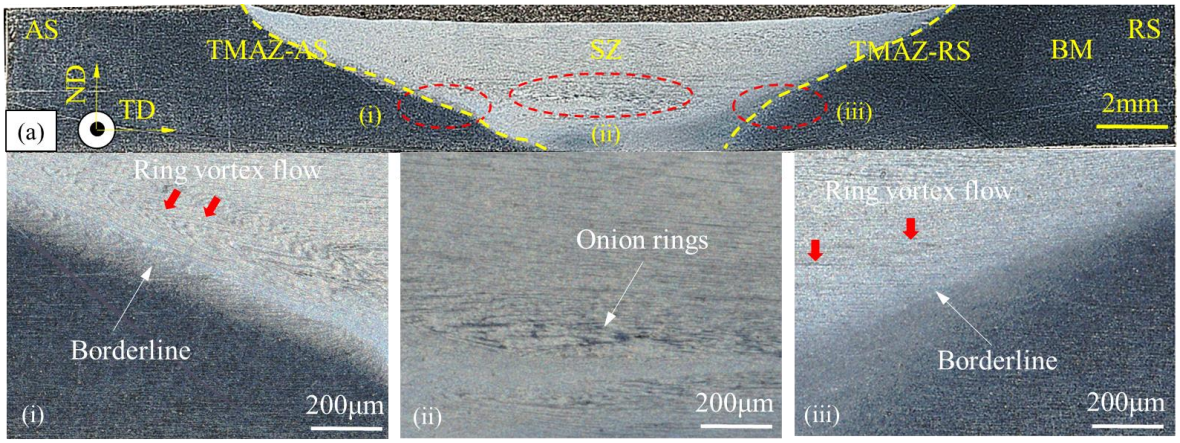

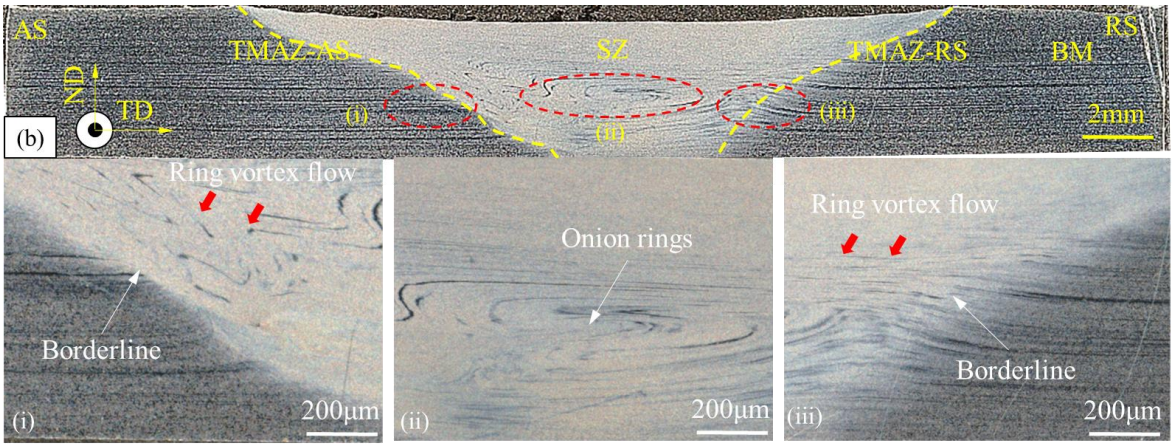

Figure 3.2 Macrostructure of transverse section of the FSW joint: (a) SMA490AW (b) SPA-H

The microstructures and EBSD inverse pole figure (IPF) of BM and SZ are indicated in Figure 3.3. The BM exhibits a typical ferrite microstructure with coarse ferrite grains, among which the stratiform pearlites are distributed. The SZ is composed of ferrite and cementites with much finer ferrite grains compared to the BM, due to the dynamic recrystallization (DRX) induced by frictional heat and severe plastic deformation. The grain size of BM is about 6~8 times larger than that of the SZ for the two studied steels based on the results of EBSD. The grain size of SMA490AW is slightly smaller than that of SPA-H at BM, SZ and TMAZ. Figure 3.3(a) and (c) show the main feature of BM with a high microstructural inhomogeneity. The EBSD map of SZ shown in Figure 3.3 (b) and (d) reveals that fine and equiaxed grains were formed in this zone.

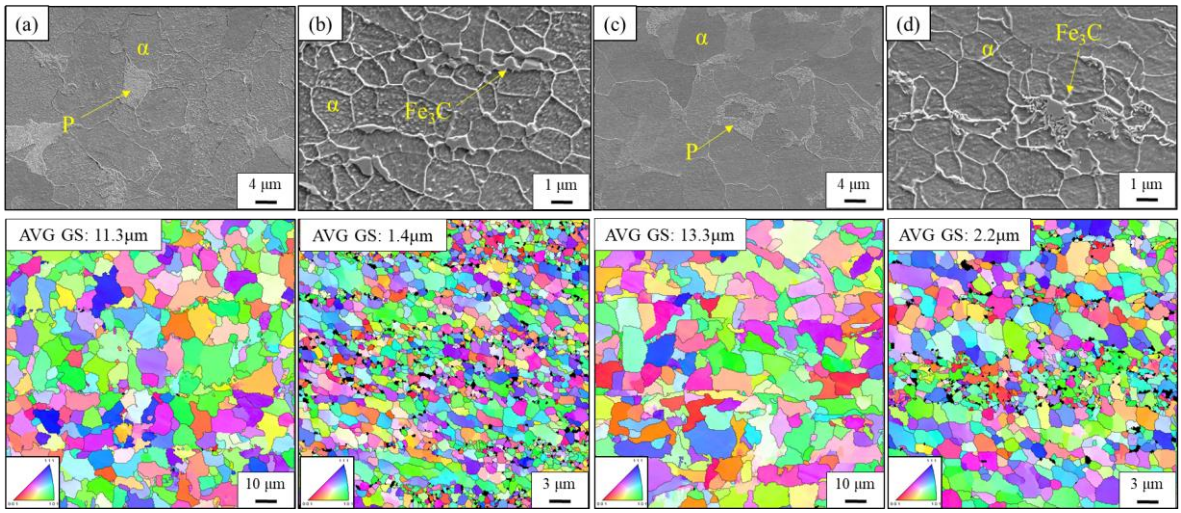

Figure 3.3 Microstructure and EBSD IPF of (a) SMA490AW-BM; (b) SMA490AW-SZ; (c) SPA-H-BM; (d) SPA-H-SZ

The SEM micrographs of transition from SZ to BM and EBSD IPF of TMAZ are illustrated in Figure 3.4. No obvious HAZ can be observed in the studied FSW joints probably because the grains near the TMAZ were not visually coarsened due to the low heat input during the welding process. There is generally a distinct boundary on the transition from SZ to BM-AS as shown in Figure 3.4(a) and (c), while the boundary is unclear on RS (Figure 3.4(b) and (d)). According to the EBSD maps, the TMAZ is characterized by the markedly rotated and elongated grains due to the plastic deformation, while a high microstructural inhomogeneity can still be observed. Similar to the boundary mentioned above, the elongation of TMAZ-RS is not as clear as on AS. This is due to the different flow behaviors of material on both sides of the rotating and travelling probe. As the probe rotation shares the same direction as the probe travelling along the steel plate, the plastic flow against the base metal on AS is more severe than that on RS. This deformation behavior results in the greater strain gradient and plastic flow on AS, illustrating the distinct boundary between the TMAZ and SZ. This also explains why borderlines of stir zone on AS and RS are not perfectly symmetrical and the area of nugget zone on AS is larger than that on RS, as seen in Figure 3.2.

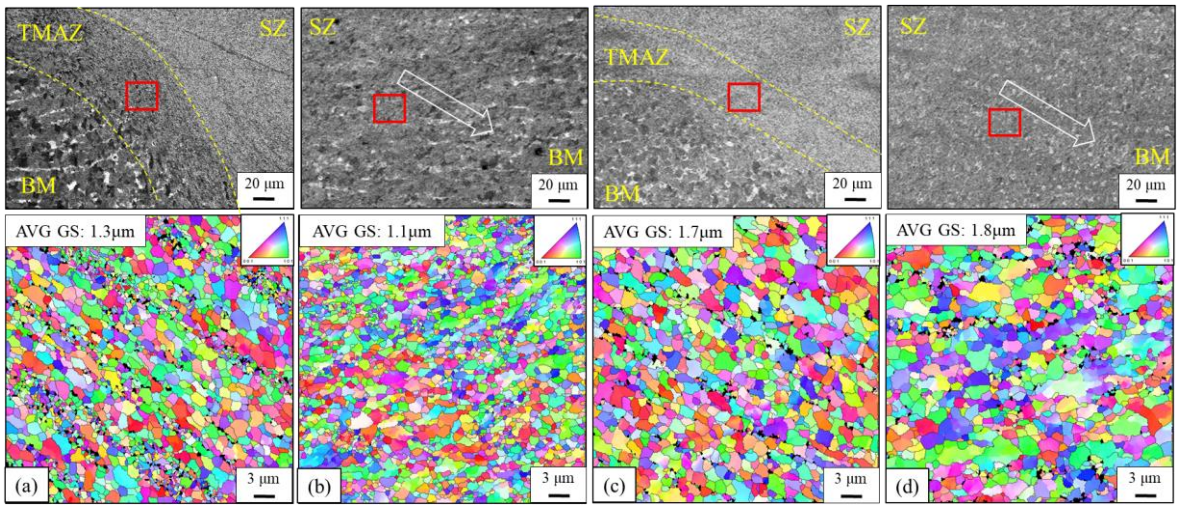

Figure 3.4 Microstructure and EBSD IPF of (a) SMA490AW-TMAZ-AS; (b) SMA490AW-TMAZ-RS; (c) SPA-H-TMAZ-AS; (d) SPA-H-TMAZ-RS

3.2.3. Microhardness distribution

The microhardness of FSW joined SMA490AW and SPA-H is summarized in Figure 3.5. Taking the center of the section as the ordinate origin, the microhardness was measured at three different depths from the FSW-processed surface (i.e., the top side, the section center and the bottom side) in the normal-transverse (ND-TD) plane.

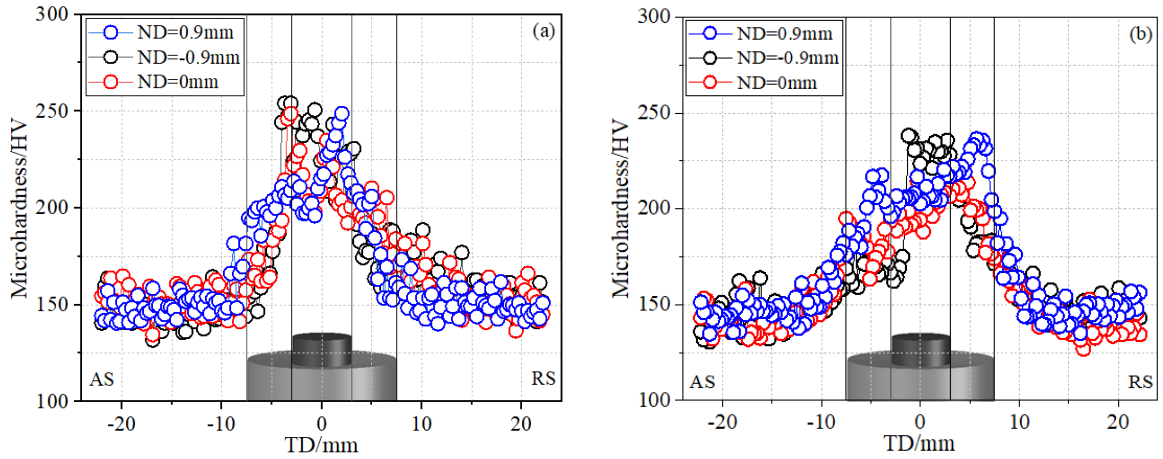

Figure 3.5 The microhardness of welded joints (a) SMA490AW; (b) SPA-H

It can be observed that both the microhardness distributions are roughly symmetrical. The microhardness of SZ is higher than that of the BM because of grain refinement. The temperature gradient at the transition from the SZ to BM results in the insufficient heat input for recrystallization of the fine grains, thus the microhardness is decreased. The grain size of SMA490AW at BM, SZ and TMAZ is slightly smaller than that of SPA-H, thus the overall microhardness of SMA490AW slightly increases compared to SPA-H. No softening of the HAZ can be observed for both the materials.

3.3. Ductile performance

3.3.1. Yield and fracture characteristics

After the monotonic loading, the engineering strain was calculated based on the

displacement field, and successive changes of strain distribution could be monitored during the yield and fracture process of four specimens. The typical local strain distribution ε_t during the loading process is illustrated in Figure 3.6. The displacement u was measured based on the change in the distance between the clamping positions of the specimen as shown in Figure 3.6, and the Load- Displacement relationship was also synchronized with the strain changes.

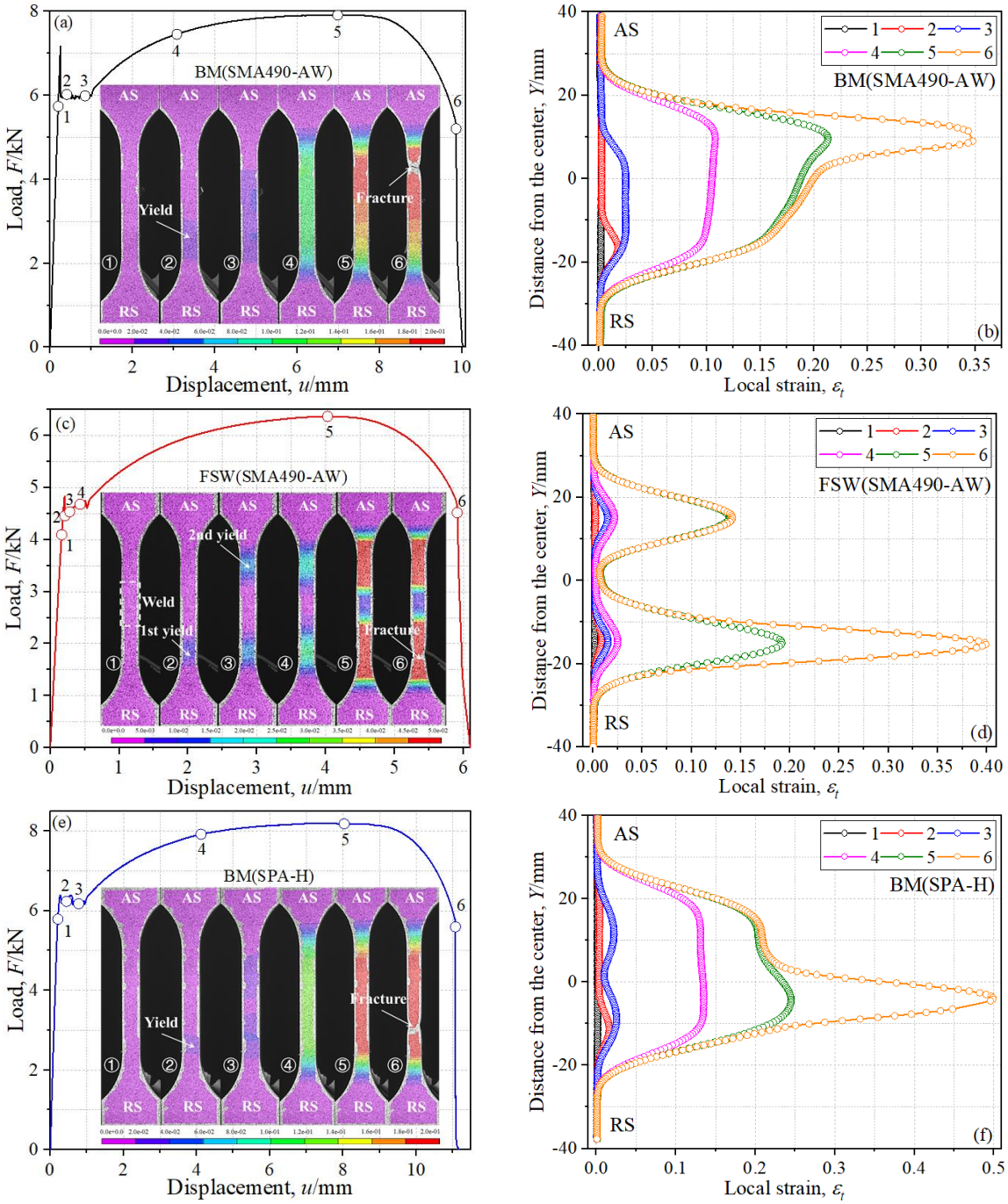

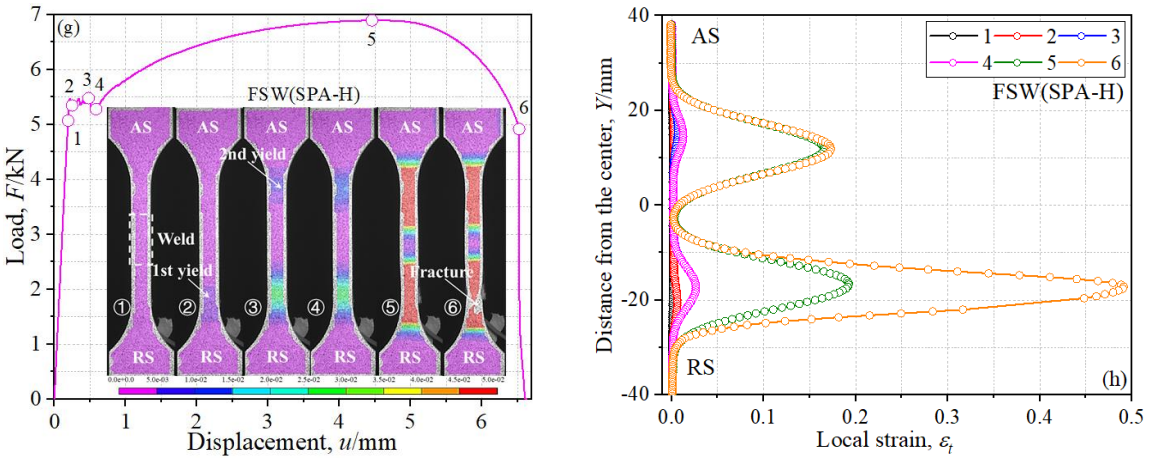

Figure 3.6 The tensile response measured by DIC for BM and FSW joints of SMA490AW and SPA-H (a) (c) (e) (g) represent the Load-Displacement curves and color-coded strain fields at separate steps, and (b) (d) (f) (h) indicate the distribution of local strain

The strain evolution of BM specimens is first discussed. As seen in Figure 3.6(a) and (c), the nominal strain was small and uniformly distributed during the elastic loading stage (1), and then great strain increment could be observed at a certain position on the parallel part of the specimen, indicating the beginning of yield (2). The position where the yield initiated could be decided by several factors, including the surface condition, interior impurities and initial deformation due to the chucking. Next, the plastic deformation was developed in the whole parallel part during the yield stage (3), after which the hardening began and the strain was further increased (4). The strain was unevenly distributed on the specimen when the tensile strength was reached (5) and the specimens fractured from the position with the greatest deformation (6).

Unlike the BM specimens, the FSW specimens experienced two yield steps. As seen in Figure 3.6(b), and (d), after the elastic loading (1), the first yield happened on the base metal on RS (2). The plastic deformation was then developed towards both sides and stopped after contacting the weld and bottom flange of the specimen (3). Along with the first yield, the first hardening could be observed from the Load- Displacement relationship, and the plastic deformation of the yield part was also increased. Next, the second yield could be observed on the BM-AS (4), after which the second hardening started and the plastic deformation was further increased on both RS and AS (5). At the hardening stage, the portion of the weldment

where plastic deformation happened was increased, while the core of the weldment was still in the elastic condition, even when the specimen was fractured (6).

The two steps of yield happening in the FSW specimen result from the great micro-hardness and strength of the weld. For the BM specimens, the yield happened at the weakest spot of the parallel part with unfavorable initial deformation or surface condition, and then propagated to other regions quickly as the yield point is successively achieved on the remaining part of the specimen. In the FSW specimen, the grain size of BM is usually greater than that of SZ and TMAZ, resulting in a lower yield and tensile strength at BM. The BM-RS yielded first in this study. The weld with high hardness and strength served as an obstacle to prevent the further development of plastic deformation to other regions of the specimen. The load was increased with the hardening of the base metal on RS until yield strength of the base metal on AS was also achieved, which resulted in the second yield as seen in Figure 3.6(c), and (g).

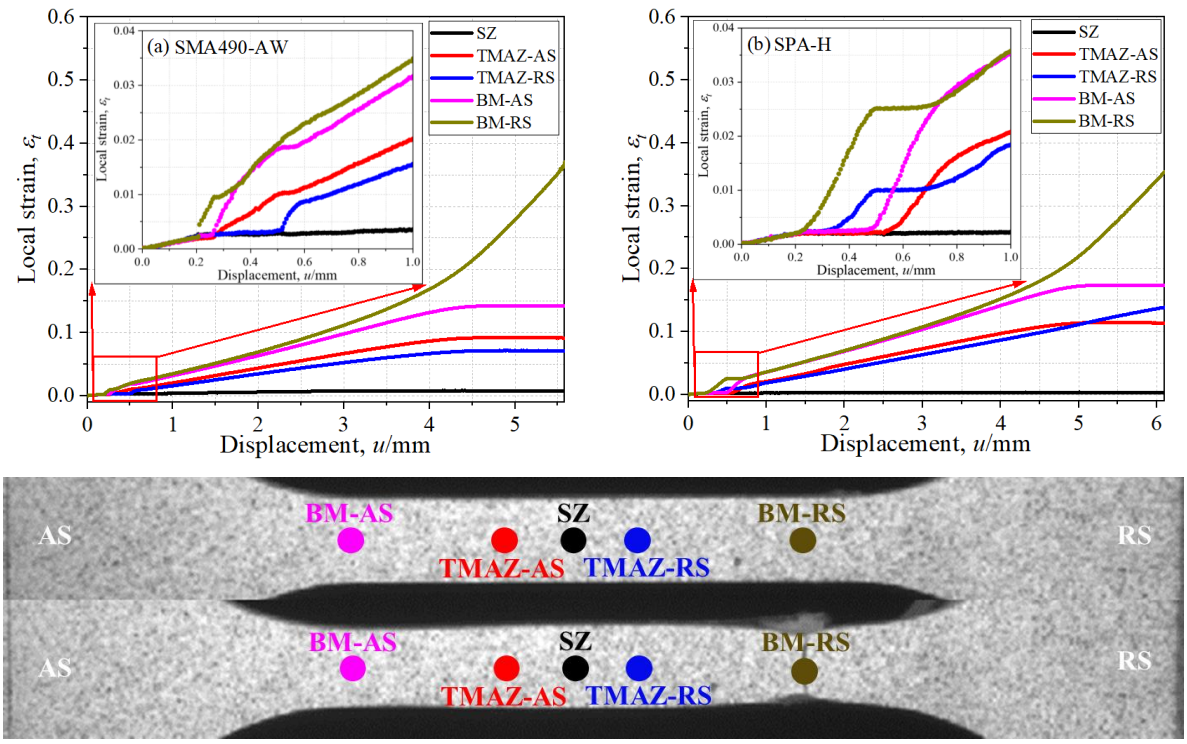

Figure 3.7 The strain increment of critical points (a) SMA490AW-FSW; (b) SPA-H-FSW

The strain increment of critical spots for FSW specimens is also summarized in Figure 3.7. The relative change of SZ, TMAZ-AS, TMAZ-RS, BM-AS and BM-RS at the yield stage is magnified. Overall, the first yield and fracture occurred at the BM-RS and the second yield

at the BM-AS as discussed above, while the sequences of yield for the TMAZ-AS and TMAZ-RS were somewhat different due to the different plastic slip rate. As for the SMA490AW, the rate of plastic deformation developing from the BM-RS to the TMAZ-RS was slow, so that the BM-AS and TMAZ-AS were successively yielded before the yield of TMAZ-RS. A different phenomenon could be observed for the SPA-H: the TMAZ-AS yielded quickly after the yield of BM-AS, followed by the plastic deformation of BM-AS and TMAZ-AS. At the fracture stage, the increase of plastic strain on AS was stopped because the loading had leveled off or tended to decrease and no more hardening could continue, while the slip rate on RS kept increasing as the section was necking. The strain of the weld nugget was barely changed due to the high strength throughout the whole loading process.

3.3.2. Yield and fracture mechanism

As seen in Figure 3.6, the first yield happened on the BM-RS, the second yield on the BM-AS and the final fracture on the BM-RS for the two kinds of FSW joints in this research. A question might occur as to whether it is accidental or could be explained by a certain mechanism. The efforts in this section are to ascertain a reasonable explanation for this phenomenon. Taking the SPA-H for example, Figure 3.8 illustrates the microhardness distribution in the FSW specimen at the processing side (TD = 0.9mm), which is extracted from Figure 3.5. It can be observed that the slope of microhardness changing from SZ to BM is sharper on RS than AS and the weld nugget is generally harder on RS. Considering the geometry of the specimen, the weld nugget on AS with lower microhardness can join BM-AS to resist the load, while weld nugget on RS is too strong to share the similar deformation as BM-RS. Therefore, the specimen is more likely to yield and fracture on the BM-RS, based on the above analysis.

To verify the validity of this speculation, the finite element (FE) model was built based on the FSW specimen by ABAQUS v6.14-3. The bilinear plastic material model was used for the base metal which was constituted of the yield strain, yield stress, fracture strain and fracture stress obtained from the experimental data in Section 3.3.1. To simulate the FSW joint with various micro-hardness as accurately as possible, the FE model of weld including the SZ and

TMAZ was partitioned by small chunks with length of 1mm, as seen in Figure 3.8. The microhardness of SPA-H for different regions was linearly fitted, so that each chunk had an identical micro-hardness, by which the yield stress could be calculated based on Equation (3.1) [150]. As there is no information for the fracture strain and fracture stress of weld with various regions, it is assumed that the weld is characterized by the linear isotropic hardening and shares the same slope as the base metal. The material models are illustrated in Figure 3.9. The FE model was built by the full-integration solid element C3D8 with a fine element size of 0.5mm. The FE model featured a total element number of 185,320 and node number of 209,594. All the freedoms of the section on RS are fixed and the loading is conducted on the AS section.

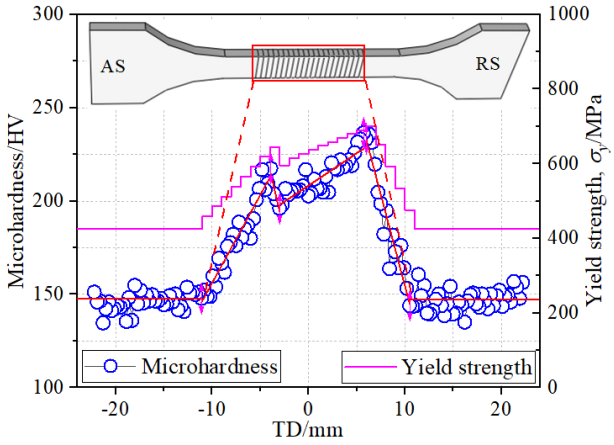

Figure 3.8 Fitting of microhardness

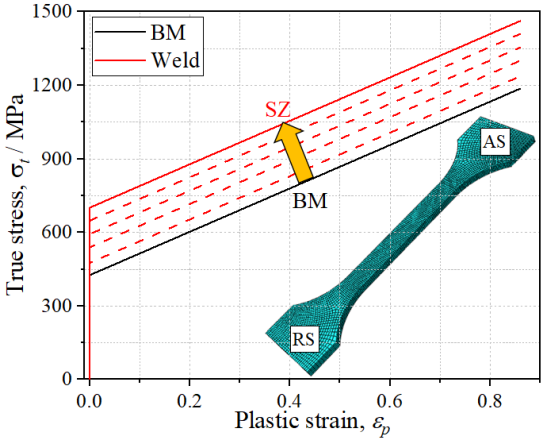

Figure 3.9 Material model

$$\sigma_y = 3.06Hv \tag{3.1}$$

Due to the simplification of the material model, the result of FE analyses cannot be compared to that of the experiment quantitatively. A qualitative comparison was carried out on three conditions including the first yield, the second yield and fracture (necking). Besides, the FE model with the same hardness distribution on AS and RS was also added for reference, as seen in Figure 3.10.

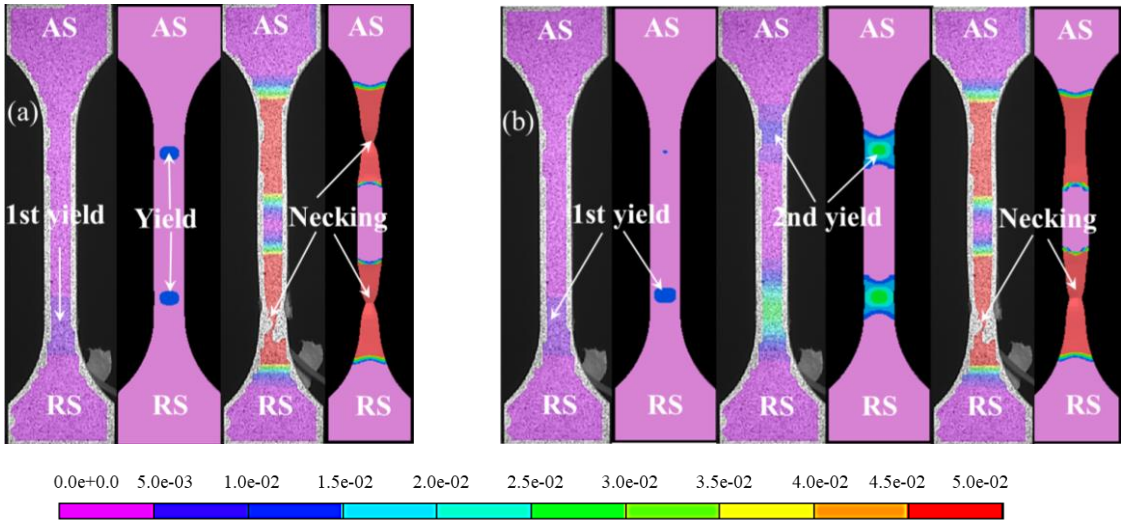

Figure 3.10 Comparison of strain distribution by FE model and experiment (a) The even hardness distribution; (b) The uneven hardness distribution

As seen in Figure 3.10(a), the yield happens simultaneously on AS and RS for the FE model with the even hardness distribution, as also for the necking that occurs in the base metal at both AS and RS, which is quite different from the conditions in the real tests. By imposing a larger slope of microhardness variation on RS, the high microhardness of weld nugget on RS cannot share the similar deformation as BM on RS, inducing the first yield and fracture on RS with smaller stiffness. As seen in Figure 3.10(b), the results of FE analyses share the same trend as the experiment. Therefore, it can be concluded that the uneven distribution of microhardness results in the first yield and fracture on RS in this research.

3.3.3. Tensile properties

The nominal strain- stress relationship of all specimens is illustrated in Figure 3.11. The nominal strain was defined by the elongation of the parallel part (35mm) of the specimen. The fracture strain of the base metal specimen is larger than that of the FSW specimen, because the weld part of the FSW specimen is barely elongated, and the deformation is mainly contributed by the base metal part of the specimen. Thus the FSW process weakens the performance of plastic deformation as conventional joining techniques. As discussed in Section 3.2.3, the microhardness of SZ is higher than that of the BM and there is no softening of the HAZ due to

the adequate heat input, so the tensile strength of FSW specimen is dependent on the part of the base metal. Therefore, the tensile strength of FSW specimens can be higher than that of the BM specimens, as seen in Figure 3.11 and the 100% joint efficiency for both materials is achieved. The mechanical properties of FSW joints for the two materials are also compared in Figure 3.12. The SPA-H illustrates a more favorable strength and ductile property than SMA490AW. As the corrosion resistance index I of SPA-H is also higher than that of SMA490AW, the steel SPA-H welded by FSW can ensure both favorable mechanical properties and anti-corrosion performance.

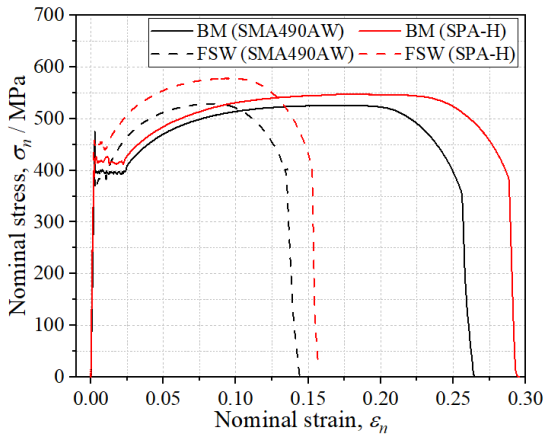

Figure 3.11 Nominal stress - strain relationship

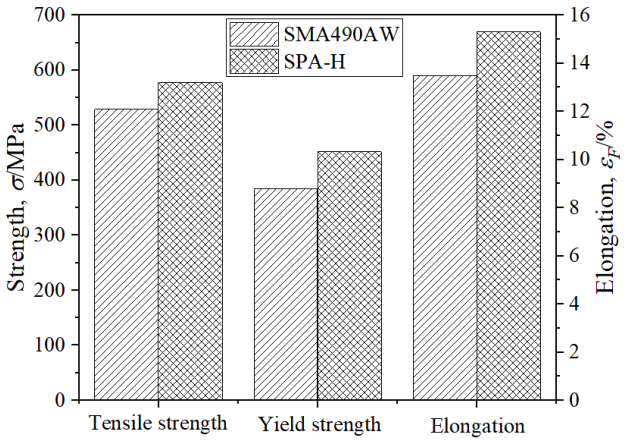

Figure 3.12 The mechanical properties of FSW joints

The ductile fracture of BM specimens and FSW specimens occurred at the base metal as seen Figure 3.13. The fracture surface for each specimen was observed by SEM. All the fracture surfaces of the tensile-tested specimens displayed similar characteristics including the BM specimens and FSW specimens. This is reasonable because all the specimens were fractured at the base metal region, far from the weld and exhibited ductile behavior according to the stress-strain relationship and elongation. The fracture surface of FSW joints of SPA-H is illustrated in Figure 3.14(a) as an example, which is characterized by the obvious necking and fibrous surface. The coarse and fine dimples as seen in Figure 3.14(b), approximately equiaxial, reveal the favorable ductile behavior of weld joints by FSW.

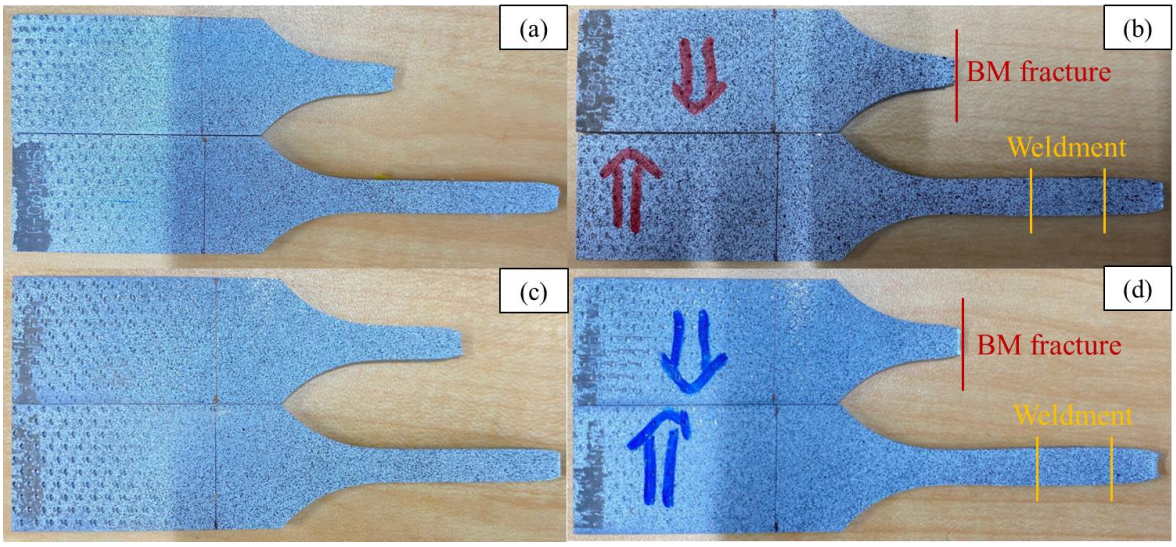

Figure 3.13 Fracture position of BM and FSW specimens (a) SMA490AW-BM; (b) SMA490AW-FSW; (c) SPA-H-BM; (d) SPA-H-FSW

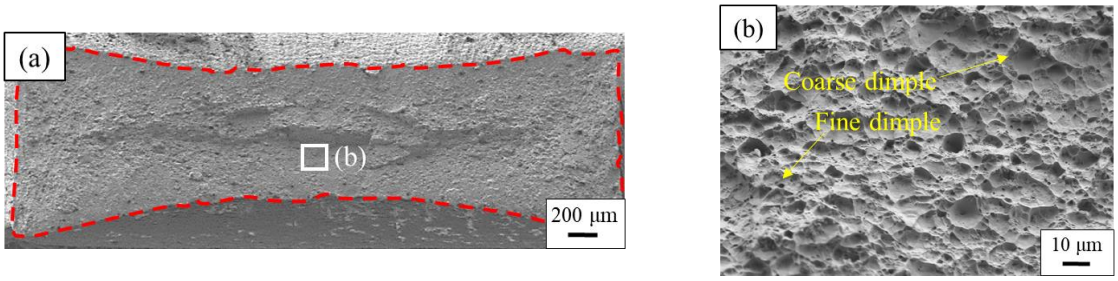

Figure 3.14 Fracture surface of FSW joints of SPA-H (a) Overview of surface (b) Surface microstructure

3.4. Fatigue performance

3.4.1. Fatigue strength

The fatigue experiment was carried out on a total of 24 BM and FSW specimens of SMA490AW and SPA-H. The specimens were defined to be running out when the fatigue fracture life $N_f > 2 \times 10^6$. The applied stress range was decided to result in the high-cycle fatigue regime for all specimens. All the FSW specimens fractured at the BM region which was far from the SZ and HAZ, indicating a favorable fatigue strength of the welded joints. Figure 3.15 shows the stress range $\Delta\sigma$ and fatigue fracture life N_f relationship of the FSW specimens, compared to the BM specimens. The recommended S-N curves (IIW-FAT112) for the welded

plates with weld reinforcement removed were added for reference, according to IIW [151]. It is observed that the data points of FSW and BM specimens are scattered together and illustrate similar fatigue strength. Therefore, the data points of the BM specimens and FSW specimens were fitted as a whole by the least square method, and the fatigue strength (FAT) was defined by the stress range $\Delta\sigma$ at $N_f = 2 \times 10^6$ cycles. The S-N curves considering 97.7% and 2.3% survival probability were also included in Figure 3.15 according to the IIW design recommendation. Figure 3.15 shows that the slope m of the S-N curves for the studied steels is much flatter compared to the design curves, and almost the same for the two materials. The fatigue strength of the studied steels is generally higher than the design curves, especially for the high-cycle fatigue region.

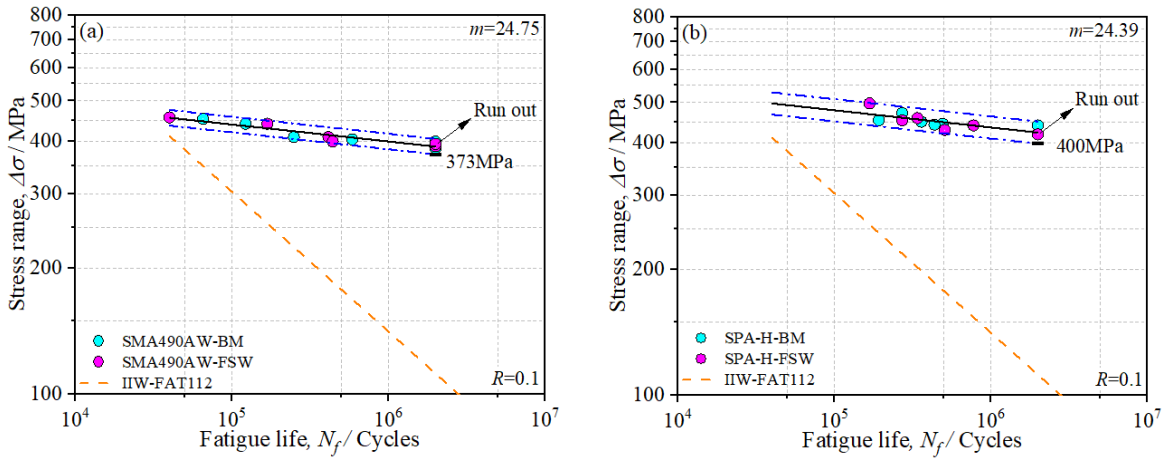

Figure 3.15 The *S-N* curves (a) SMA490AW; (b) SPA-H

Figure 3.16 compares the fatigue strength (represented by the stress range, $\Delta\sigma$, corresponding to the fatigue fracture life $N_f = 2\times10^6$) and yield stress σ_y (corresponding to 0.2% plastic strain) relationship of the BM and FSW specimens to IIW (FAT112). The fatigue strengths of the BM and FSW specimens in Figure 3.15 were fitted separately to assess the weldability of FSW below the temperature A_1. The fatigue tests of steels with different chemical compositions (DH-36, S690QL, 409M, S690, S355) joined by FSW were also illustrated for comparison [136,139,152-154]. It is observed that the steels joined by FSW in this research or from the references all illustrate higher fatigue strengths compared to the design curve (FAT112). The fatigue strengths of FSW and BM specimens of the steel SMA490AW

and SPA-H in this research are almost the same, while the decreasing fatigue strengths of FSW joints compared to the base metals were observed for the steel S355 and S690QL, which is especially drastic for the steel S690QL. The decreasing fatigue strength of FSW joints of the steel S690QL results from the HAZ softening because the crack usually initiates from the partially recrystallized zone in the HAZ, which exhibits a sharp drop of hardness [136]. The fatigue strengths of FSW joints of the studied steels in this research are generally higher than those from the references. Comparing to the joining conditions and geometry conditions in the references (S355, 409M, DH-36, S690, S690QL), it is concluded that the fatigue strengths of the FSW joints in this research are higher because the FSW joining parameters resulted in a welding temperature below A_1, thus the HAZ softening was inhibited in the welded joints. Moreover, the specimens were finely ground and polished to eliminate geometric discontinuities. The evidence is that the cracks initiated at the root of weld joint or the spot with HAZ softening for many specimens from the references.

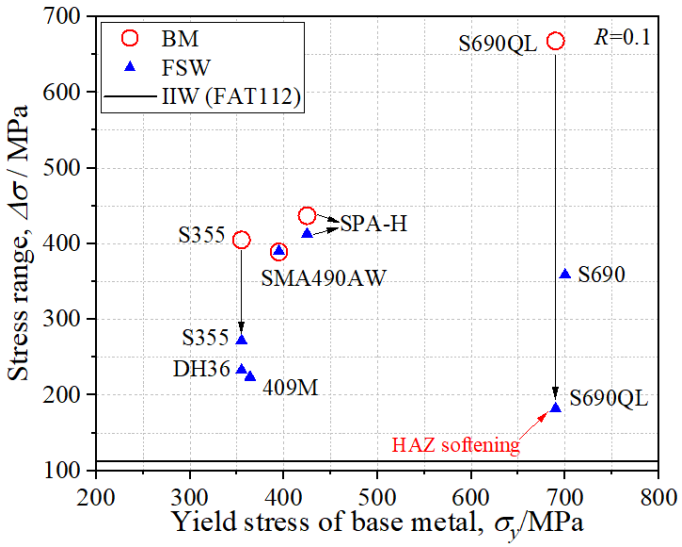

Figure 3.16 The fatigue strength - yield stress relationship

3.4.2. Ratcheting behaviors and fractography

The displacement history of all specimens was recorded during the fatigue loading so the ratcheting behaviors could be analyzed. Figure 3.17(a) and (b) illustrate two types of ratcheting

behaviors observed in this research, both obtained from the BM specimens of SMA490AW. The breaking point of each line was taken within the 2000 cycles before the final fracture. Type (1) illustrates a continuous and stable increase of ratcheting strain, followed by plasticity instability during a comparatively long fatigue life period, which is 22% of the full life for the specimen as seen in Figure 3.17(a). The large accumulation of ratcheting strain causes the necking and lower fatigue life, which results from the high maximum stress (95.9% of tensile strength). As the applied maximum stress is close to the tensile strength, certain local necking occurs at the spot ready to fracture, which makes the plastic deformation easier to accumulate. The large elongation during the plasticity instability can be mostly contributed by the necking spot, resulting in a ductile fracture as seen in Figure 3.18. The letters a and b in Figure 3.18 referred to the position where the microstructure was observed by SEM, so were the same for the letters in Figure 3.19. The fracture surface of Type (1) is fibrous-shaped with no obvious radial texture and shear lips (Figure 3.18(a)). A few fatigue striations with smooth texture and secondary cracks are observed among the fibrous texture in Figure 3.18(b), which are induced by the extrusion and intrusion of the fracture surfaces during the cyclic loading.

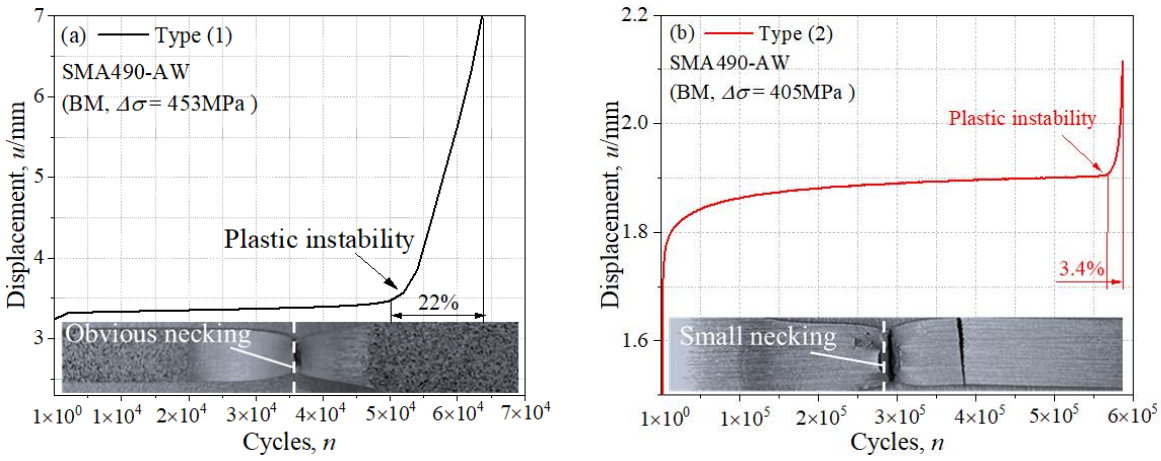

Figure 3.17 The typical ratcheting behaviors: (a) Type (1); (b) Type (2)

Type (2) shows a continuous accumulation of ratcheting strain which is the same as Type (1), while the plasticity instability occupies only an extremely small proportion of the whole fatigue life (3.4% of the fatigue life for the specimen in Figure 3.17(b)). Type (2) often occurs for the high cycle fatigue or severely cyclic hardened materials, and the small necking as seen

in Figure 3.17(b) results from the final plasticity instability. The fracture surface is usually characterized by the crack propagation region with ellipse shape and final ductile fracture with fibrous texture. As seen in Figure 3.19, the crack initiation occurs on the surface of the specimen due to the higher degrees of freedom for extrusion and intrusion, and the slip is easier to occur on this position. Deep straight dimples along the rolling direction are observed on the final ductile fracture surface, surrounding which are the fine equiaxed dimples as seen in Figure 3.19(a). The white plateau indicating the crack growth direction is shown in Figure 3.19(b), perpendicular to which are the crack arrest marks known as tyre tracks (fatigue striations). The crack initiation spot with an elliptical shape is observed in Figure 3.19(c). The surface is dominated by the transgranular fracture, and the fatigue crack can deflect at grain boundaries as seen in Figure 3.19(d).

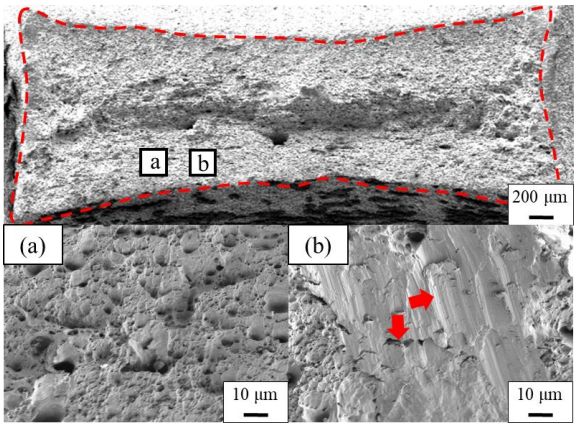

Figure 3.18 Fracture surface of ratcheting Type (1)

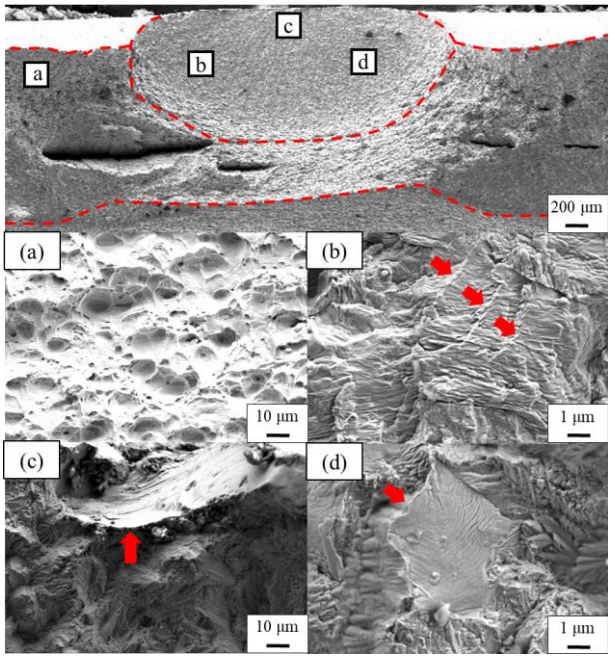

Figure 3.19 Fracture surface of ratcheting Type (2)

3.4.3. Strain accumulation of SZ, HAZ and BM

The DIC measurement was conducted on the surface of FSW specimens of SMA490AW and SPA-H during the first 10 cycles to study the cyclic plastic deformation. The specimens

were named SMA490AW-1 and SPA-H-1, both loaded by the peak stress of 95.9% tensile strength in the static test. The nominal stress - nominal strain relationship of the first 10 cycles and corresponding strain distribution measured by DIC are shown in Figure 3.20(a) and (c). The contours of strain deformation before the first yield, at the first yield, at the second yield and at the peak stress of Cycle 1 were marked by stage 1~4, respectively. The nominal strain in these two figures was defined by the total elongation of the parallel part of the specimen (35 mm), which illustrated the strain variation of the parallel part as a whole, and neglected the deformation behavior of different regions. i.e., the BM, SZ and HAZ. Two steps of yield are observed at stages 2 and 3 for both materials, and the yield started from the BM of the specimen to the SZ. Two reasons can explain the two steps of yield at the welded joint. Firstly, the SZ with high hardness can be deemed as a fixed end, and the distance from the flange of the specimen to the SZ decided the stiffness of the top and bottom parallel parts. Although the chucking distance was set to be the same in the fatigue experiment, the distance between the clamp and SZ at top and bottom sides was more or less different due to the visual error during the chucking. Moreover, the microhardness distribution is not perfectly symmetrical, as seen in Figure 3.5, and accounts for the stiffness difference. As the region with smaller stiffness often exhibits larger deformation under the same loading and tends to yield first, there is a sequence of yield for the top and bottom BM regions. Secondly, when the yield occurs on one side, the SZ with high hardness serves as an obstacle and prevents the successive plastic deformation from the yield spot to the whole parallel part. The nominal strain of SZ was obviously smaller than that of BM when the peak stress was reached, as seen at stage 4.

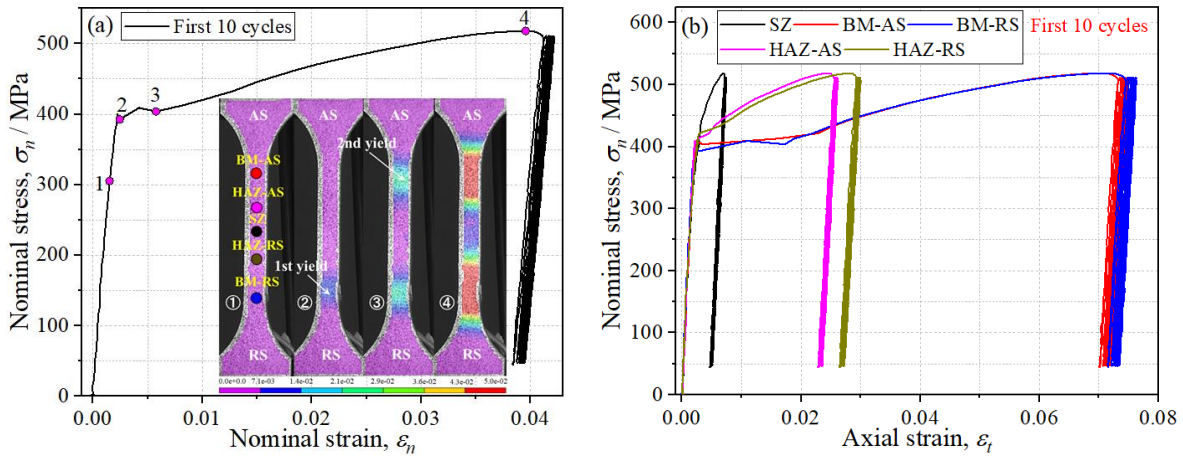

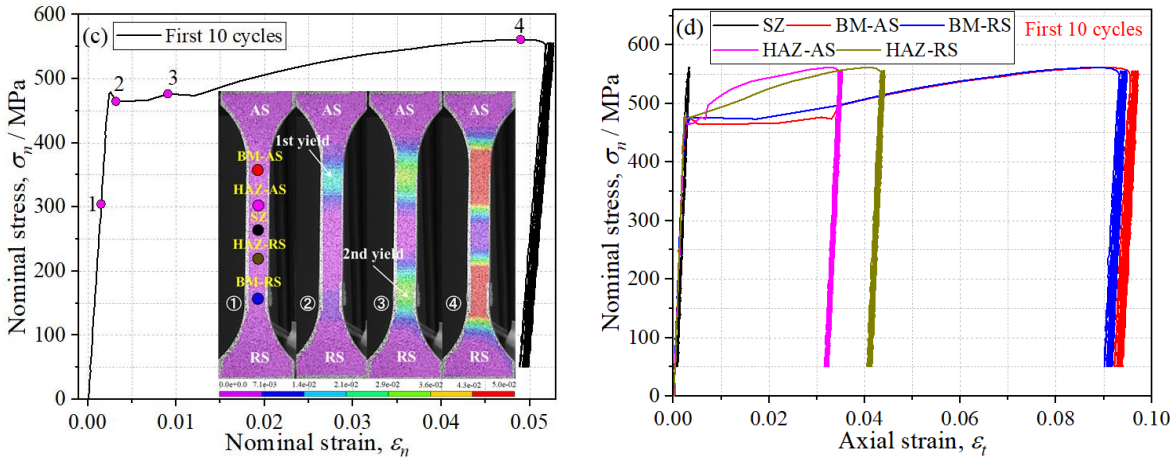

Figure 3.20 Cyclic deformations during the first 10 cycles: (a) Nominal S-S curve of SMA490AW-1; (b) Nominal S-Axial S curves of SMA490AW-1; (c) Nominal S-S curve of SPA-H-1; (d) Nominal S- Axial S curves of SPA-H-1

To investigate the cyclic deformation behavior of different spots (SZ, BM-AS, BM-RS, HAZ-AS, HAZ-RS), the axial strains of the first 10 cycles of specimen SMA490AW-1 and SPA-H-1 are illustrated in Figure 3.20(b) and (d). For specimen SMA490AW-1, yield is observed at each spot, while no obvious yield plateau occurred at SZ. The yield behavior of SZ is similar to that of the high-strength steel due to the high microhardness. The BM illustrates the obvious yield plateau, and the HAZ behaves as a transition from BM to SZ with a shorter plateau. For specimen SPA-H-1, no obvious plastic deformation is shown at SZ. As the two specimens were loaded by the same peak stress characterized by the same ratio of the respective tensile strength, the SZ of SPA-H is indicated to have a higher strength increment than that of SMA490AW. The large strain accumulation of BM is observed at the first 10 cycles for the two specimens, while that of SZ and HAZ is much smaller. The ratcheting strain of different spots explains why the fatigue fracture occurs in the BM region of all FSW specimens. As the strain accumulation of the weld is much smaller than base metal and no defects or HAZ hardening exist, the fatigue life of the FSW specimens depends on the BM region instead of the SZ or HAZ, which results in the similar fatigue strength for the FSW specimens and BM specimens as mentioned in Section 3.4.1.

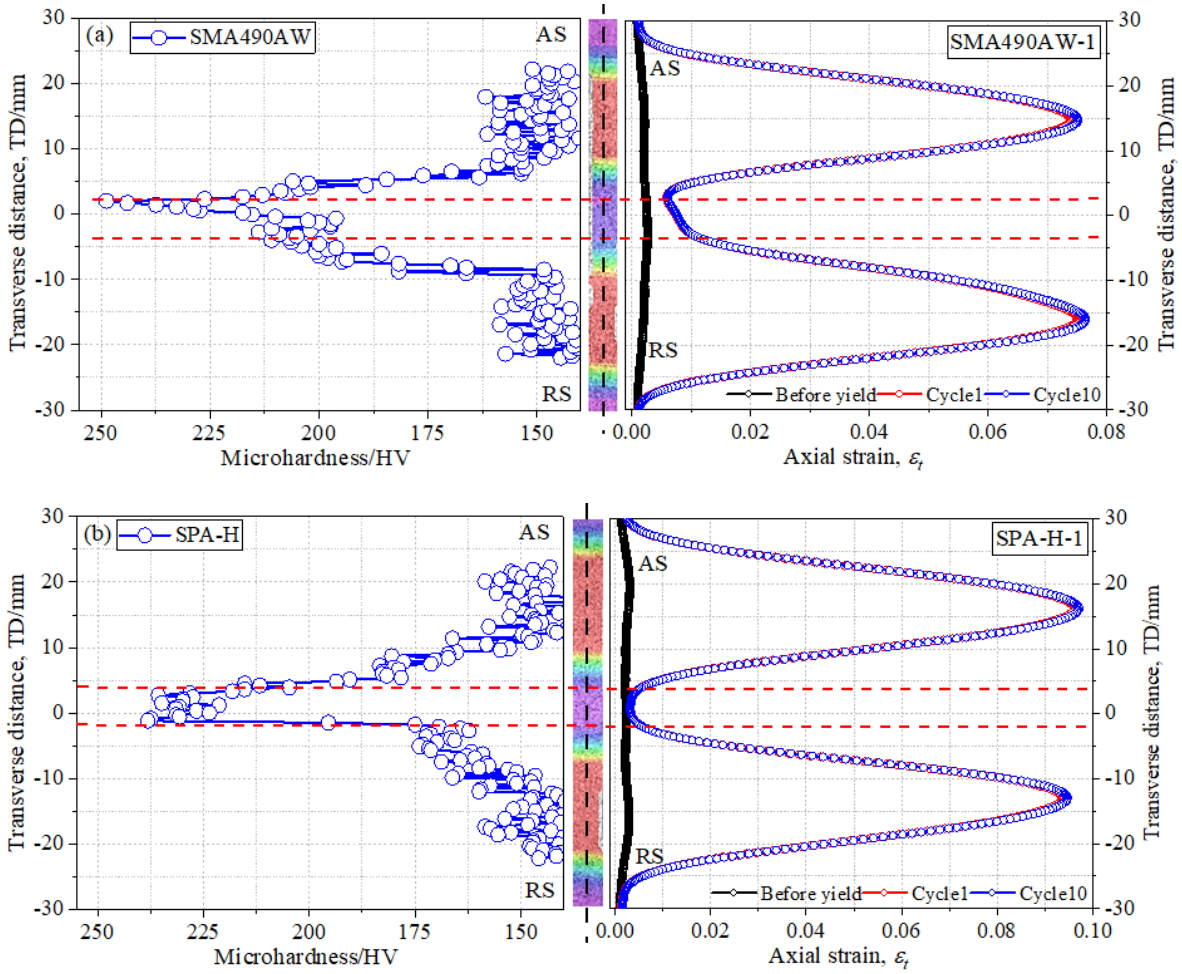

Figure 3.21 The axial strain corresponding to the microhardness distribution: (a) SMA409AW-1; (b) SPA-H-1

The axial strain along the transverse direction of two FSW specimens is illustrated in Figure 3.21. The strain contour at Cycle 10 is also added for reference, and the contour level is the same as that in Figure 3.20. The strain distributions before the yield, at Cycle 1 and 10 are summarized, and it is observed that the axial strain is roughly symmetric to the center of the weld nugget. The plastic deformation is mainly accumulated at Cycle 1 and no obvious strain increment is found at Cycle 10, except for the center of BM region. For specimen SMA490AW-1, the weld nugget was also yielded together with the HAZ and BM, while the strain distribution was inclined to AS due to the asymmetric microhardness. With reference to the microhardness distribution, the peak microhardness of SMA490AW is not at the center of the weld nugget. The decline rate of microhardness is comparatively smaller at the beginning on RS and then drops at the same rate as AS. Therefore, an inflection point at the weld nugget is observed for

the strain distribution. For specimen SPA-H, the microhardness is symmetric to the weld nugget, thus the strain distribution is also symmetric. Although the peak microhardness of SMA490AW is higher than that of SPA-H, the wider area with high microhardness at the weld nugget is observed for SPA-H, thus the strain response is still elastic for the core of the weld nugget.

3.5. Conclusions

In this chapter, conventional weathering steels SMA490AW and SPA-H were joined by FSW below the A_1 temperature. The microstructure characteristics and mechanical properties of weldments were investigated. The cyclic behaviors of different regions (BM, SZ, HAZ) under the fatigue loading were studied, and the fatigue strength was compared to the design curve and fatigue tests from the references. The specific conclusions are as follows:

(1) Joints with no defects are obtained for both conventional weathering steels (SMA490AW and SPA-H). SZ is characterized by fine-grained ferrite with strengthening phase cementite. TMAZ is streamlined against the SZ and grains are significantly elongated. No softening is observed at HAZ by the microhardness assessment.

(2) A distinct boundary between the TMAZ and SZ on AS is observed, while the boundary is unclear on RS due to the different flow behaviors of the material at both sides. This also explains why the nugget zone on AS is larger than that on RS.

(3) The FSW joints experienced two steps of yield under the monotonic loading due to the high microhardness and strength of weldment. The yield and fracture both happened at the base metal region on RS of the specimen due to the uneven distribution of microhardness, and the weld nugget was still in the elastic condition, even when the specimen was fractured.

(4) The joint efficiency of SMA490AW and SPA-H by FSW can be as high as 100%. Sound ductile behavior is observed for both materials, while the SPA-H with higher P composition and corrosion resistance index illustrates a more favorable strength and ductile property than SMA490AW.

(5) Two steps of yield are also observed for the FSW specimens in the first cycle of the fatigue loading, due to the high microhardness of SZ which served as an obstacle and prevented the successive plastic deformation from the yield spot to the whole parallel part.

(6) The yield plateau is obvious in the BM region of the FSW specimen, and cannot be observed at SZ with high microhardness and small elongation. The HAZ behaves as a transition from BM to SZ with a shorter plateau. The ratcheting deformation of SZ is also smaller than those of BM and HAZ.

(7) Two types of ratcheting behaviors are observed for the studied weathering steels. The high peak stress results in the plasticity instability which covers a comparatively larger proportion of fatigue life, and a ductile fracture surface is illustrated. The low peak stress causes a short plasticity instability, and a fracture surface is characterized by an ellipse-shaped crack propagation area with obvious tyre tracks.

(8) The BM and FSW specimens of weathering steels have almost identical fatigue strength due to the absence of HAZ softening and notches, indicating a favorable weldability. The slopes of the *S-N* curves for the two materials are rather flat, compared to the recommended design curve FAT112. The fatigue strength of the welded joints is higher than the design value assessed by the nominal stress.

Chapter 4.

High-phosphorus weathering steels joined by friction stir welding

4.1. Introduction

The conventional weathering steels SMA490AW and SPA-H were successfully joined by FSW below A_1 temperature, and the favorable ductile and fatigue performance were confirmed (see Chapter 3). Since FSW has been proved to successfully join conventional weathering steels, it is expected that FSW can join weathering steels with higher wt.% P without solidification cracks, and achieve a stronger anti-corrosion performance at the same time. Therefore, the new weathering steels with higher wt.% P (as high as 0.3% P) were developed and also joined by FSW below A_1 temperature (see Chapter 2). The geometry characteristics and residual stress of the high-phosphorus weathering steels joined by FSW were measured and compared to conventional weathering steels. Influence of wt.% P and other alloying elements on the microstructure and microhardness of FSW joints was analyzed. The yield and fracture characteristics were observed by DIC. The monotonic and fatigue tests were carried out on the finely polished FSW specimens to obtain the tensile and fatigue strength. During the optimization of welding parameters, some FSW joints with solidification cracks were also obtained. The influence of solidification crack on tensile and fatigue strength of FSW joints was finally studied by comparing to those without defects.

4.2. Residual stress, microstructure and microhardness

4.2.1. Geometry and residual stress

The angular distortion α of conventional and high-phosphorus weathering steels perpendicular to the welding direction was measured by VL-500. The relationship of angular distortion to wt.% P is shown in Figure 4.1. It is observed that a higher wt.% P can result in larger angular distortion according to the experiment results in this research.

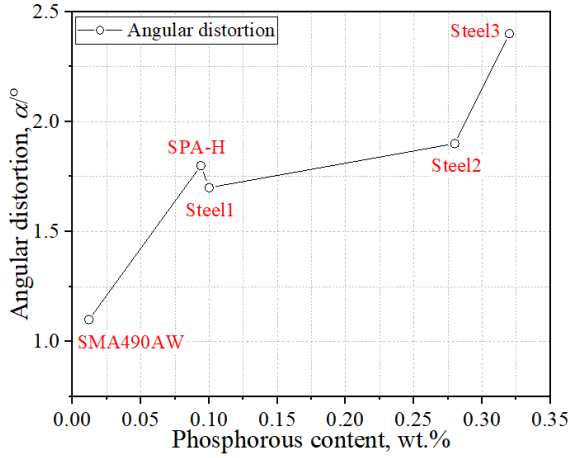

Figure 4.1 Relationship of angular distortion to phosphorus content

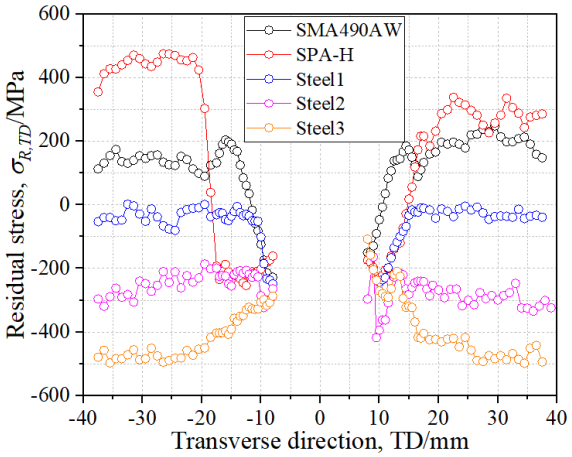

Figure 4.2 Residual stress of FSW joints of different steels

The residual stress $\sigma_{R,TD}$ of FSW joints of five weathering steels studied in this research was shown in Figure 4.2. The high residual compressive stress can be observed for five weathering steels due to the high downward load during the welding. However, the residual stress far from the weldment is very different between the studied steels due to the different processing of base metals. SMA490AW and SPA-H were sliced from thickness of 12 mm to 3 mm before welding, and the high heat input during the fabrication of BM possibly resulted in the high residual tensile stress. Different from the conventional weathering steels, the ingot of Steel1 and Steel2 was hot-rolled to the thickness of 3 mm at the expected temperature of 1000°C followed by heat treatment at 1000°C for 15 minutes. The ingot of Steel3 was hot-rolled to the thickness of 3 mm at the expected temperature of 1200°C without heat treatment.

4.2.2. Microstructure characteristics

The cross section macrographs of high-phosphorus weathering steels with similar characteristics are illustrated in Figure 4.3. The joints with no defects were produced for all steels under the welding conditions in this research. The weld nugget appears to have the typical basin-shape which is consistent with the geometry of the welding tool, and the weld zone is not perfectly symmetric to the weld centerline. The complete consolidation at the weld root can be observed for all welding conditions. A subtle difference of the weld section between all materials is that the SZ of Steel3 is slightly inclined to AS of the FSW processing, while those of Steel1 and Steel2 can be more symmetric by the AS and RS. The TMAZ of Steel3 corresponding to AS and RS of the FSW process is magnified as seen in Figure 4.4 together with the weld nugget. Clear borderlines can be observed between the SZ and the TMAZ, and the distinct feature is the streamline distribution against the borderline which indicates the ring vortex flow direction. The onion rings are obviously observed in the center of SZ with the band structures distributed above for Steel1 and Steel3, while they are not so clear for Steel2.

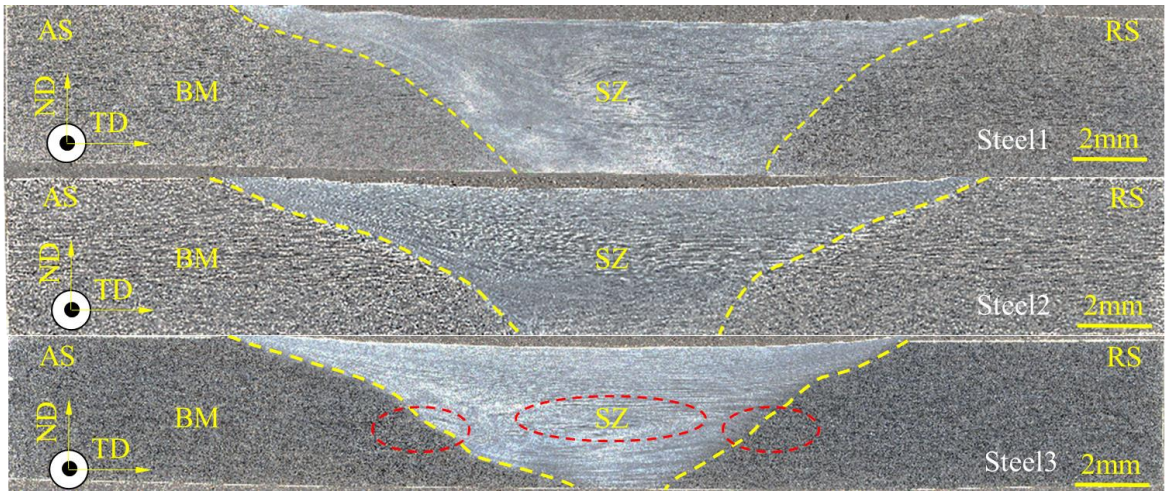

Figure 4.3 The cross section of Steel1, Steel2 and Steel3

The microstructures of the TMAZ-AS, band structure and TMAZ-RS of Steel3 are also shown in Figure 4.4. The grains at TMAZ-AS and TMAZ-RS are extremely elongated along the direction of the ring vortex flow. The cementite at TMAZ-AS illustrates a more obvious

dispersion than those at TMAZ-RS. This can be explained by the different flow behaviors of material on both sides resulting in the higher strain and temperature at TMAZ-AS [121]. As the probe rotation shares the same direction as the probe travelling along the steel plate, the plastic flow against the base metal on AS is severer than that on RS. This deformation behavior results in the larger strain gradient and plastic flow on AS, thus the ferrite is recrystallized and cementite is more severely dispersed and refined compared to those on RS. The band structure with only ferrite can be observed in the ferrite + cementite microstructure of the SZ. A possible explanation for the origin of this band structure given by Dmitriev [155] is that during the successive shear of thin layers when the shear stress from friction force exceeds the yield strength of the material, the sliding occurs between the base metal and welding tool, thus the material sticks to the tool and no sufficient heat input is available for the recrystallization.

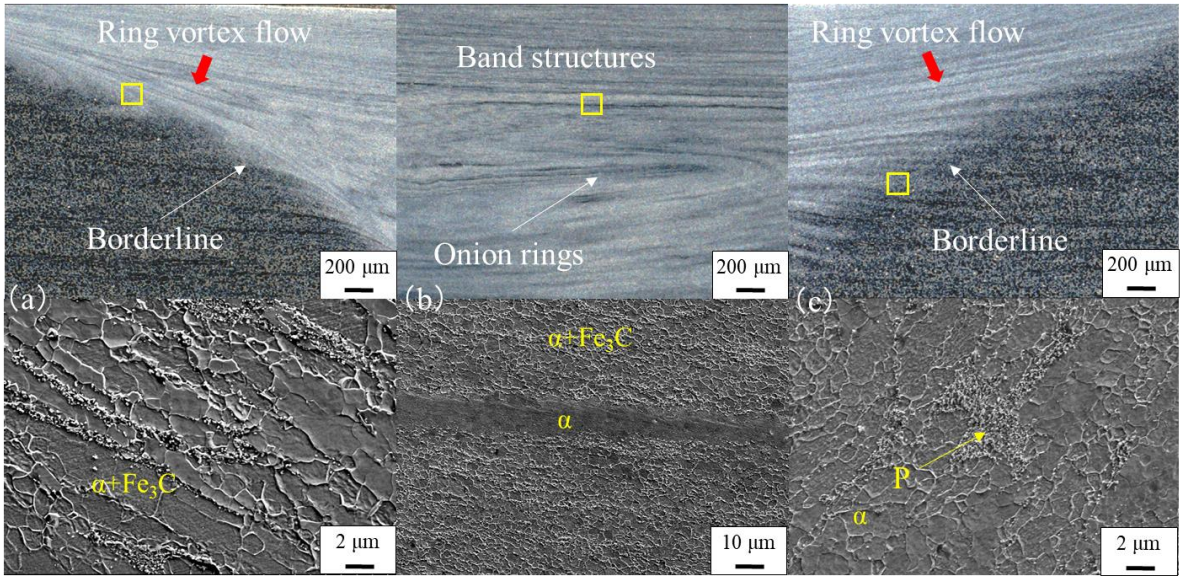

Figure 4.4 The macro and micro structure of Steel3 (a) TMAZ-AS; (b) band structure; (c) TMAZ-RS

The microstructures of the base metal are illustrated in Figure 4.5(a)-(c). The ferrite mixed up with the stratiform-shaped pearlite can be observed for all materials. The grain size d and pearlite contents η are shown in Figure 4.5(d). The grain sizes of SMA490AW and SPA-H are close to those of Steel1 and Steel2. Although the alloying element Nb was added to Steel3 to achieve the grain refinement, the grains of Steel3 are not fully refined as expected and

comparatively larger than other steels which were treated by normalization.

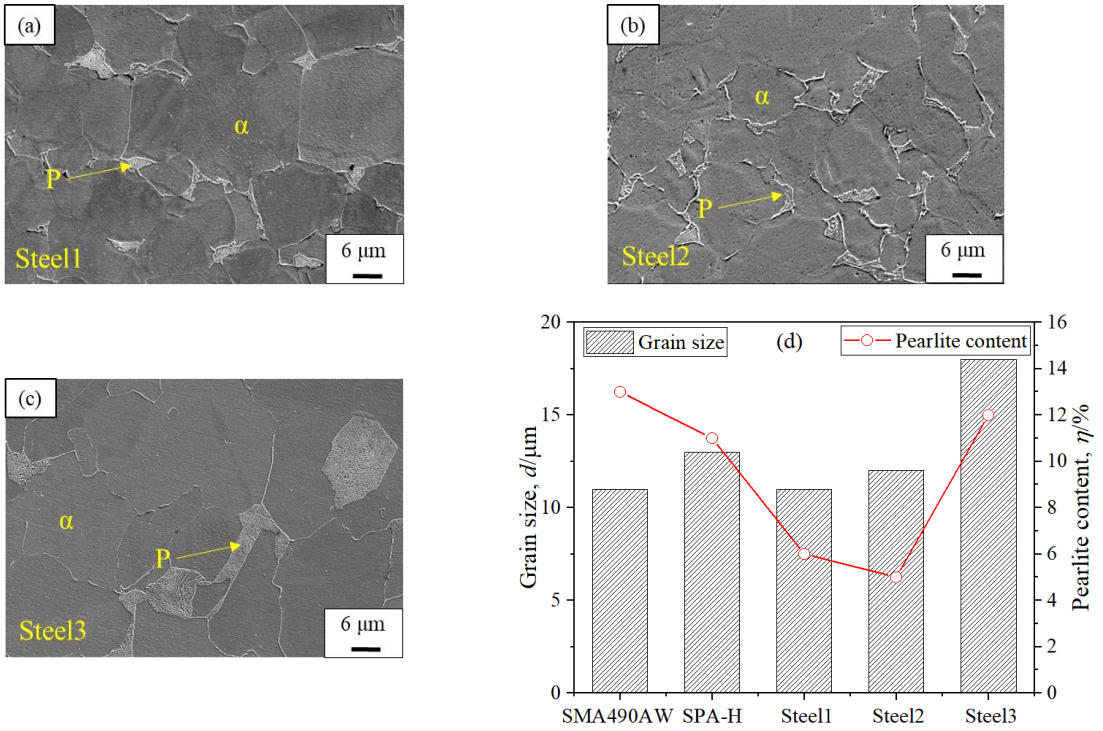

Figure 4.5 Microstructure of BM (a) Steel1; (b) Steel2; (c) Steel3; (d) Grain size d and Pearlite contents η

The pearlite of BM is magnified for all materials as seen in Figure 4.6. The pearlite of Steel1 and Steel2 is much coarser than that of the conventional weathering steel while an obvious refinement is achieved for Steel3 because of the addition of alloying elements, which also results in the increasing of pearlite contents as illustrated in Figure 4.5(d).

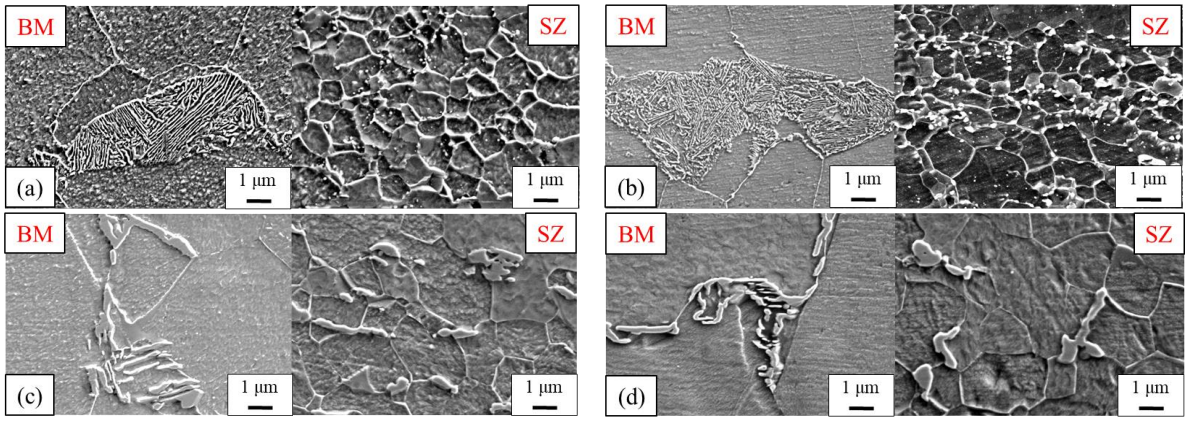

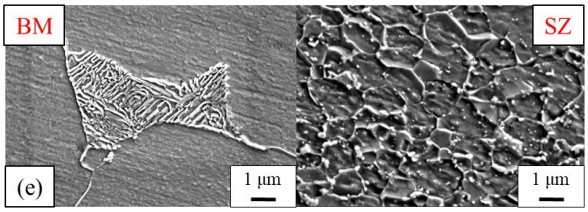

Figure 4.6 The microstructures of SZ corresponding to the microstructures of BM (a) SMA490AW; (b) SPA-H; (c) Steel1; (d) Steel2; (e) Steel3

The SZ is composed of ferrite and cementite with much finer ferrite grains compared to the BM due to DRX induced by frictional heat and severe plastic deformation. The cementite of Steel3 is more refined than those of Steel1 and Steel2 due to the refinement of the pearlite at BM. Moreover, in spite of the materials, the ferrite phase is mainly observed without any evidence of phase transformation at SZ, while the mixed recrystallized and recovered microstructures with highly misoriented and refined globular cementite can be observed at TMAZ. The TMAZ-AS microstructure presented in Figure 4.4 reveals the change in grain orientation due to the metal excavation from this zone to deposit at TMAZ-RS.

4.2.3. Microhardness distribution

Figure 4.7 shows the microhardness distribution of the conventional weathering steels and the high-phosphorus weathering steels joined by FSW. The microhardness of the SZ is generally higher than the BM due to the refined grains, though the microhardness profile is slightly different between the various materials. For the conventional weathering steels, the SMA490AW and SPA-H share similar microhardness at TMAS-AS while the area of high microhardness is larger for SPA-H than for SMA490AW at TMAS-RS. The microhardness of the base metal for these two steels is almost the same.

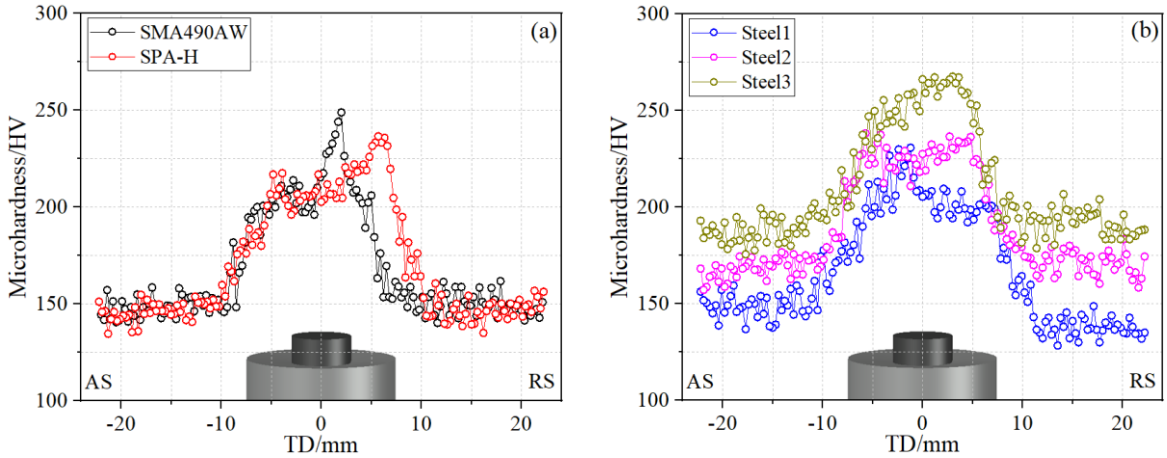

Figure 4.7 The microhardness of FSW joints (a) The conventional weathering steel; (b) The developed steels

For the high-phosphorus weathering steels, the increasing wt.% P results in the enhancement of microhardness at both the base metal and welded joint. By the addition of alloying elements, the microhardness of Steel3, especially for the SZ, is significantly increased compared to Steel1 and Steel2 due to the refinement of ferrite and the strengthening phase cementite. The solid solution of alloying elements into the ferrite is also believed to contribute to the increasing microhardness. No HAZ softening is observed for both conventional weathering steels and high-phosphorus steels, indicating a favorable weldability by FSW.

4.3. Ductile performance

4.3.1. Yield and fracture characteristics

The mechanical properties of FSW joints vertical to the welding direction were investigated. The tensile specimens were first milled by the polishing machine, and then polished by the sandpaper up to 1000 grits. The monotonic experiment was conducted on the base metal specimens and FSW joint specimens under the same testing conditions. Figure 4.8 illustrates the typical Load- Displacement curves and corresponding strain distribution of the FSW joints measured and analyzed by DIC system. The numbers attached on the figures indicate when the DIC was used for the strain measurement. The FSW specimens all

experienced twice yield stages occurring in the base metal region. Taking Steel1 which illustrates the most obvious twice yield features for example, the yield stress of the BM-AS (2) was first reached after the elastic loading (1). The visible front of the plastic deformation (Lüders band) can be observed at an angle about 50° from the specimen axis, which is more clear for Steel3. The plastic deformation of base metal was successively accumulated on AS, until the parallel part of BM-AS all entered the hardening stage (3). With the increasing load, the base metal on RS also reached the yield stress (4), and the hardening was continued and the plastic deformation was furtherly increased at both RS and AS (5). It can be observed that the load when the first yield occurred is almost the same as the second yield. At the fracture stage, part of the weldment also yielded and a certain plastic deformation was accumulated, while the core of the weldment was still in the elastic condition even when the specimen was fractured (6). The fracture happened on the same side as the first yield for all specimens.

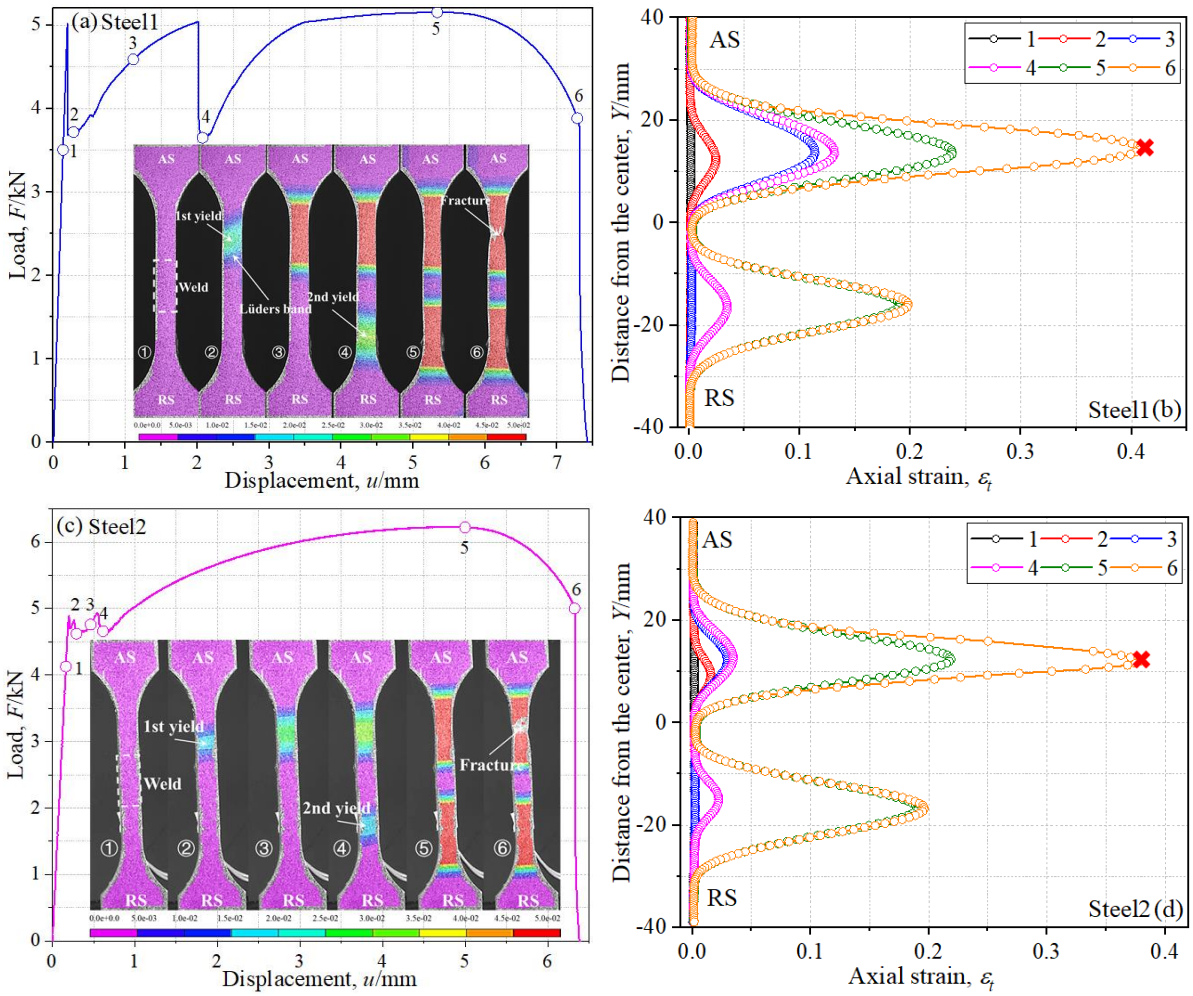

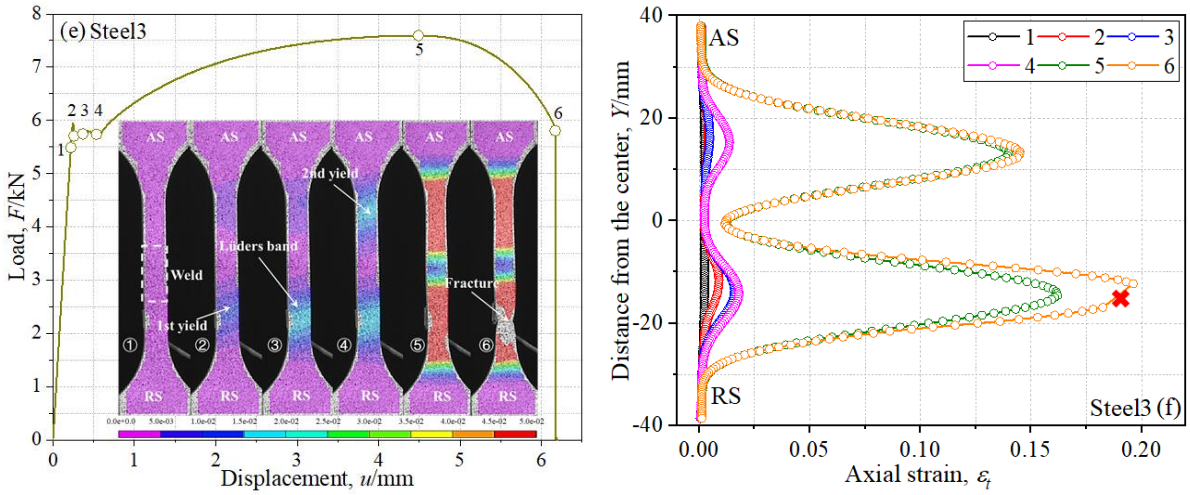

Figure 4.8 The yield and fracture condition of Steel1, Steel2 and Steel3 (a)(c)(e) represent the Load-Displacement curves and strain contours of the specimen; (b)(d)(f) represent the axial strain distribution as a function of distance from weld center along the TD direction

The two steps of yield occurring in the FSW specimen result from the high microhardness of the weld. The weld with the high microhardness and strength serves as an obstacle to prevent further development of plastic deformation in other regions of the specimen, thus the yield process of the FSW specimen is not consistent, but divided into two steps bordered by the strong weldment.

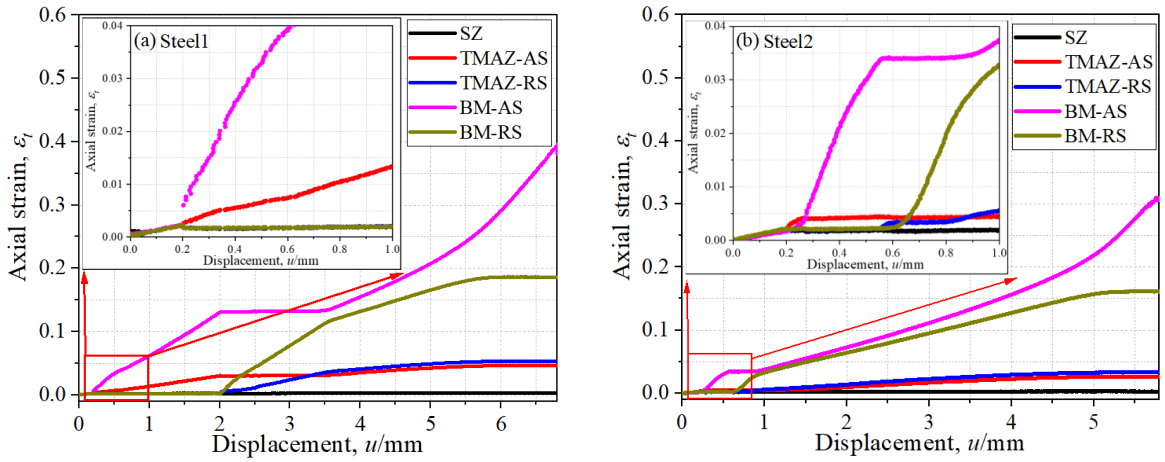

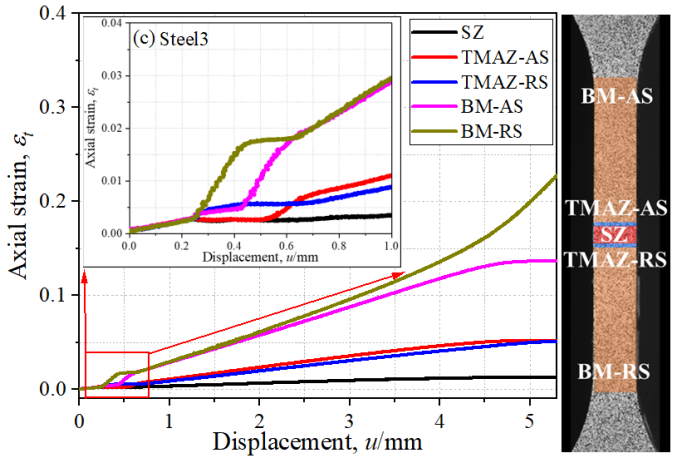

Figure 4.9 The axial strain accumulation of different zones (a) Steel1; (b) Steel2; (c) Steel3

The axial strain history of critical spots (SZ, TMAZ-AS, TMAZ-RS, BM-AS, BM-RS) and the appearance of the specimen before and after monotonic testing are illustrated in Figure 4.9. A typical characteristic for the strain history is that the yield or fracture at one part is usually accompanied by the barely no increment of strain at another part. Taking Steel3 as an example, all critical spots were elongated by the same strain increment during the elastic stage. The BM-RS was first yielded while other critical spots were maintained at a low strain rate. A plateau could be observed for the BM-RS as soon as the BM-AS also entered the yield stage because almost no loading increment occurred at this time due to the fact that the yield and the elongation were mostly contributed by the BM-AS. The yield of BM was usually followed by the obvious change in the strain at the TMAZ because the plastic deformation was propagated from the low-hardness region to the high-hardness region, i.e., from the BM to the SZ. At the fracture stage when the load stopped increasing, a plateau could be observed at all critical spots except for the BM-RS because of the large necking and the subsequent fracture.

4.3.2. Tensile properties

The nominal stress-nominal strain relationship of high-phosphorus weathering steels including the base metal and welded joints is illustrated in Figure 4.10. The results of conventional weathering steels are also referenced. The elongation of the FSW specimens is always smaller than that of the BM specimens because the welded joint with high

microhardness is barely deformed, and the deformation is mostly contributed by the base metal part of the specimen. Since there is no HAZ softening in the weld and the strength of SZ is higher than BM, the fracture strength of the specimen is dependent on the base metal part. Therefore, the fracture strength of the FSW specimens can be as high as the BM specimens, resulting in a joint efficiency of 100%.

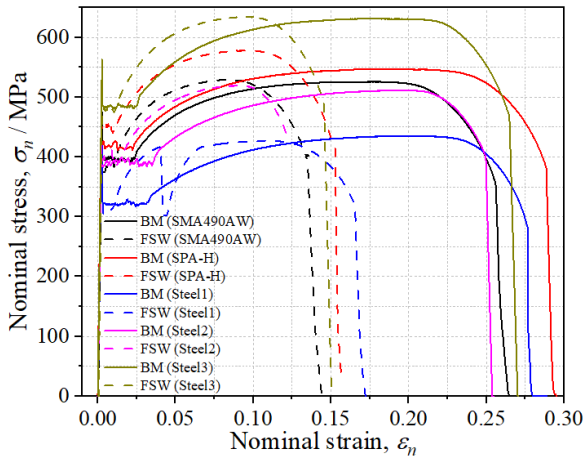

Figure 4.10 Nominal stress - nominal strain relationship

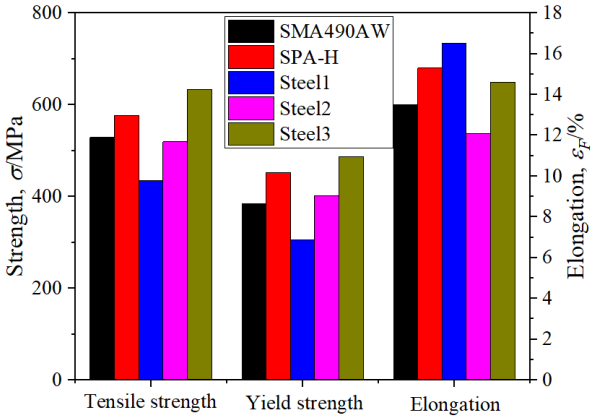

Figure 4.11 The mechanical properties of FSW joints

The tensile strength, yield strength and elongation of the FSW joints are summarized in Figure 4.11. The mechanical properties of the FSW joints are assessed by their strength and elongation. The high-phosphorus Steel3 has the highest yield strength and tensile strength among the studied steels, while Steel1 is featured by the largest elongation due to its favorable deformed behavior. The increasing wt.% P can result in the enhancement of the strength by comparison of Steel1 and Steel2. The solid solution of alloying elements into the ferrite contributes to enhancement of ductile behavior and ultimate strength at the same time by comparison of Steel2 and Steel3. Overall, Steel3 joined by FSW is characterized by the highest strength and favorable ductile behavior among the studied steels.

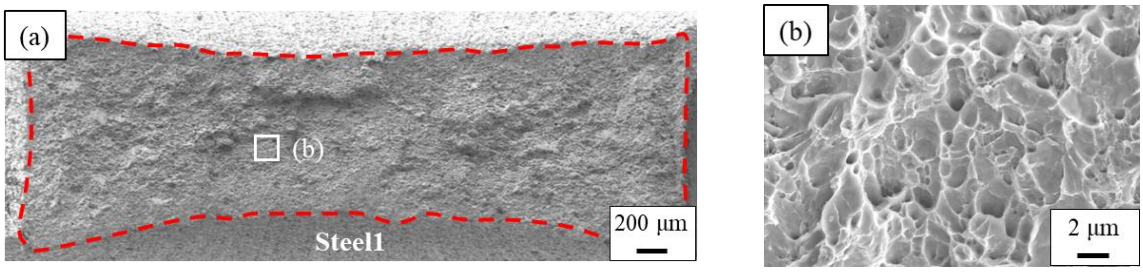

Figure 4.12 Fracture surface (a) overview of surface; (b) surface microstructure

All the fracture surfaces of the FSW specimens illustrate a ductile behavior because the fracture occurred at the base metal of the FSW specimen due to the high strength of the weld nugget. The fracture surface of Steel1 is illustrated in Figure 4.12 as an example, which is characterized by the presence of fine and coarse dimples as a typical ductile fractography.

4.4. Fatigue performance

4.4.1. Fatigue strength

The loading stress range $\Delta\sigma$ was initially determined based on the design curve of FAT112 proposed by IIW [151], and the specimens were loaded at a comparatively low stress level (below the yield stress). After several trials, it was found that the tested specimens could fracture before running out (2×10^6 cycles) only when the peak stress was larger than the upper yield stress σ_{YU}. Therefore, the remaining specimens were all carried out by a peak stress above the upper yield point. The data points of the stress range $\Delta\sigma$ to the fatigue fracture life N_f are shown in Figure 4.13. The S-N curves were fitted by the least square method and also considering the survival probability of 97.7% and 2.3%. The upper yield stress σ_{YU} and tensile strength σ_B of the FSW specimens were added in Figure 4.13 in the form of stress range considering the stress ratio of 0.1. The design curve of FAT112 is also illustrated for comparison. As seen in Figure 4.13 (a)-(c), the BM specimens and FSW specimens of the three steels show similar fatigue strength. As the HAZ softening and interior defects were inhibited owing to the welding conditions in this research, the weld nugget had a stronger fatigue strength and the BM region became the weakest part of the FSW specimen. Therefore, the fatigue life of the FSW

specimens was dependent on the strength of the BM region where the fatigue fracture usually occurred.

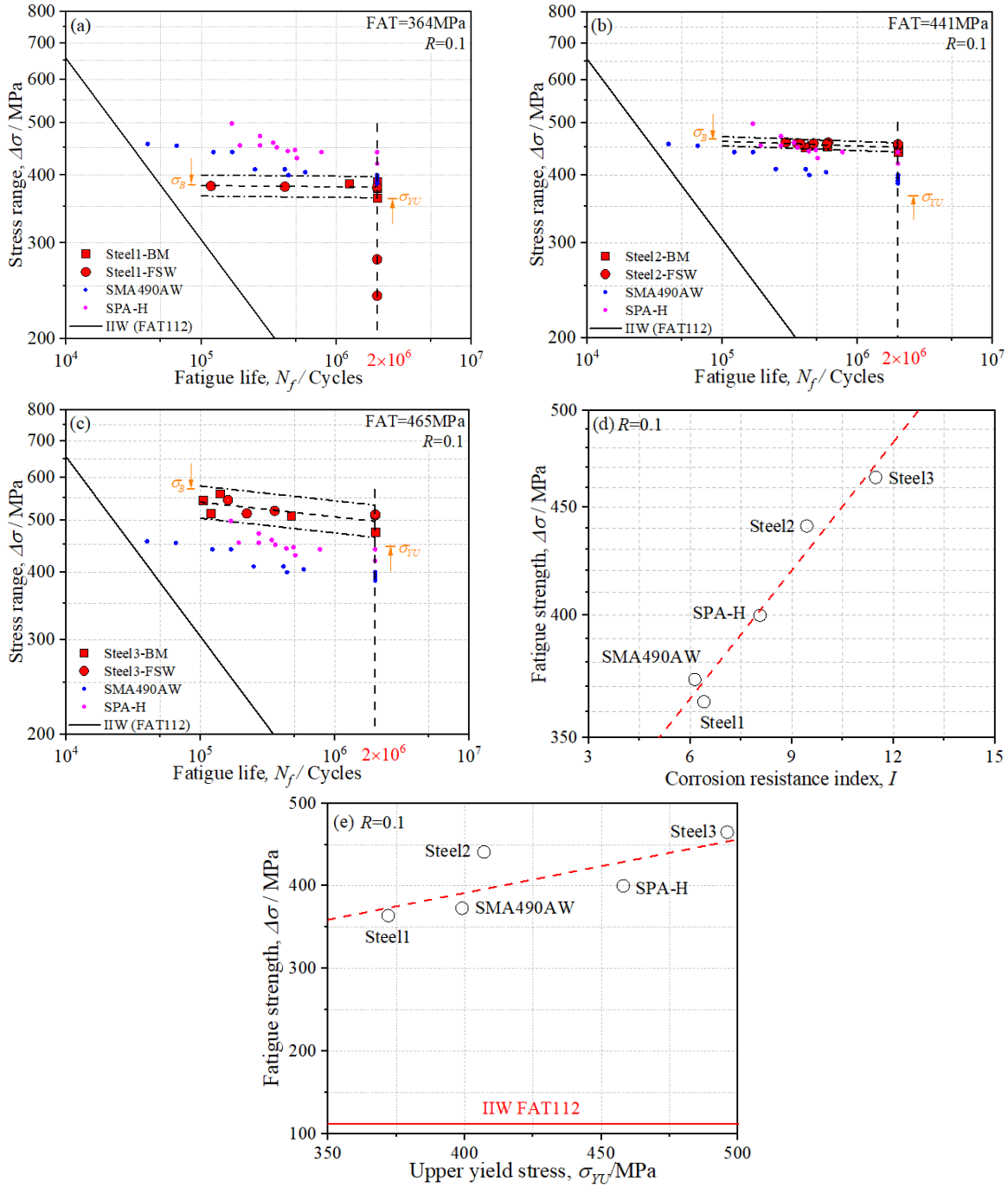

Figure 4.13 Assessment of fatigue life (a) Steel1; (b) Steel2; (c) Steel3; (d) relationship of fatigue strength $\Delta\sigma$ to corrosion resistance index I; (e) relationship of fatigue strength $\Delta\sigma$ to upper yield stress σ_{YU}

For Steel1 in Figure 4.13(a), most of the data points were running out and gathered at the

fatigue life of 2×10^6 cycles due to the low peak stress. The peak stress should often be larger than 98% of the tensile strength σ_B to make it fracture before running out. The slope of the fitted curves is extremely flat compared to the design curve due to the large yield ratio σ_{YU}/σ_B. The fatigue strength of Steel1 is generally lower than those of the conventional weathering steels, SMA490AW and SPA-H. The fitted S-N curve of Steel2 (Figure 4.13(b)) illustrates a larger slope compared to Steel1, but it is still much flatter than the design curve. The fatigue strength of Steel2 is lower than that of SPA-H in the low cycle fatigue region, while it is higher in the high cycle fatigue region. The fitted S-N curve of Steel3(Figure 4.13(c)) is more tilted than the other steels. The fatigue strength $\Delta\sigma$ is defined by the stress range corresponding to the fatigue fracture life $N_f = 2\times10^6$ cycles. As seen in Figure 4.13(d) which illustrates the relationship of the fatigue strength $\Delta\sigma$ to the corrosion resistance index I, Steel3 which is featured by the strongest anti-corrosion performance shows the highest fatigue strength among the three high-phosphorus weathering steels and conventional weathering steels SMA490AW and SPA-H. The linear relationship of the fatigue strength $\Delta\sigma$ to the corrosion resistance index I can be observed for the mild steels joined by FSW. The increasing wt.% P contributes to the enhancement of the anti-corrosion performance and fatigue strength by comparison of Steel1 and Steel2. The alloying elements such as the Ni, Cr and Nb result in a further improvement of anti-corrosion performance and fatigue strength by comparison of Steel2 and Steel3. Figure 4.13(e) compares the fatigue strength $\Delta\sigma$ of the three high-phosphorus weathering steels and conventional weathering steels to FAT112. The relationship of the fatigue strength $\Delta\sigma$ to upper yield stress σ_{YU} was fitted and the fatigue strength generally increases with the increasing upper yield stress. The fatigue strength of all steels is much higher than the FAT112 design curve, indicating that the steels joined by FSW below A_1 have a very favorable fatigue performance.

4.4.2. Ratcheting behaviors

The ratcheting behaviors of the FSW joints were assessed by the displacement variation of the fatigue specimens. The typical ratcheting behaviors are illustrated in Figure 4.14. For the specimens which were fractured before running out, two types of ratcheting behaviors can be observed. Type (1) in Figure 4.14(a) shows that the specimen maintained the elastic state when

the cyclic loading was initially applied. As the fatigue damage in the materials was accumulated, the yield suddenly occurred while it is speculated that only one part of the BM region was yielded at this stage. This is because when the plastic deformation was accumulated to some extent after the first yield, a sharp increase in the displacement was observed again which indicated the occurrence of the second yield. Based on the analyses in Section 4.3.1, two steps of yield usually happened for the FSW joints in this research and there was sometimes an interval between these two steps. Therefore, one part of the BM region was yielded at first, and after a certain accumulation of fatigue damage, the other part of the BM region was also yielded. After the second yield, the plastic deformation was drastically accumulated and the fracture quickly occurred. Type (2) in Figure 4.14(a) shows that a significant plastic deformation happened at the first cycle, and no obvious change in the plastic deformation could be observed until the final fracture suddenly happened. By comparison of Type (1) and Type (2), the large accumulation of plastic deformation could be observed in Type (1) after yielding, which resulted from the high stress level applied to the specimen. The specimens loaded by lower stress level usually illustrated the ratcheting behavior of Type (2).

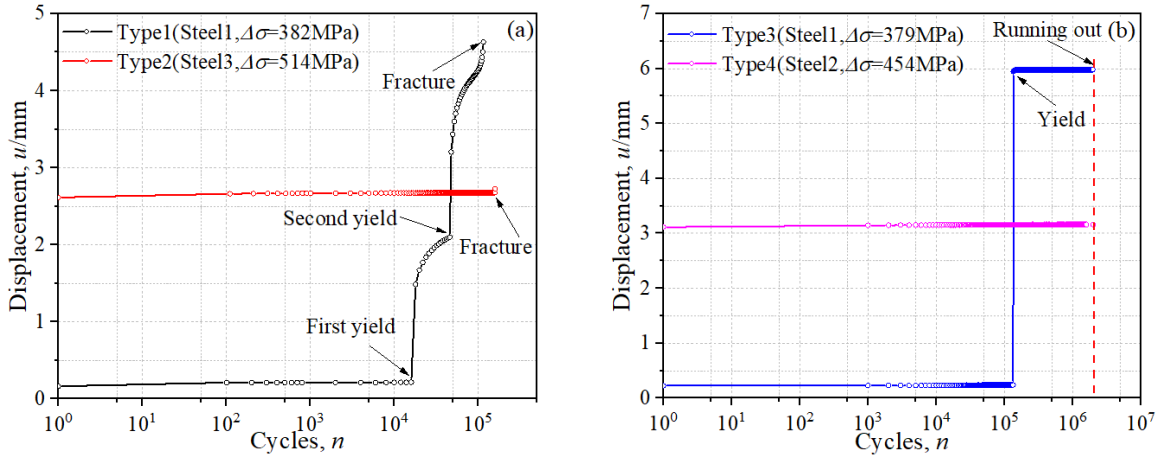

Figure 4.14 Typical ratcheting behaviors (a) Specimens which were fractured; (b) Specimens which were running out

Two other types of ratcheting behaviors can be observed for the specimens which were running out. Similar to Type (1), Type (3) illustrates that the specimen maintained the elastic state until the yield suddenly happened at high loading cycles. It is believed that the BM-AS and BM-RS yielded at the same time instead of one after the other. This is because the

displacement when the yield happened was rather high. If the displacement was contributed by only one side of the base metal, the large displacement could result in the direct fracture. Type (4) showed that the specimen yielded at the first cycle and did not fracture at $N = 2\times10^6$ cycles. The large plastic deformation occurred at the first cycle, and no obvious accumulation of ratcheting was observed even when the specimen was running out.

In Figure 4.14(a), the specimen of Type (1) illustrates a much smaller initial displacement than other types, but the fatigue life of this Type (1) is the shortest among the studied four types. This phenomenon results from the high yield ratio of FSW joints of Steel1. The yield ratio of FSW joints of Steel1 is as high as 94.1%, indicating that the upper yield stress is very close to the tensile strength. Although the specimen of Type (1) was loaded by a high stress level, the specimen could not yield due to the high upper yield stress, thus the initial displacement is very small. When the yield finally happened after dozens of cyclic slips, a large plastic deformation was accumulated due to the high stress level, resulting in the short fatigue life.

4.4.3. Influence of weld defects

During the optimization of the welding parameters, some welded samples with weld defects were obtained due to the inadequate downward load. In this research, weld defects were observed in Steel1 joined by a downward load of 42 kN and Steel3 joined by a downward load of 52 kN, and the welded joints with no flaws were obtained when the downward load was increased to 45 kN and 55 kN, respectively. The microstructure of the welded joints for Steel1 with weld defects which illustrates the typical hook shape is shown in Figure 4.15(a). The crack center with a triangular shape is magnified in Figure 4.15(b) and the white bands can be observed along the crack tip. As seen in Figure 4.15(c) and (d), the white bands were formed by a large amount of refined cementites along the propagation direction of the weld defects.

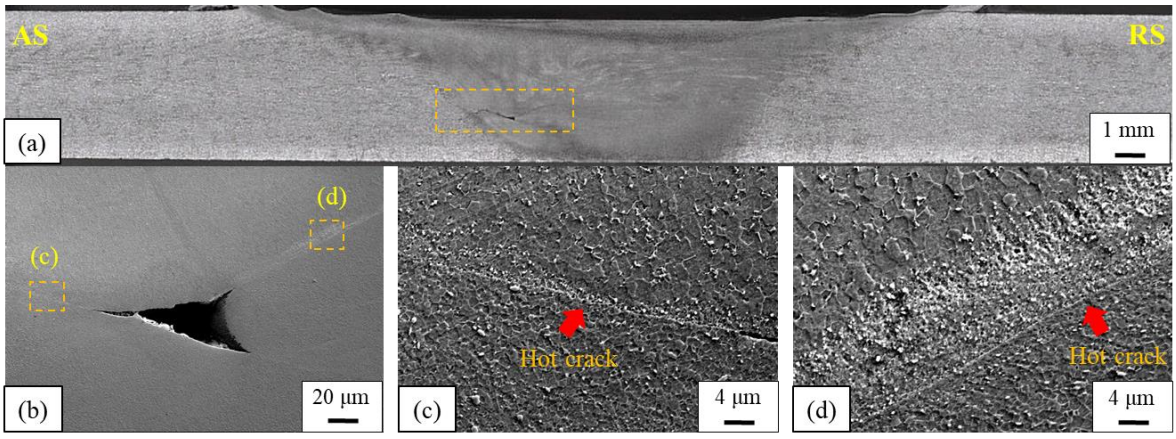

Figure 4.15 Weld defects of the welded joints (a) section of welded joints; (b) magnification of weld defects; (c) weld defects on the left; (d) weld defects on the right

The influence of weld defects on the tensile strength was discussed. The nominal stress-nominal strain relationship of specimens with and without flaws is shown in Figure 4.16. Some differences can be observed for the yield behavior, while the tensile strength was almost the same regardless of the weld defects. This is because the ductile fracture occurred in the BM region of the specimen instead of the weld nugget with weld defects, thus the tensile strength was dependent on the base metal. It can be summarized that the weld defects have no significant influence on the tensile strength of the FSW joints.

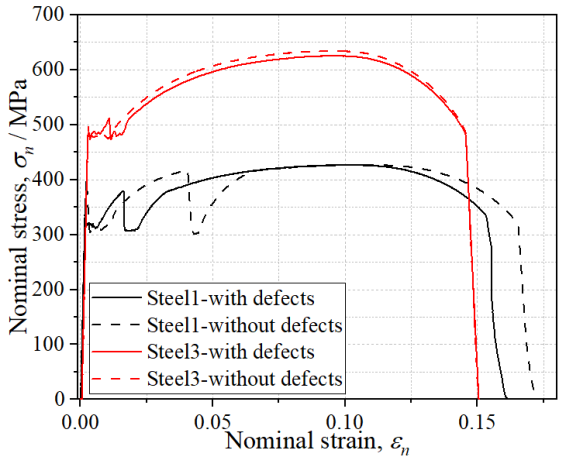

Figure 4.16 Nominal stress - nominal strain relationship of FSW joints with and without weld defects

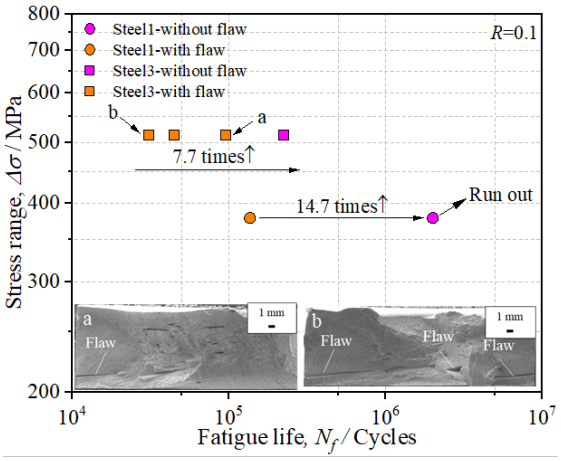

Figure 4.17 Fatigue experiment of FSW joints with and without weld defects

The fatigue experiment was carried out on four specimens with weld defects under the same stress range as the specimens without weld defects. As seen in Figure 4.17, the fatigue

life of the FSW specimen of Steel1 without flaws was increased by more than 14.7 times compared to that with weld defects. For the three specimens of Steel3 with flaws, the fatigue life was much shorter than that without flaws. Moreover, the weld defect length also had a great influence on the fatigue life. The specimen (b) in Figure 4.17 which had through-section flaws illustrated the shortest fatigue life.

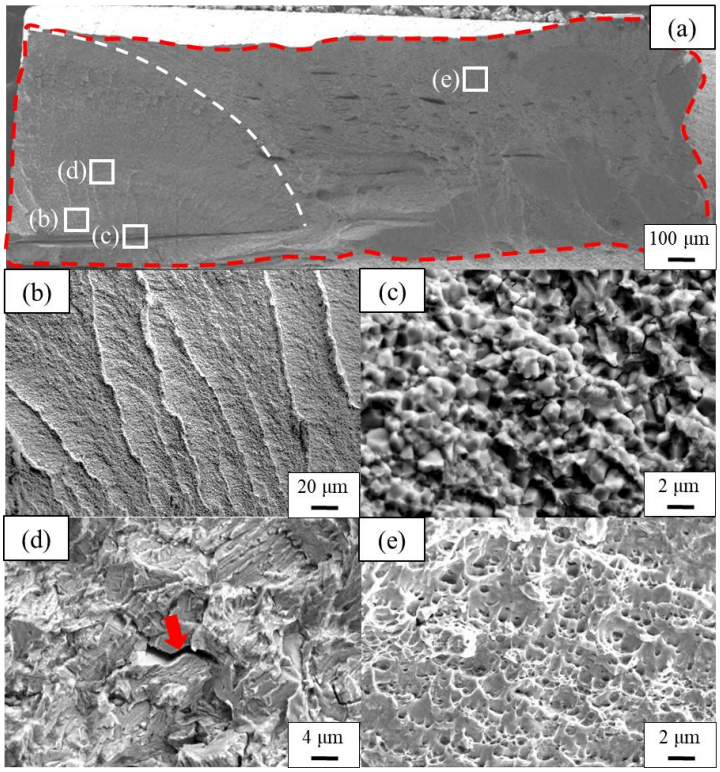

Figure 4.18 Fractography of the FSW specimen with weld defects (Steel3, $\Delta\sigma = 462.6$ MPa, $N_f = 44479$)

A distinct difference of fatigue fracture between the specimens with and without weld defects is that the specimens without weld defects all fractured from the BM region of the specimen, while those with weld defects fractured from the weld nugget. It is obvious that the weld defects result in the quick crack propagation under the fatigue loading. The fracture surface of one FSW specimen (Steel3, $\Delta\sigma = 462.6$ MPa, $N_f = 44479$) with weld defects is shown in Figure 4.18(a). The fracture surface can be divided into the crack propagation region and ductile fracture region. The crack propagation region is featured by a quarter of the ellipse shape with crack propagating radially from the weld defect. Very clear river marks can be

observed in Figure 4.18(b). Figure 4.18(c) is the fracture surface near the weld defect which is featured by the very small intergranular fracture corresponding to the cementites crystallized along the weld defect as seen in Figure 4.18(c) and (d). Figure 4.18(d) illustrates the typical cleavage fracture with clear striations, and the secondary crack could also be observed. The ductile fracture region is featured by very small dimples which indicated the large plastic deformation as seen in Figure 4.18(e).

4.5. Conclusions

In this chapter, high-phosphorus weathering steels with high wt.% P were friction stir welded below the A_1 temperature. The microstructure characteristics and mechanical properties of the weldments were investigated. The fatigue strength was also evaluated considering the anti-corrosion index and the yield stress. The plasticity accumulation of different regions and ratcheting behaviors was analyzed. The influence of the weld defects on the fatigue life was also clarified. The specific conclusions are as follows:

(1) The BM of all new weathering steels is characterized by ferrite and pearlite. The pearlite is refined and increased with the addition of alloying elements (Ni, Cr and Nb). The fine-grained ferrite and cementite can be observed at SZ, and the cementite of Steel3 is furtherly refined due to the refinement of pearlite at BM.

(2) The grains at TMAZ on the AS and RS are extremely elongated along the direction of the ring vortex flow. The cementite at TMAZ on the AS illustrates a more obvious dispersion than those on the RS due to the comparatively larger strain gradient and plastic flow.

(3) The increasing wt.% P improves the microhardness and strength of the friction stir welded joints but weakens the ductile behavior. The solid solution of alloying elements (Ni, Cr and Nb) into the ferrite can enhance the ductile behavior and mechanical strength at the same time.

(4) The friction stir welding applied in this research can achieve a joint efficiency of 100% for three high-phosphorus weathering steels with high wt.% P. The ductile fracture

characterized by fine and coarse dimples occurred at the base metal of the friction stir welded specimens due to the high strength of the weld nugget and absence of HAZ softening.

(5) The fatigue strength of the FSW specimens and BM specimens was almost the same for three high-phosphorus weathering steels. This was because the HAZ softening and interior defects were successfully inhibited owing to the FSW joining, thus the weld nugget had a stronger fatigue strength and the fatigue life was dependent on the BM region of the FSW specimens.

(6) The fatigue strength of three high-phosphorus weathering steels was much higher than the FAT112 design curve, and the *S*-*N* curves were extremely flat. The increasing wt.% P contributed to the enhancement of the anti-corrosion performance and fatigue strength. The alloying elements such as the Ni, Cr and Nb resulted in a further improvement of anti-corrosion performance and fatigue strength.

(7) In the fatigue test, the yield initially occurred in the BM region of FSW specimens then subsequently propagated to the HAZ in the first loading cycle. The SZ showed barely no plastic deformation in the first 10 cycles due to the high microhardness. The high stress resulted in the continuous accumulation of plastic deformation during the fatigue loading, while no obvious increase in the displacement could be observed for the specimen under the low stress.

(8) The weld defects due to the inadequate downward load resulted in the fatigue fracture at the weld nugget and decreased the fatigue life by as long as 14.7 times, but they barely had no influence on the tensile strength. The fracture surface near the weld defect was featured by the very small intergranular fracture corresponding to the cementite crystallized along the weld defect.

Chapter 5.

Conventional weathering steels joined by linear friction welding

5.1. Introduction

The conventional and high-phosphorus weathering steels were successfully joined by FSW below A_1 temperature, and the welding parameters have been optimized to ensure no solidification cracks (see Chapter 4). Compared to the FSW, the LFW can also join steels at low temperature but requires no shielding gas and consumes no welding tool, making it a promising way to join the engineering structures and components. In this chapter, the conventional weathering steels SMA490AW and SPA-H were joined by LFW. It is still difficult to achieve a welding temperature as low as A_1 for the weathering steels with high wt.% P by LFW, thus the welding was conducted at a temperature above A_3. The residual stress and geometry characteristics were measured, and the stress concentration factor (SCF) considering various flash shapes of LFW joins was assessed by FEM. The microstructure of LFW joints was analyzed corresponding to the microhardness distribution. The welded joints in the real engineering often work in a status of as-weld without polishing, thus it is necessary to investigate the mechanical properties of as-welded LFW joints. The yield and fracture characteristics of as-welded and polished LFW specimens under the monotonic loading were compared with the aid of DIC. The fatigue strength and crack propagation characteristics of as-welded and polished LFW specimens under the cyclic loading were also studied. Finally, the fractography of LFW specimens with different geometry characteristics was analyzed.

5.2. Residual stress, geometry characteristics, microstructure and microhardness

5.2.1. Residual stress distribution

The geometry and residual stress measured along the centerline of LFW joints with thickness of 12 mm are shown in Figure 5.1. The definition of coordinates in Figure 5.1 is consistent to that in Figure 2.3. To differentiate, the stationary side and oscillation side during the LFW joining process are pointed out in Figure 5.1. The residual stress in the X and Y directions is represented by $\sigma_{R\text{-}X}$ and $\sigma_{R\text{-}Y}$, respectively. There is no obvious difference in the residual stress distribution between both sides of the welded joint. The distribution of the residual stress along the oscillation direction ($\sigma_{R\text{-}X}$) illustrates a "W" shape and that along the loading direction ($\sigma_{R\text{-}Y}$) illustrates an "M" shape. Overall, $\sigma_{R\text{-}X}$ shows a high residual tensile stress on the weld toe, while a sharp decrease to the compressive stress is observed at a very short distance from the weld toe. With the further increasing distance from the weld toe, the residual stress is gradually increased and has the trend to converge. $\sigma_{R\text{-}Y}$ shows a completely opposite distribution with the high residual compressive stress on the weld toe followed by a sharp increase to the tensile stress. With the further increasing distance from the weld toe, the residual stress is gradually decreased and has the trend to converge.

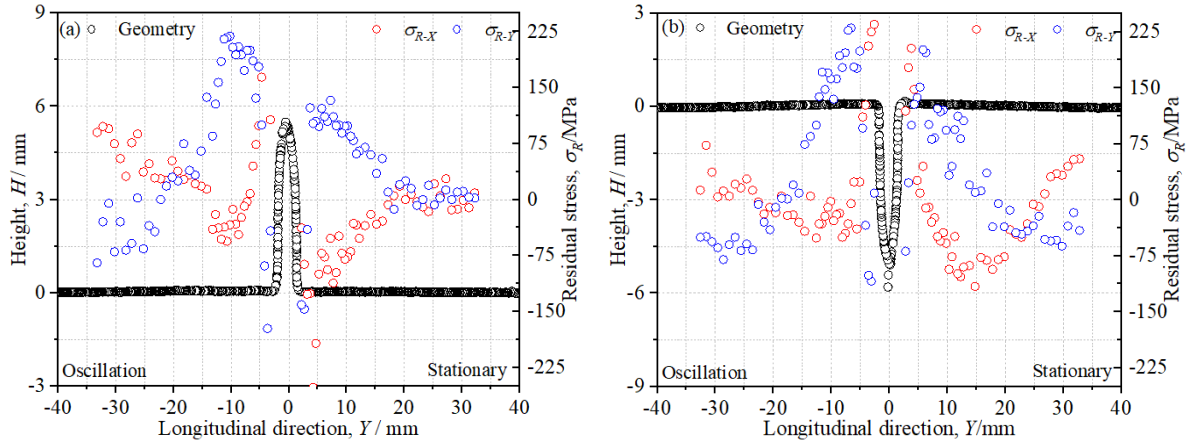

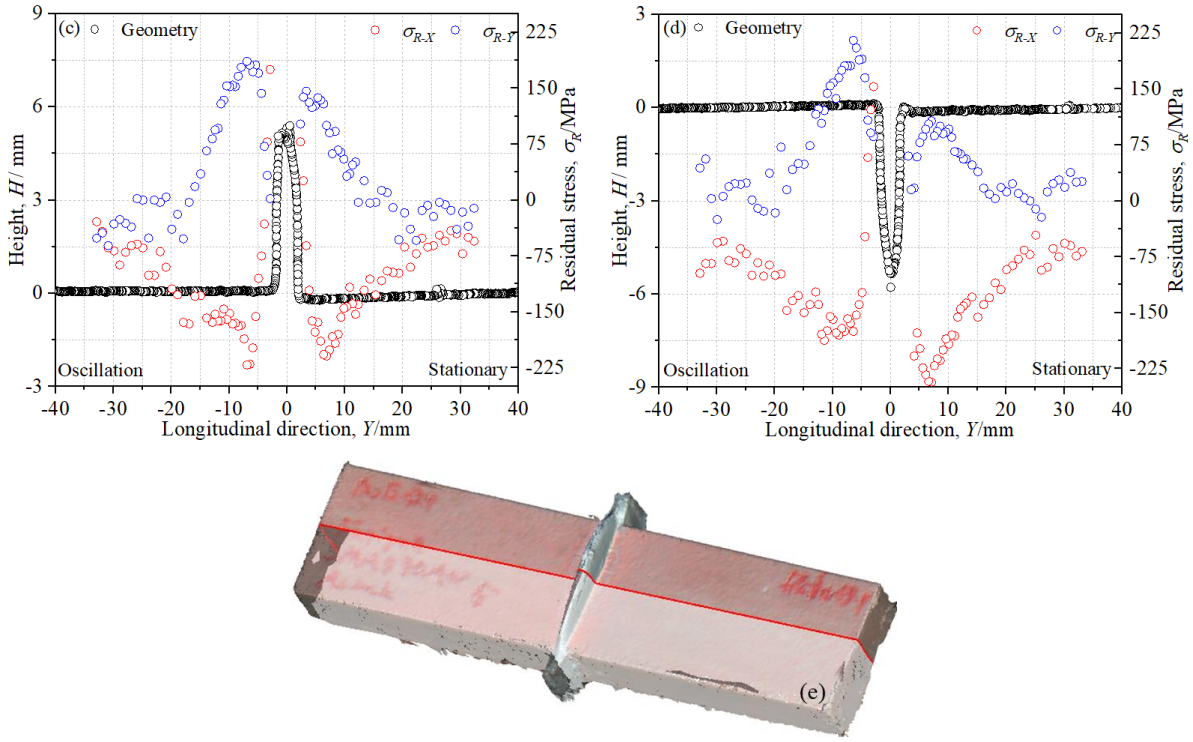

Figure 5.1 Geometry and residual stress of LFW joints (a) front side of SMA490AW; (b) back side of SMA490AW; (c) front side of SPA-H; (d) back side of SPA-H; (e) geometry measurement

The W-shaped distribution of $\sigma_{R\text{-}X}$ and M-shaped distribution of $\sigma_{R\text{-}Y}$ are influenced by whether the applied pressure loading can have the dominant influence on the residual stress. For $\sigma_{R\text{-}Y}$, the longitudinal residual tensile stress in the vicinity of the weld toe was inhibited because the applied pressure loading could provide the driving force for the longitudinal shrinkage of the softened materials, thus $\sigma_{R\text{-}Y}$ near the weld toe could be close to zero and even compressive stress. However, with the increasing distance from the weld toe, the welding temperature was not high enough to cause softening of the material. Therefore, the applied pressure loading failed to drive the shrinkage of the materials, and the shrinkage was driven by the internal stress between the materials and resulted in the residual tensile stress. The base metals far from the weld toe were only influenced by the low temperature increment due to the heat conduction, and the residual stress was rather small. For $\sigma_{R\text{-}X}$, the applied pressure loading was perpendicular and had little influence on the shrinkage along the oscillation direction. Therefore, the high residual tensile stress was observed and contributed by the internal stress due to the shrinkage of the materials near the weld toe. The compressive residual stress

occurred with a small distance increasing from the weld toe to achieve the internal stress balance. Similar to the trend of $\sigma_{R\text{-}Y}$, the residual stresss $\sigma_{R\text{-}X}$ of the base metals far from the weld toe was very small.

Table 5.1 Welding conditions of LFW from the reference [106] and this research

	Material	Frequency/Hz	Amplitude/mm	Pressure/MPa	Thickness/mm
Case1	S45C	20	1.5	100	2.0
Case2	S45C	20	1.5	200	2.0
Case3	S45C	20	1.5	300	2.0
Case4	S45C	20	1.5	400	2.0
Case5	SPA-H	50	1.5	50	12.0
Case6	SPA-H	50	1.5	50	3.2

The residual stress distribution of LFW joints by different welding conditions, materials and plate thickness from the reference [106] is compared. The welding conditions and materials are shown in Table 5.1. Case 1-4 is from the reference and Case 5-6 was conducted in this research. Figure 5.2(a) and (b) illustrate the residual stress distribution $\sigma_{R\text{-}X}$ and $\sigma_{R\text{-}Y}$ obtained on the stationary side of the LFW joints. Overall, $\sigma_{R\text{-}X}$ shows a peak value of the residual tensile stress at the weld toe, while the tensile stress is sharply decreased to the compressive stress at a very small distance from the weld toe. At a further increasing distance from the weld toe, $\sigma_{R\text{-}X}$ gradually increases and converges in the state of a small tensile stress. The distribution of residual stress $\sigma_{R\text{-}Y}$ is slightly different from that of $\sigma_{R\text{-}X}$, as the peak value of the residual tensile stress is induced at about 2-4 mm from the weld toe. $\sigma_{R\text{-}Y}$ shows a higher peak value of residual tensile stress than $\sigma_{R\text{-}X}$, and then gradually decreases to the compressive stress at the increasing distance from the weld toe. $\sigma_{R\text{-}Y}$ finally converges in the state of a small compressive stress. The similar distribution of residual stress $\sigma_{R\text{-}X}$ and $\sigma_{R\text{-}Y}$ can be observed for LFW joints by different welding conditions, materials and plate thickness, thus the residual stress distribution elaborated in this research can be general characteristics for LFWed steels.

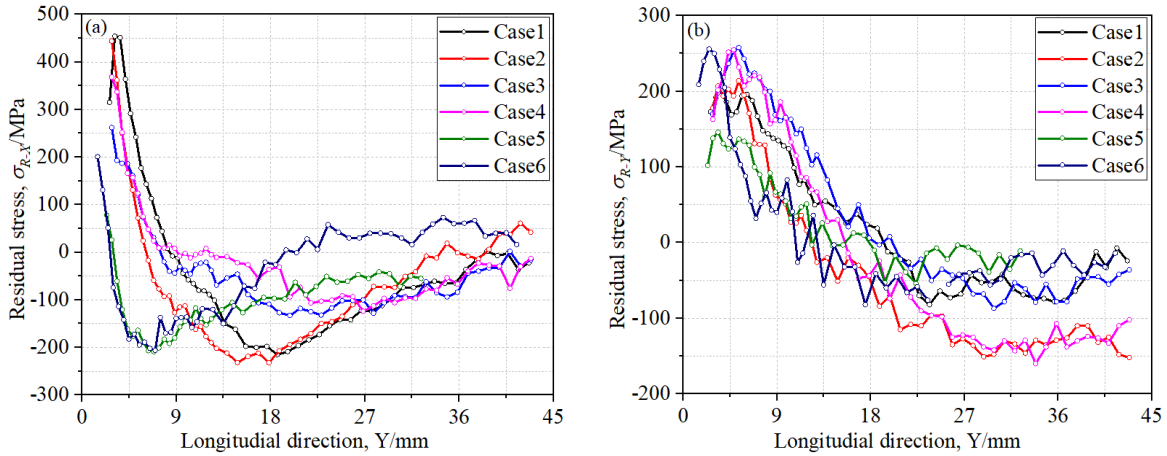

Figure 5.2 Comparison of residual stress distribution from previous references (a) residual stress $\sigma_{R\text{-}X}$; (b) residual stress $\sigma_{R\text{-}Y}$

5.2.2. Assessment of stress concentration

The angular distortion α and eccentric misalignment δ were measured on the centerline of 7 LFW joints with thickness of 3 mm and 6 LFW joints with thickness of 12 mm. under the same welding conditions. The α and δ were defined as illustrated in Figure 2.4(b), and the results are shown in Table 5.2. The angular distortion of the LFW joints in this research ranged from 0.02° to 0.26°. A higher discreteness of eccentric misalignment can be observed for the eccentric misalignment, which is 0.012 mm-0.328 mm.

Table 5.2 Geometry parameters

SPA-H	Angular distortion (α)	Eccentric misalignment (δ)	Slice	Weld toe radius (ρ)	SCF(K_t)
Plate thickness t = 3 mm					
Joint1	0.03°	0.115 mm	Slice1	0.133 mm	2.46
Joint2	0.02°	0.087 mm	Slice2	0.241 mm	2.28
Joint3	0.20°	0.183 mm	Slice3	0.122 mm	2.83
Joint4	0.05°	0.208 mm	Slice4	0.154 mm	2.46
Joint5	0.04°	0.060 mm	Slice5	0.149 mm	2.37
Joint6	0.07°	0.051 mm	Slice6	0.369 mm	2.58(1.68)

Joint7	0.01°	0.012 mm			
Plate thickness t = 12 mm					
Joint1	0.26°	0.328 mm	Slice1	0.325 mm	3.27
Joint2	0.21°	0.139 mm	Slice2	0.176 mm	2.78
Joint3	0.26°	0.275 mm	Slice3	0.221 mm	2.54
Joint4	0.05°	0.156 mm	Slice4	0.336 mm	2.60
Joint5	0.03°	0.171 mm	Slice5	0.301 mm	2.19
Joint6	0.02°	0.118 mm	Slice6	0.611 mm	2.87

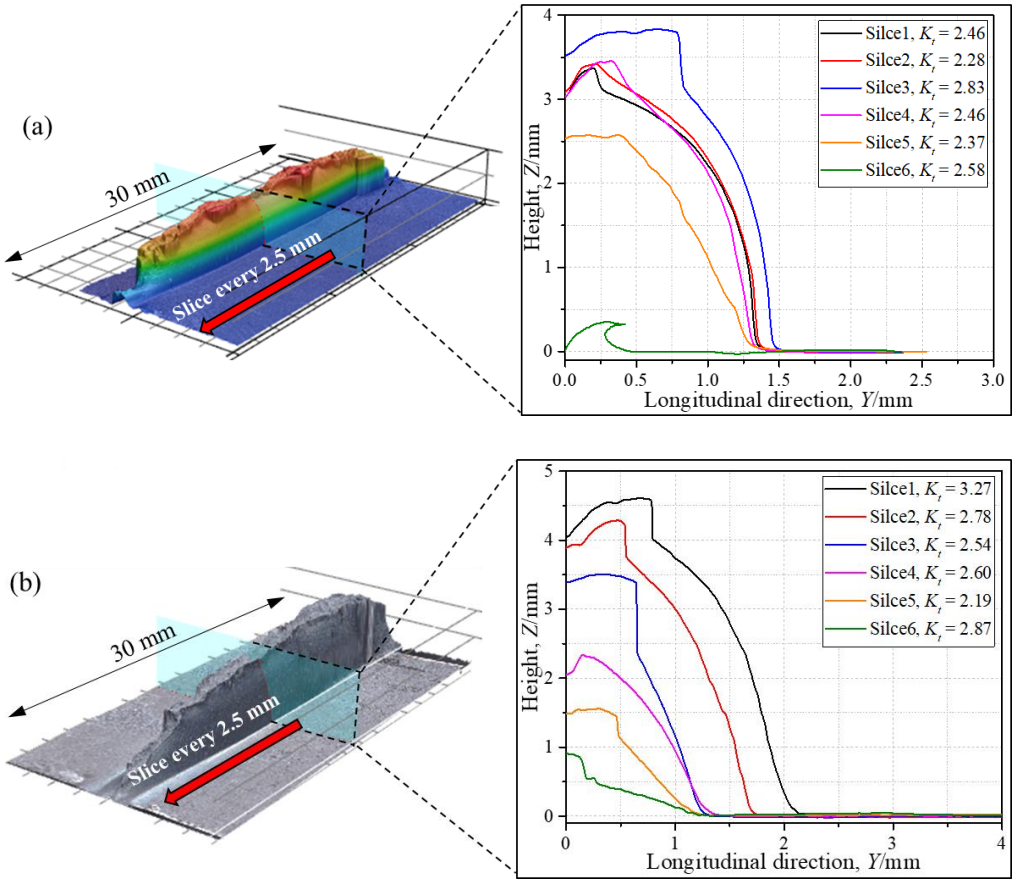

Figure 5.3 Geometry characteristics of LFW joints (a) thickness of 3 mm; (b) thickness of 12 mm

The flash profile of Joint5 with t = 3 mm and Joint6 with t = 12 mm was measured to assess the stress concentration factor (K_t) of the LFW joints. Considering the variation of flash profiles, six slices perpendicular to the oscillation direction were conducted at an interval of 2.5 mm as seen in Figure 5.3, and used as the geometry data for the FEM models. It is observed

that the flash usually shows a “mountain” shape with a high weld reinforcement, while that near the edge of the joint is much smaller and characterized by a “wave” shape. The weld toe radius ρ, which ranged from 0.122 mm to 0.369 mm, was measured and shown in Table 5.2.

The one-quarter FEM models for six slices were built considering a plane stress condition by the commercial software ABAQUS v6.14-3. The material was assumed to be isotropic with an elastic modulus E = 206 GPa and a Poisson’s ratio v = 0.3. The plane stress element CPS4 was used with a global grid size of 0.5 mm and local grid size of 0.01 mm for the flash. The FEM model and boundary conditions are illustrated in Figure 5.4(a). The influence of angular distortion and eccentric misalignment was not considered in the FEM models.

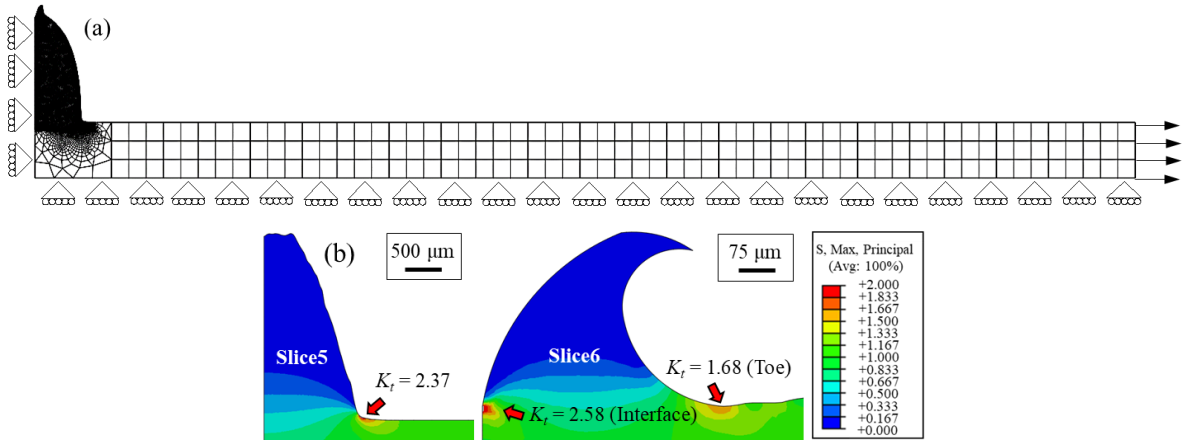

Figure 5.4 Stress concentration factor assessment (a) FE model and boundary conditions; (b) maximum principal stress contour of Slice5 and Slice6 for LFW joints with thickness of 3 mm

The severe stress concentration of the LFW joints is usually located at the weld toe, which is the potential position of fatigue crack initiation. The maximum principal stress contour of Slice5 is shown in Figure 5.4(b) as an example. The stress concentration factors represented by K_t were calculated for six slices and shown in Table 5.2 and Figure 5.4(a). The stress concentration factors ranged from 2.28 to 2.83 for Slice1 to Slice5, the values of which are mostly influenced by the weld toe geometry. It is worth noting that at the edge of the LFW joints, the most severe stress concentration can possibly locate at the weld interface instead of the weld toe. As seen for Slice6 in Figure 5.4(c), the weld interface has a much higher stress

concentration factor (K_t = 2.58) than the weld toe (K_t = 1.68). In this case, the weld interface is also the potential source for the fatigue crack initiation.

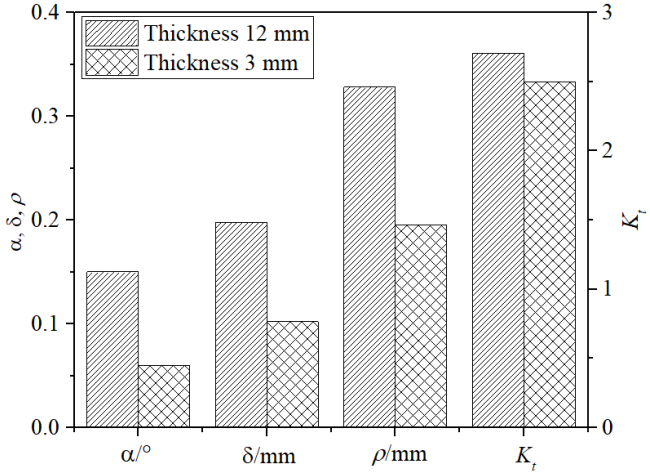

Figure 5.5 Comparison of geometry characteristics between LFW joints with thickness of 12 mm and 3 mm

The average values of angular distortion (α), eccentric misalignment (δ), weld toe radius (ρ), stress concentration factor (K_t) were calculated. The comparison of geometry characteristics is illustrated in Figure 5.5. It can be observed that the average values of angular distortion and eccentric misalignment of the thick LFW joints are larger than that of the thin LFW joints. Although the weld toe radius of the thick LFW joints is larger than that of the thin LFW joints, the stress concentration factor of the thick LFW joints is comparatively higher.

5.2.3. Characteristics of microstructure and microhardness

The microhardness contour of the LFW joined SMA490AW and SPA-H is summarized in Figure 5.6(a) and (c). It can be observed that the boundary of the high microhardness region coincides with that of the WCZ and the HAZ. With the decreasing distance from the flash, the area of WCZ and HAZ is increased, as is the high microhardness region. This can be explained by the higher freedom of plastic flow of materials at the edge of the workpieces which results in the larger friction heats. Also, the microhardness contour illustrates a generally higher microhardness of SMA490AW than that of SPA-H. The linear microhardness distributions of

SMA490AW and SPA-H at Z = 0 mm, Z = 3 mm and Z = 6 mm are shown in Figure 5.6(b) and (d). The linear microhardness distribution at Z = 6 mm shows the larger area of the high microhardness region than that at Z = 0 mm and Z = 3 mm.

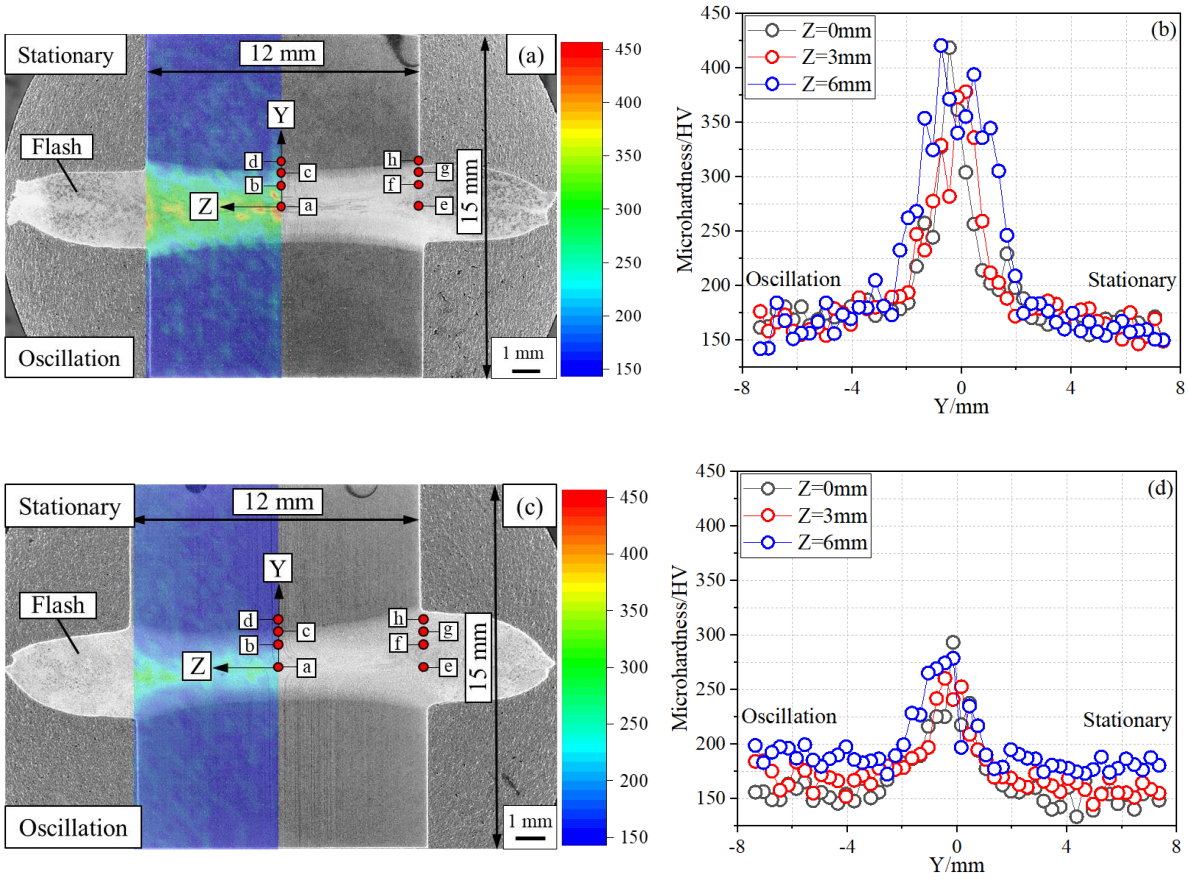

Figure 5.6 The microhardness of LFW joints (a) microhardness contour of SMA490AW (unit: HV); (b) linear microhardness distribution of SMA490AW; (c) microhardness contour of SPA-H (unit: HV); (d) linear microhardness distribution of SPA-H

The microstructure of welded joints of SMA490AW on various positions is illustrated in Figure 5.7. Figure 5.7(a)-(d) correspond to the positions of Z = 0 mm and Y = 0 mm, 1 mm, 1.5 mm and 2 mm in the center of the weld as seen in Figure 5.6. Figure 5.7(e)-(h) correspond to the positions of Z = -6 mm and Y = 0 mm, 1 mm, 1.5 mm and 2 mm near the flash. It is observed that the microhardness distribution conforms to the variation of the area fraction of bainites. As seen in Figure 5.7(a)-(d), the weld center (Figure 5.7(a)) shows a large area fraction of bainites accompanied with a small amount of ferrites, resulting in a high microhardness as

seen in Figure 5.6(b). At the distance of 1 mm from the weld center (Figure 5.7(b)), the bainites are obviously decreased while the area fraction of ferrites is increased. These phenomena suggest that the weld center has the highest welding temperature, and even a small distance from the weld center results in the drastic temperature decrease, indicating a large temperature gradient from the WCZ to the BM. At a distance of 1.5 mm from the weld center (Figure 5.7(c)), the bainites are furtherly decreased and nearly disappear, and the ferrites occupy most of the area with a small amount of recrystallized cementites, which result from the plastic deformation at a low temperature. The disappearance of bainites result in the sharp decrease of microhardness as seen in Figure 5.6(b). At a distance of 2 mm from the weld center (Figure 5.7(d)), the BM microstructure with coarse ferrites and pearlites are observed, indicating that the width of the weld in the center of the sample is approximately 3 mm. The decrease of microhardness tends to converge from this position. As seen in Figure 5.7(e)-(h), the trend of the microstructural evolution from the weld center to the BM at Z = -6 mm (near the flash) is similar to that at Z = 0 mm. However, a certain amount of bainites can still be observed even at a distance of 2 mm from the weld center, which results in the larger area of high microhardness region as seen in Figure 5.6(b).

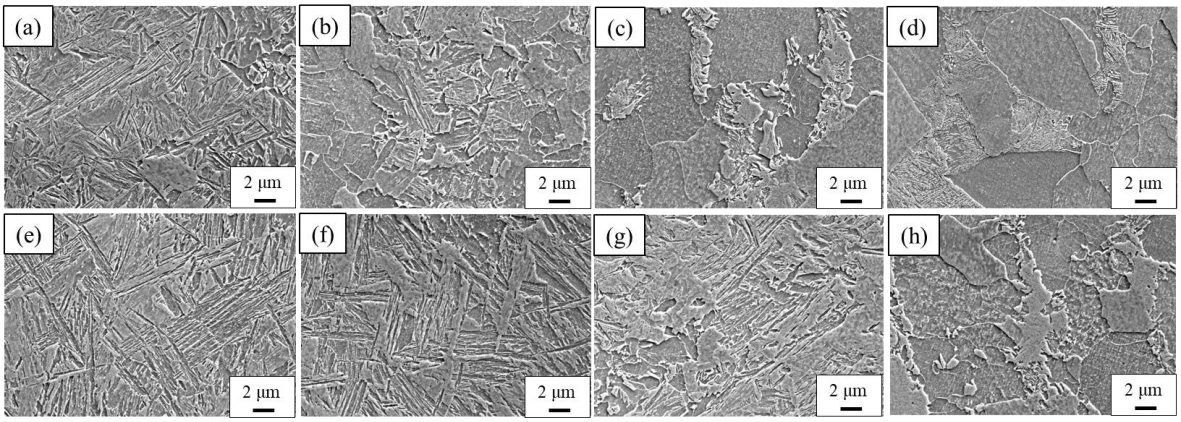

Figure 5.7 The microstructures of LFW joints of SMA490AW corresponding to the positions (a), (b), (c), (d), (e), (f), (g) and (h)

As seen in Figure 5.8 which illustrates the microstructures of LFW joints of SPA-H, the same trend in the microstructural evolution from the weld center to the BM can be observed as

SMA490AW. That is, the area fraction of bainites is obviously decreased at a small distance from the weld center, and the microstructure near the flash of the sample shows a larger area of the strengthening phase. Comparing the microstructures of SMA490AW to that of SPA-H, it is observed that SMA490AW generally has a much larger area fraction of bainites than SPA-H, which results in the much higher microhardness of SMA490AW as seen in Figure 5.6.

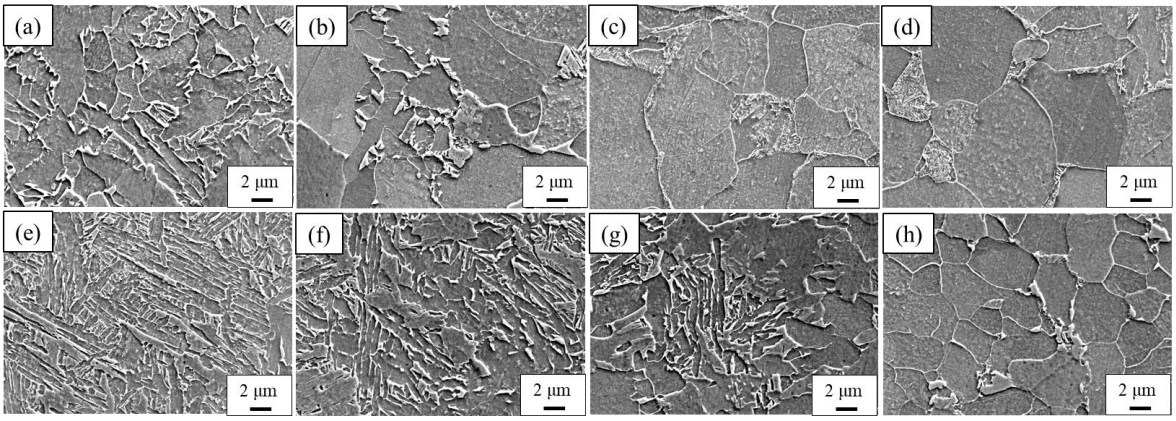

Figure 5.8 The microstructures of LFW joints of SPA-H corresponding to the positions (a), (b), (c), (d), (e), (f), (g) and (h)

5.3. Ductile performance

5.3.1. Yield and fracture characteristics of finely polished LFW specimens

The load-displacement relationship of LFW joints under monotonic loading is shown in Figure 5.9(a) and (c), and the strain contours corresponding to the typical loading time are also added. To differentiate, the oscillation side during the LFW joining process is pointed out in the contours. It is observed that the yield occurred separately at the BM part on both sides of the WCZ. A small time difference occurred between the yield on both sides, *i.e.*, BM parts on the oscillation side and stationary side did not yield at the same time. The yield of the welded joint of SMA490AW illustrates visible front of the plastic deformation (Lüders band) [156]. The deformation of WCZ was always smaller than that of HAZ and BM throughout the whole loading process due to the strengthening phase bainites and high microhardness. The axial strain distribution corresponding to the six loading times in Figure 5.9(a) and (c) is shown in

Figure 5.9(b) and (d). The WCZ of high microhardness served as a fixed end with very small axial strain, and the axial strain of BM on the oscillation side is slightly smaller than that on the stationary side due to the higher microhardness. However, the difference is quite small and the deformation of the BM parts observed on both sides is almost symmetric during the first five loading times. With the occurrence of necking, a drastic increasing strain can be observed at the BM part on the stationary side, and ductile fracture finally happened. By comparison of the strain distribution of SMA490AW and SPA-H, the strain accumulation of WCZ of SMA490AW is much smaller than that of SPA-H, which results from the higher microhardness of SMA490AW as seen in Figure 5.6. Also, the slightly higher microhardness of the BM parts on the oscillation side can explain the reasons for the fracture of the BM on the stationary side for the two monotonic specimens in this research.

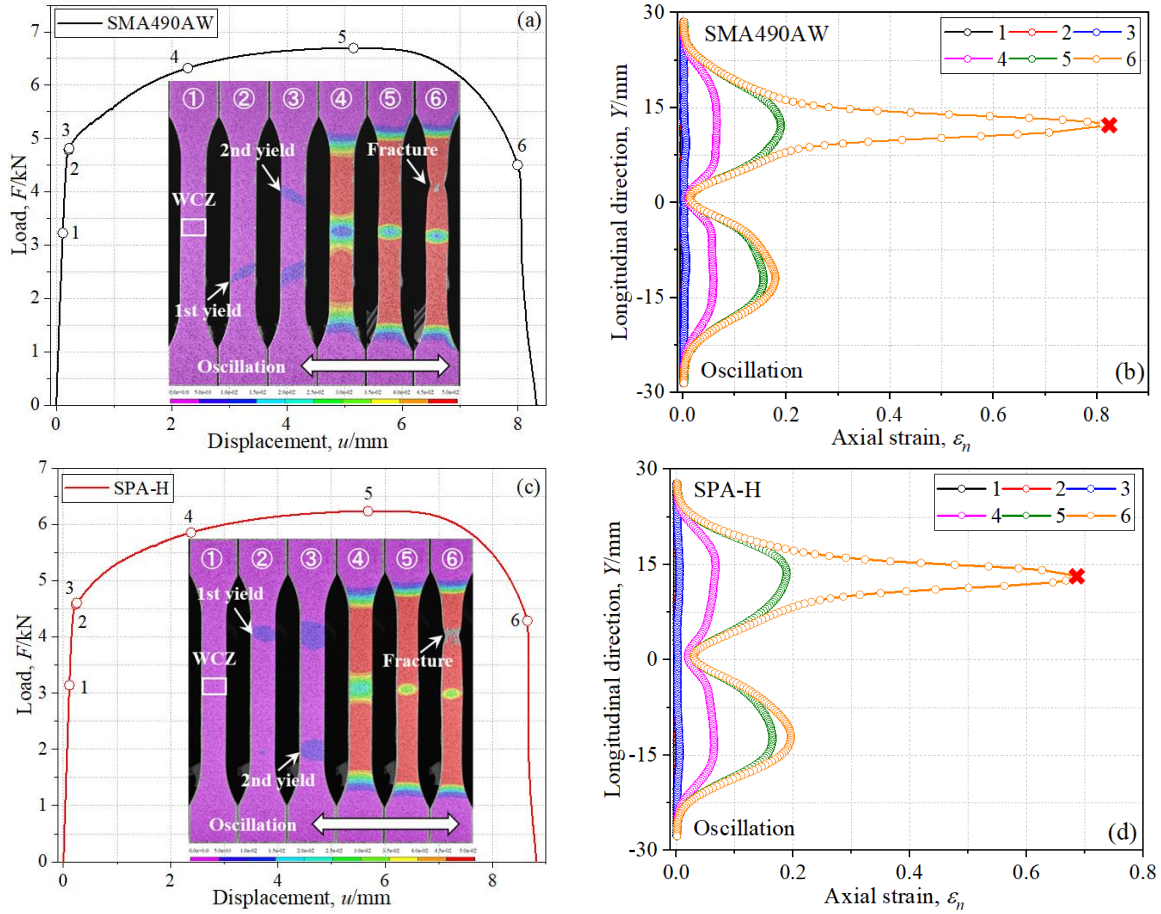

Figure 5.9 The tensile response measured by DIC for LFW joints of SMA490-AW and SPA-H (a) (c) represent the Load-Displacement curves and color-coded strain fields at separate steps; (b) (d) indicate the distribution of the axial strain

5.3.2. Yield and fracture characteristics of as-welded LFW specimens

The nominal stress - nominal strain relationship of the LFW specimen is illustrated in Figure 5.10(a), and data of the BM specimen are also added for comparison. The yield plateau can be observed for the BM specimen which is a common characteristic of mild steel. No plateau is shown for the LFW specimen due to the existence of strengthening phase bainite. There is no obvious difference between the tensile strength of the LFW specimen and that of the BM specimen, indicating that a joint efficiency of 100% is achieved. This is because the ductile fracture of the LFW specimen occurred in the region of the BM instead of the WCZ, thus the tensile strength of the LFW specimen actually depends on the BM. However, the elongation of the LFW joint is obviously smaller because the large plastic deformation was constrained to the BM on the oscillation side due to high microhardness of the WCZ.

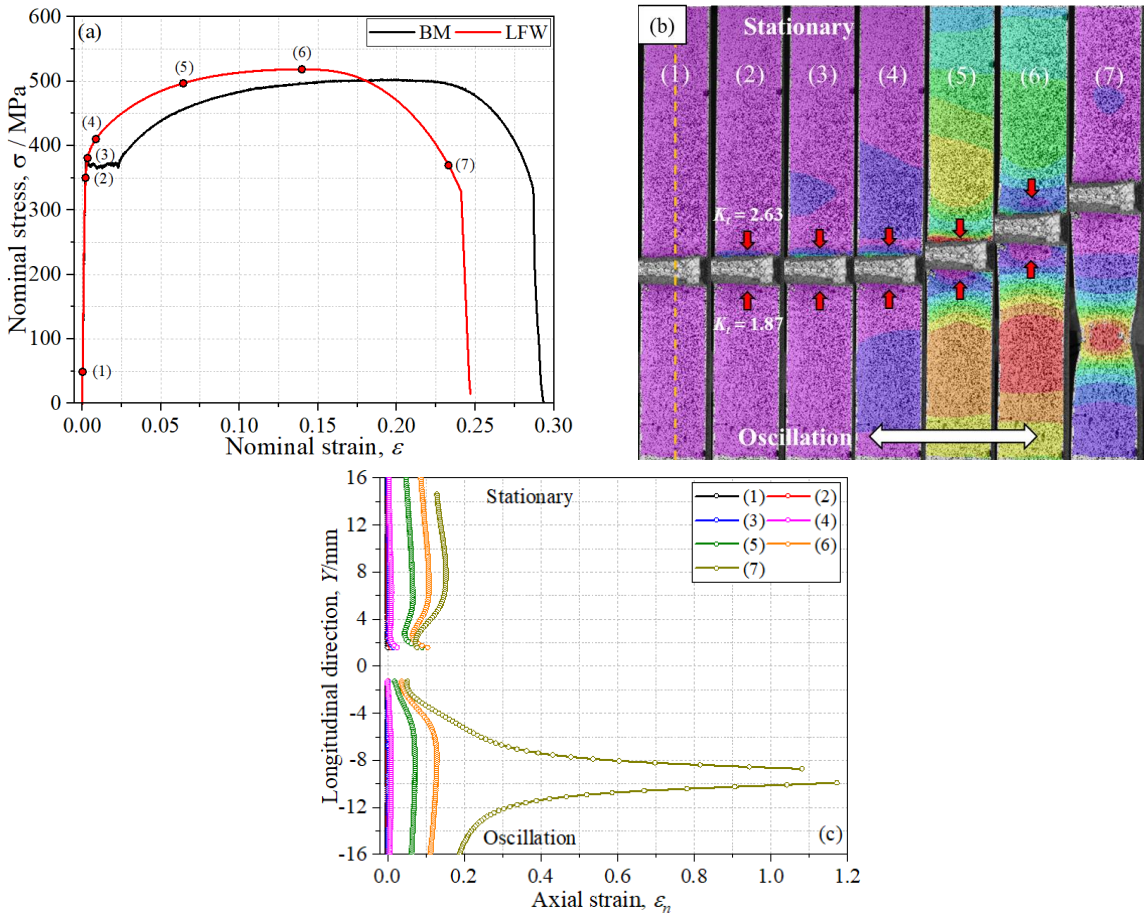

Figure 5.10 Monotonic experiment (a) nominal stress - nominal strain relationship of BM and LFW joints; (b) strain contour measured by DIC; (c) longitudinal strain distribution along the centerline

The strain contour corresponding to the typical loading time was measured using the DIC and shown in Figure 5.10(b). The axial strain distribution along the centerline of the specimen as marked in Figure 5.10(b) was also measured and shown in Figure 5.10(c). The strain of the flash failed to be measured because it could not be focused by the DIC cameras. As seen for the loading time (2), though the microhardness near the WCZ was higher than that of the BM, the yield first occurred at the weld toe on the stationary side due to the local stress concentration (K_t = 2.63). The BM on the stationary side yielded subsequently as seen for the loading time (3), followed by the yield of the BM on the oscillation side as seen the loading time (4). With the further development of hardening, the local strain of the BM on the oscillation side showed a higher growth rate than that of the weld toe on the stationary side as seen for the loading times (5) and (6). Necking occurred at the BM on the oscillation side and ductile fracture finally happened as seen for the loading time (7). The axial strain of the weld toe on the oscillation side was small during the whole loading history due to the high strength and lower stress concentration (K_t = 1.87).

5.3.3. Tensile properties

The nominal strain- nominal stress relationship of the BM specimens and LFW specimens is shown in Figure 5.11(a). The LFW specimens both fractured at the BM part of the specimen due to the high strength of strengthening phase bainites and lack of HAZ softening or welding defects. Therefore, the tensile strength of the LFW specimens is dependent on the strength of the BM part, and the tensile strength of the BM specimens and LFW specimens is very close. The tensile strength of the BM specimen (566MPa) of SMA490AW is slightly higher than that of the LFW specimen (554MPa), while the tensile strength of the BM specimen (502MPa) of SPA-H is slightly lower than that of the LFW specimen (513MPa). The joint efficiency for the two materials joined by LFW is close to 100%. The elongation of the LFW specimens is smaller than that of the BM specimens due to the small deformation of the WCZ. The BM specimens illustrate the typical yield behavior of mild steels with an obvious upper yield point and yield terrace, while no yield terrace can be observed for the LFW specimens due to the existence of bainites in the WCZ. The mechanical properties of the LFW joints of the two weathering steels

are shown in Figure 5.11(b). The welded joint of SMA490AW shows a higher tensile strength and yield strength than those of SPA-H, while a larger elongation can be observed for SPA-H.

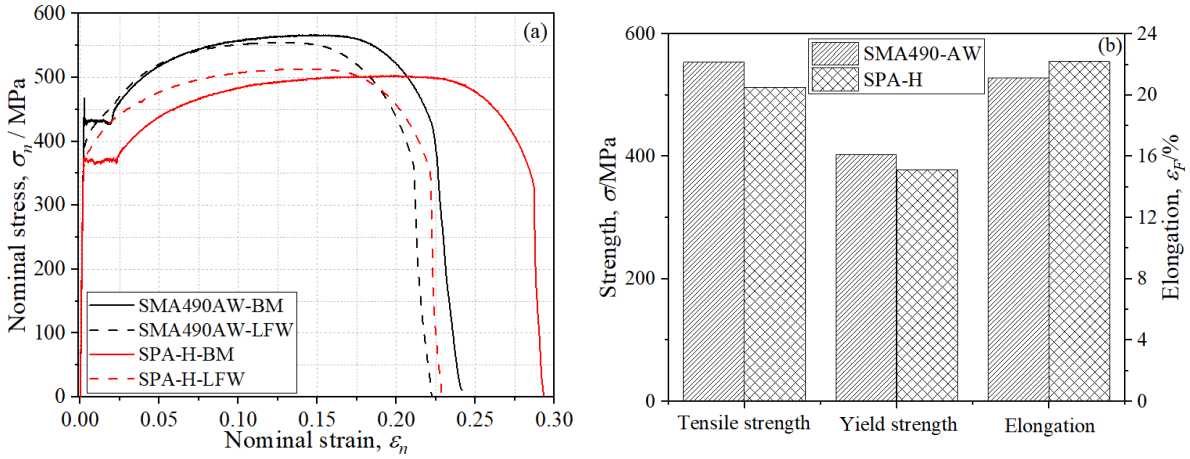

Figure 5.11 Mechanical properties of LFW joints (a) nominal stress- nominal strain curves; (b) comparison of mechanical properties

The fracture surface of both LFW specimens illustrates the typical features of ductile fracture as the specimens were fractured at the BM part which showed large plastic deformation. The fracture surface of the LFW joint of SMA490AW is illustrated in Figure 5.12 as an example. The obvious shrinkage of the fracture section can be observed in Figure 5.12(a). The fracture surface is fibrous. The coarse and fine dimples, which are approximately equiaxial, indicate the favorable ductile behavior of the weld joints by LFW as seen in Figure 5.12(b).

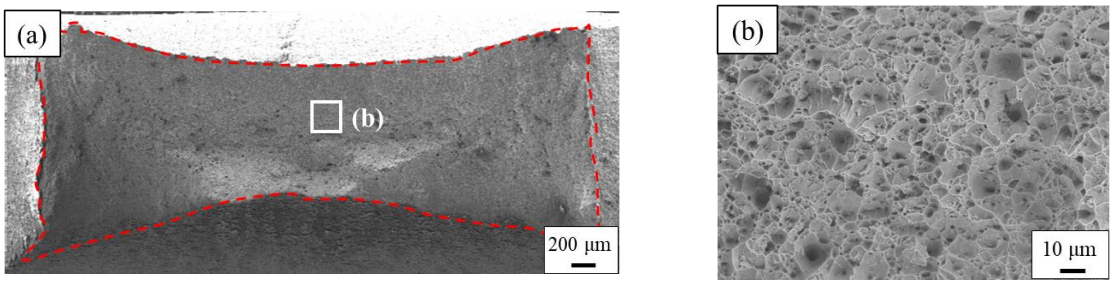

Figure 5.12 Fracture surface of LFW joint of SMA490AW (a) macrostructure feature; (b) microstructure feature

5.4. Fatigue performance of finely polished LFW joints

5.4.1. Fatigue strength

The fatigue test was carried out on six BM specimens and nine LFW specimens for both materials. The fatigue test was defined to be running out when the loading cycles were larger than 2×10^6. The fatigue testing results of BM and LFW specimens were summarized in Table 5.3. All LFW specimens were fractured at the BM part which was far from the WCZ and HAZ in this study. This is reasonable because the WCZ with a large area of bainites has a higher microhardness and strength than the BM, and no HAZ softening and welding defects are observed in the weld. Figure 5.13 shows the stress range $\Delta\sigma$ and fatigue fracture life N_f relationship of the BM specimens and LFW specimens. The design curve of FAT112 from IIW [151] was also added for reference. The yield stress σ_y and tensile strength σ_B of LFW joints were added in Figure 5.13 in the form of a stress range considering the stress ratio R of 0.1. According to the method of statistical analysis suggested by IIW, the S-N curves were fitted by the least square method and also considering the survival probability of 97.7% and 2.3%.

Table 5.3 Fatigue testing results of BM and LFW specimens

Material	Type	$\Delta\sigma$ /MPa	N_f /cycles	Material	Type	$\Delta\sigma$ /MPa	N_f /cycles
SMA490AW	BM	450.9	Run out	SPA-H	BM	445.5	141,404
		462.6	275,756			441.0	355,263
		459.0	Run out			436.5	Run out
		460.8	Run out			442.8	143,567
		468.0	260,758			440.1	369,888
		466.2	Run out			441.9	Run out
	LFW	456.6	407,001		LFW	450.0	Run out
		453.2	167,882			453.6	Run out
		441.0	Run out			459.0	265,736
		450.0	513,521			455.4	319,296

	446.4	Run out	454.5	266,259
	450.9	578,001	458.1	346,101
	449.1	327,201	454.0	478,297
	462.6	441,953	457.2	568,403
	466.2	170,201	459.9	297,509

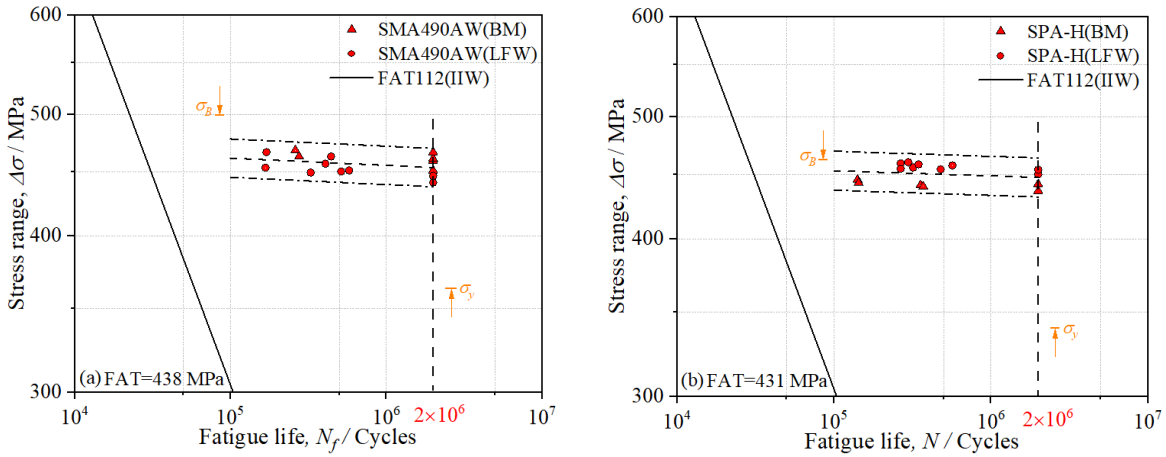

Figure 5.13 *S-N* curves of BM and polished LFW joints (a) SMA490AW; (b) SPA-H

As described in Section 5.3.3, the tensile strength of the BM specimens of SMA490AW is slightly higher than that of the LFW specimens, which contributes to the slightly higher fatigue strength of the BM specimens as seen in Figure 5.13(a). The same is true for SPA-H, because the slightly higher tensile strength of the LFW specimens results in the higher fatigue strength than the BM specimens as seen in Figure 5.13(b). However, the difference in the fatigue strength between the BM specimens and LFW specimens is very small because the LFW specimens were all fractured at the BM part, thus the S-N curves were fitted based on the BM specimens and LFW specimens as a whole. The S-N curves of the two steels are very flat compared to the design curve FAT112, and the fatigue strength is much higher than the design value. The fatigue strength of the two steels is very close though SMA490AW has a higher tensile strength than SPA-H as seen in Figure 5.11. Compared to the previous studies in which the welded joints usually fractured in a stress range below the yield point [136][139], the applied fatigue loading in this research should always be much higher than the yield stress σ_y to make the specimens fracture before running out. The specimens still exhibited a high-cycle

fatigue behavior even when the applied stress is rather close to the tensile strength σ_B. The high fatigue strength of the LFW specimens in this research can be explained by the absence of HAZ softening and welding defects. Also, the specimens were finely polished to remove the flash and geometry discontinuities.

5.4.2. Ratcheting behaviors and fractography

The ratcheting behaviors of different regions (WCZ, HAZ and BM on the stationary and oscillation side) were analyzed. The axial strain contour of one LFW specimen of SMA490AW ($\Delta\sigma$ = 466.2MPa) measured by DIC is shown in Figure 5.14(a). The strains were measured at the peak of applied stress except for the last figure which illustrates the condition of fatigue fracture. The scale of the contour was not identical throughout the strain history and set to change with the variation of the peak strain to illustrate the relative magnitude of strains at the different loading times. Defining n as a specific loading cycle, the percentage of the loading cycle n accounting for the whole fatigue life N_f is represented by n/N_f and indicated in each strain contour. It is observed that the strain of the BM part on the stationary side (BM-1) is generally larger than that on the oscillation side (BM-2) throughout the loading history due to the higher microhardness on the oscillation side. Also, the deformation of the WCZ and HAZ with strengthening phase is very small due to the high microhardness. The strain history of the LFW specimen of SMA490AW is illustrated in Figure 5.14(b). No obvious change in the axial strain can be observed for WCZ, HAZ and BM on the oscillation side during the whole loading history. The plastic deformation of BM-1 on the stationary side was slowly accumulated until a sharp increase occurred at n/N_f = 27.4%. This sharp increase in the strain occurred probably because the small crack nucleation reached a certain length. The net section was decreased and the increasing local stress resulted in the faster accumulation of plastic strain. The corresponding strain contour illustrated the change in the strain distribution where the region of high strain began to rotate and tilt toward the longitudinal axis. The tilt of the high strain region was more clear when n/N_f = 98.7% with the extension of the microcrack length, indicating a more drastic cyclic slip induced by the shear stress at an angle of about 45° with respect to the loading direction. A macrocrack was first observed at the flange of the specimen

due to the stress concentration when n/N_f = 99.3%, and the region of high strain was narrowed and concentrated on the crack tip. The second macrocrack was observed at n/N_f = 99.8% and the typical butterfly pattern of the strain distribution [63] started to form and became obvious when n/N_f = 99.9%. The fatigue failure finally occurred due to the first macrocrack, and obvious necking can be seen on the right of the fracture surface due to the final ductile fracture.

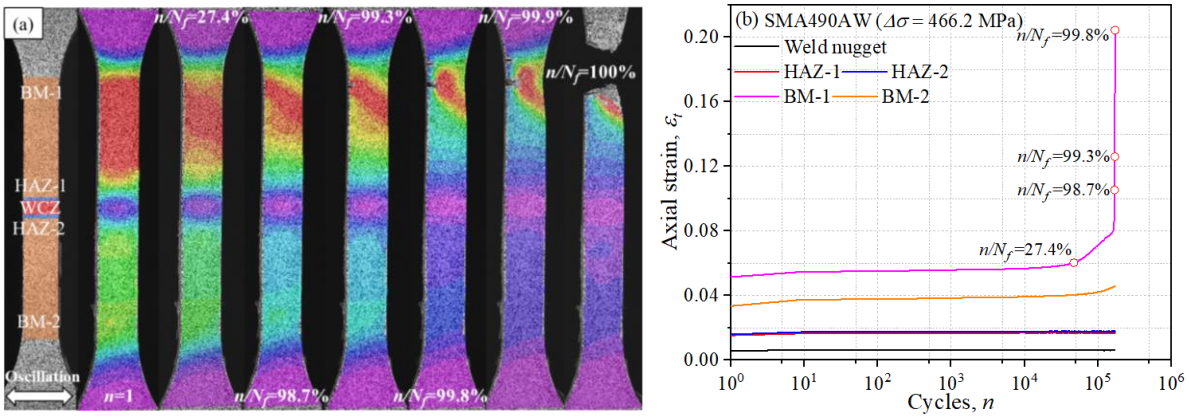

Figure 5.14 The strain distribution of one LFW specimen of SMA490AW ($\Delta\sigma$ = 466.2 MPa) (a) strain contour; (b) ratcheting strain

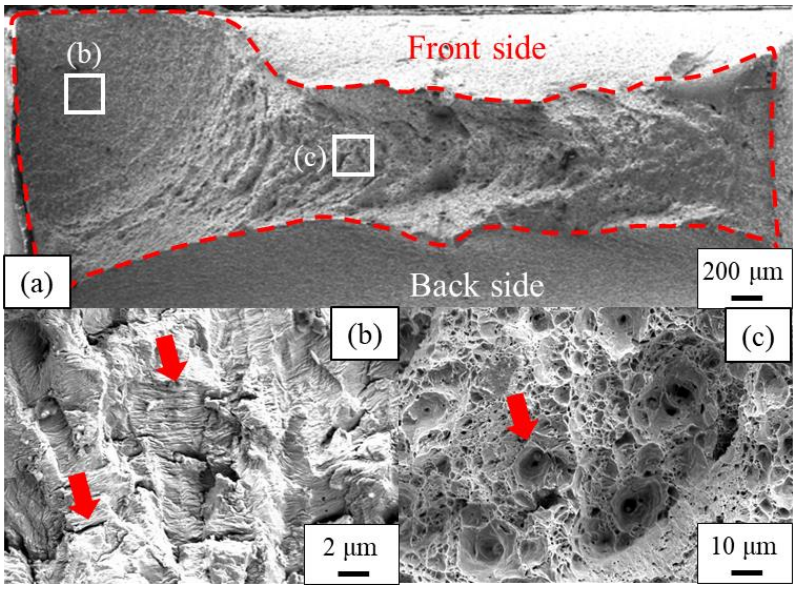

Figure 5.15 The fracture surface of one LFW specimen of SMA490AW ($\Delta\sigma$ = 466.2 MPa)

The fractography of the specimen in Figure 5.14 is shown in Figure 5.15. As seen in Figure 5.15(a), the front side indicates the specimen surface which was measured by DIC. The fractography features the crack propagation area and the final ductile fracture area. Very clear

river marks are observed in the crack propagation area and it can be speculated from the direction of the river marks and the ellipse-shaped area that the crack initiated from the front side of the specimen. The magnification of the crack propagation area in Figure 5.15(b) illustrates the cleavage fracture with several secondary cracks and fatigue striations. The large shrinkage of the section can be observed in the ductile fracture area compared to the crack propagation area. As seen in Figure 5.15(c), the ductile fracture surface is featured by numerous fine and coarse dimples.

The strain distribution of one LFW specimen of SPA-H ($\Delta\sigma$ = 458.1 MPa) measured by DIC is shown in Figure 5.16(a). An interesting phenomenon observed in this specimen is that the strain of the BM part on the stationary side (BM-1) was larger than that on the oscillation side (BM-2) during most of the loading history ($n/N_f \leq 98.9\%$), while the final fracture occurred on the oscillation side (BM-2). Many factors can contribute to this phenomenon such as the higher stress concentration of the arc on BM-2 due to the lower precision of fabrication, or a potential scratch induced by careless operation during the fatigue experiment. The region of high strain at an angle of about 45° with respect to the loading direction which indicates the direction of the cyclic slip suddenly occurred on the oscillation side at n/N_f = 99.2%, corresponding to the ratcheting behavior in Figure 5.16(b) is the drastically increased axial strain. The region of high strain first appeared on the left side of the specimen at n/N_f = 99.2% and propagated to the whole section at n/N_f = 99.5%, while the first macrocrack was observed on the right side as seen in the strain contour at n/N_f = 99.9%. With the aid of the fractography as seen in Figure 5.17(a), it can be understood that the crack actually initiated from the back side of the specimen according to the river mark direction and the ellipse-shaped area. Therefore, the macrocrack observed in Figure 5.16(a) at n/N_f = 99.9% was a through-wall crack which propagated from the back side. It is speculated that though a high strain region occurred on the left and front side of the specimen, a comparatively higher strain region existed on the right and back side of the specimen and resulted in the earlier crack initiation than the left side. Unfortunately, the strain distribution of the back side of the specimen is unavailable, thus it is difficult to confirm this speculation.

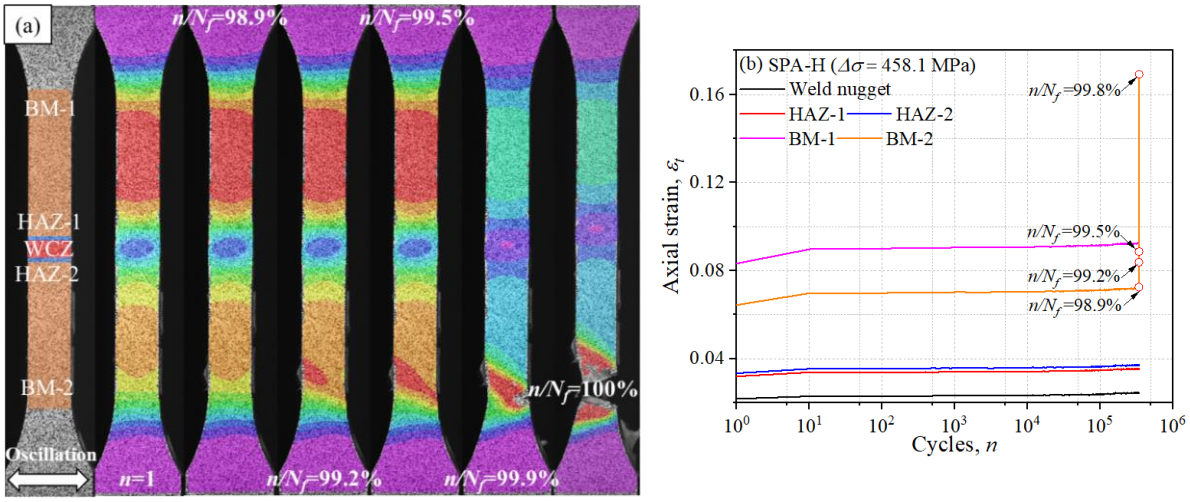

Figure 5.16 Strain distribution of one LFW specimen of SPA-H ($\Delta\sigma$ = 458.1 MPa) (a) strain contour; (b) ratcheting strain

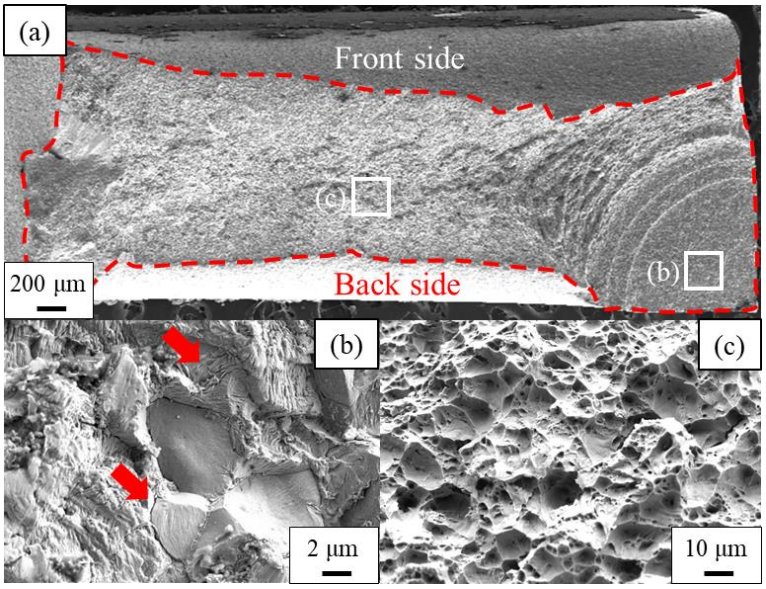

Figure 5.17 Fracture surface of one LFW specimen of SPA-H ($\Delta\sigma$ = 458.1 MPa)

The fractography of the LFW specimen of SPA-H ($\Delta\sigma$ = 458.1 MPa) is shown in Figure 5.17. Similar to that of SMA490AW, the river marks in Figure 5.17(a) are very obvious in the crack propagation area. Several intergranular fractures are illustrated in the magnified crack propagation area with the secondary crack deflected at the grain boundaries as seen in Figure 5.17(b). Fatigue striations are also observed surrounding the grains. The ductile fracture in Figure 5.17(c) features fine and coarse dimples.

5.5. Fatigue performance of as-welded LFW joints

5.5.1. Fatigue strength

As discussed in Section 5.2.2, the weld toe and interface are the potential crack initiation positions for the LFW joints due to the high stress concentration. Most of the LFW specimens in this study were characterized by a weld toe fracture as seen in Figure 5.18(a). This is because the flash usually shows a "mountain" shape as seen in Figure 5.4(b) and the high stress concentration is located at the weld toe. Only three LFW specimens illustrated weld interface fracture as seen in Figure 5.18(b). These specimens were cut from the edge of the LFW joints, and the flash shows a "wave" shape as seen in Figure 5.4(b). In this case, the weld interface can have a higher stress concentration factor than the weld toe.

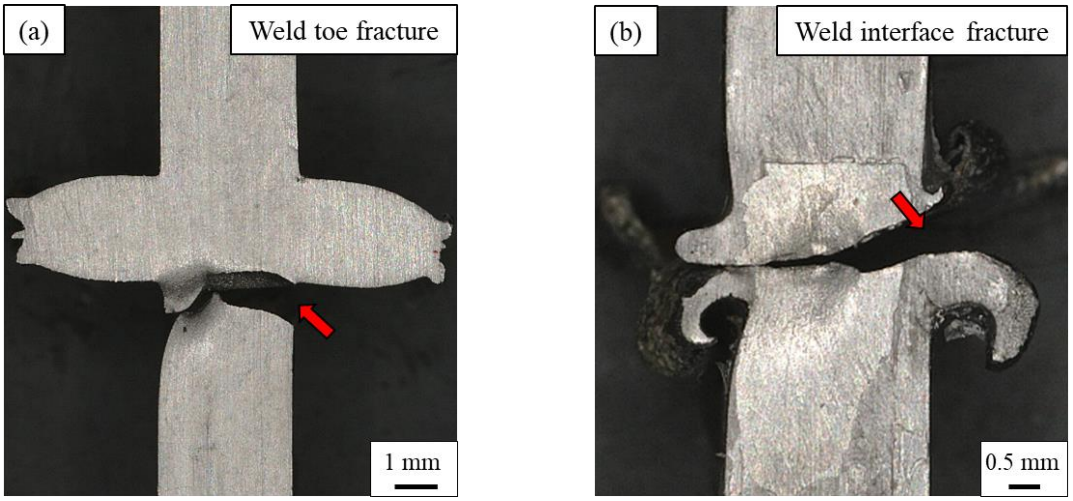

Figure 5.18 Fatigue fracture characteristics (a) weld toe fracture ($\Delta\sigma$ = 338 MPa, N_f = 558630); (b) weld root fracture ($\Delta\sigma$ = 360 MPa, N_f = 361342)

The relationship of the nominal stress range $\Delta\sigma$ - fatigue fracture life N_f of the LFW specimens in this research is illustrated in Figure 5.19 by the circles. Three LFW specimens that fractured from the weld interface were pointed out in this figure. The fatigue test was defined to be running out when the loading cycles were larger than 2×10^6. The testing results were fitted by the least square method, and the fatigue strength FAT of the LFW specimens is

308 MPa defined by the stress range $\Delta\sigma$ at $N_f = 2 \times 10^6$ cycles. As seen in Figure 5.19, a certain discreteness can be observed among the testing data due to the variation of the geometries. The fatigue life of the LFW specimens is much higher than the FAT90 design curve proposed by IIW [151], indicating that the welding conditions of LFW in this research can contribute to a very favorable fatigue strength.

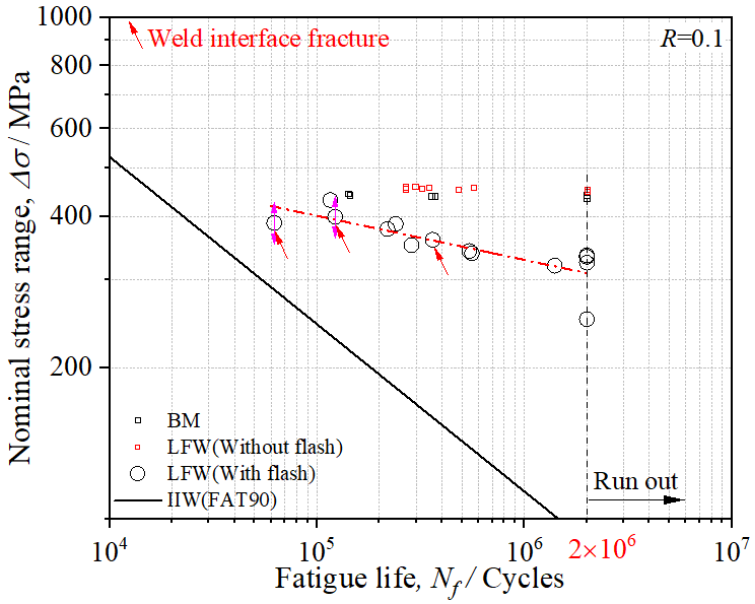

Figure 5.19 *S-N* curve of as-welded LFW specimens

The fatigue testing results of the BM specimens and finely polished LFW specimens (without flash) from Section 5.4 were also added in Figure 5.19 for comparison. It is worth noting that the LFW specimens without flash all fractured from the BM region of the specimen due to the high strength of the WCZ, absence of HAZ softening and smooth geometry. Therefore, the fatigue strengths of the BM specimens and LFW specimens without flash are very close. It is observed that the fatigue strength of the LFW specimens with flash is obviously lower than that without flash, indicating that the stress concentration at the weld toe and interface greatly reduced the fatigue life of the LFW joints.

5.5.2. Crack initiation and propagation behaviors

As discussed in Section 5.5.1, the LFW specimens are characterized by a fatigue fracture

at the weld toe or weld interface. The crack initiation and propagation behaviors were investigated with the aid of DIC. Taking one of the LFW specimens which was fractured at the weld toe as an example, the strain contours corresponding to the peak load are illustrated in Figure 5.20. The n/N_f represents the proportion of the current loading cycles accounting for the total fatigue life. The relationship of the crack length to the loading cycles was also measured and shown in Figure 5.21(a). In Cycle1 (n = 1), the BM generally yielded while the strain of the WCZ was much smaller due to the higher microhardness. The large strain due to the stress concentration could be observed at the weld toes as pointed out in the figure with a true strain ε_t of 0.00658 and 0.00576, respectively. These two weld toes were the potential crack initiation positions for this specimen. Due to the higher microhardness, the peak strain of the WCZ at the weld toes was lower than the BM in spite of the stress concentration.

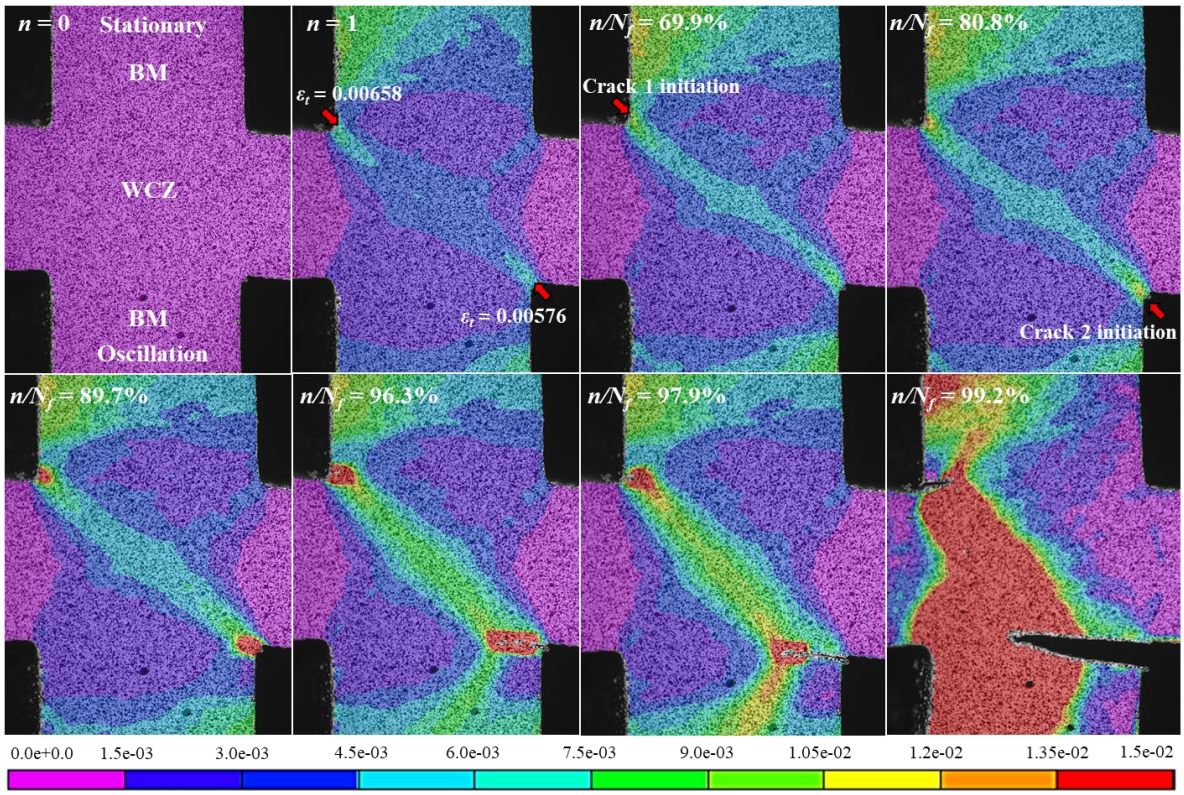

Figure 5.20 Strain contour of one LFW specimen with weld toe fracture ($\Delta\sigma$ = 387 MPa , N_f = 240822)

The crack initiation first occurred at the weld toe on the stationary side due to the higher peak strain when n/N_f = 69.9%. The crack initiation life accounted for a large fraction of the

total fatigue life. When n/N_f = 80.8%, the second crack was also initiated at the weld toe on the oscillation side with a smaller peak strain. With the accumulated plastic strain and crack propagation, the peak strain of the WCZ at the weld toes continue to increase and became larger than the BM. As seen in Figure 5.21(a), although Crack1 was firstly initiated, Crack2 illustrated a higher growth rate and reached the same crack length as Crack1 when n/N_f = 89.7%. With the fast propagation of Crack2, the area of high strain in the WCZ was also increased as seen for the figure of n/N_f = 96.3% and n/N_f = 97.9%. The WCZ in front of Crack1 and Crack2 finally illustrated a significant plastic deformation and the fatigue fracture was about to occur as seen for n/N_f = 99.2%.

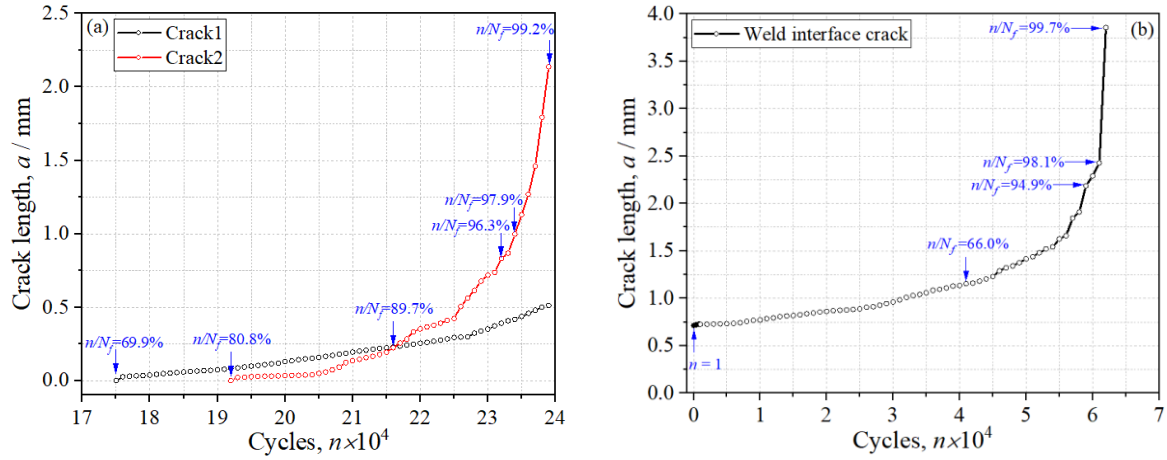

Figure 5.21 Relationship of crack length to loading cycles (a) weld toe fracture ($\Delta\sigma$ = 387 MPa , N_f = 240822); (b) weld interface fracture ($\Delta\sigma$ = 389 MPa , N_f = 62165)

The fatigue fracture that occurred at the weld interface was only observed for the LFW specimens sliced near the edge of the LFW joints, because the stress concentration at the weld interface can be higher than that at the weld toe in this case. Among the three specimens fractured at the weld interface as seen in Figure 5.19, two of them showed comparable fatigue strength as those fractured at the weld toe. As seen in Figure 5.3(a), the stress concentration factor of Slice6 with potential weld interface fracture is not very different from that of Slice1-5 with a potential weld toe fracture, thus it is reasonable for these two types of fatigue fracture to show very close fatigue strength. As seen in Figure 5.19, only one specimen fractured at the weld interface illustrates a comparatively shorter fatigue life below the fitted S-N curve, the

strain contours of which are shown in Figure 5.22. The crack initiation occurred at n = 1 due to the unbonded weld interface, which resulted in the sharp crack tip and drastically decreased the fatigue life. The crack propagation life accounted for 100% of the total fatigue life. The weld toe on the stationary side as pointed out in the figure showed a large stress concentration, which was also the potential position of crack initiation for this specimen. With the crack propagation, the area of high strain in the WCZ increased as seen for n/N_f = 66.0%. The crack at the weld toe on the stationary side was not initiated until n/N_f = 94.9% when the crack at the weld interface was very long. The bearing capacity of the section was severely lost at this time, and the local high stress resulted in the quick crack initiation and propagation. The crack at the weld toe on the stationary side propagated in two directions as seen for n/N_f = 98.1%. The WCZ in front of the crack illustrated a significant plastic deformation and the fatigue fracture was about to occur as seen for n/N_f = 99.7%. To ensure the high fatigue strength of the LFW joints, it is suggested to remove the flash near the edge in order to reduce the risk of unbonded flash.

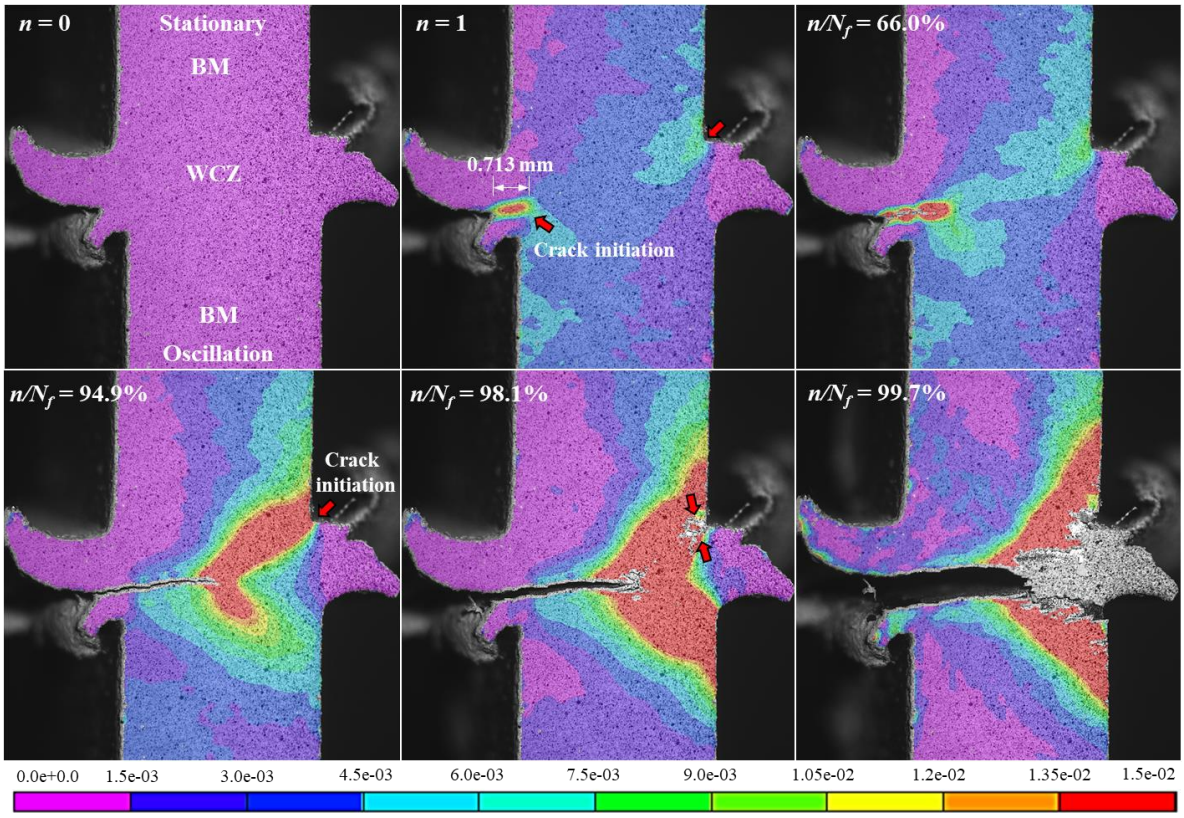

Figure 5.22 Strain contour of one LFW specimen with weld interface fracture ($\Delta\sigma$ = 389 MPa , N_f = 62165)

5.5.3. Fractography characteristics

The fracture surfaces of two specimens in Section 5.5.2 are shown in Figure 5.23 and Figure 5.24. As seen in Figure 5.23(a) corresponding to the LFW specimen of Figure 5.20, the fracture surface is characterized by a crack propagation region with an elliptical shape and a ductile fracture region with a fibrous pattern. The beach marks are very clear and indicate the direction of crack propagation. The white steps in Figure 5.23(b) represent the several spots of crack initiation, and were connected to one fracture surface with the further development of crack propagation. Figure 5.23(c) shows the typical cleavage fracture with obvious plateaus and fatigue striations. The fracture surface is also featured with secondary cracks as seen in Figure 5.23. The ductile fracture region illustrated in Figure 5.23(e) shows large and deep dimples surrounded by fine dimples, indicating a favorable ductility.

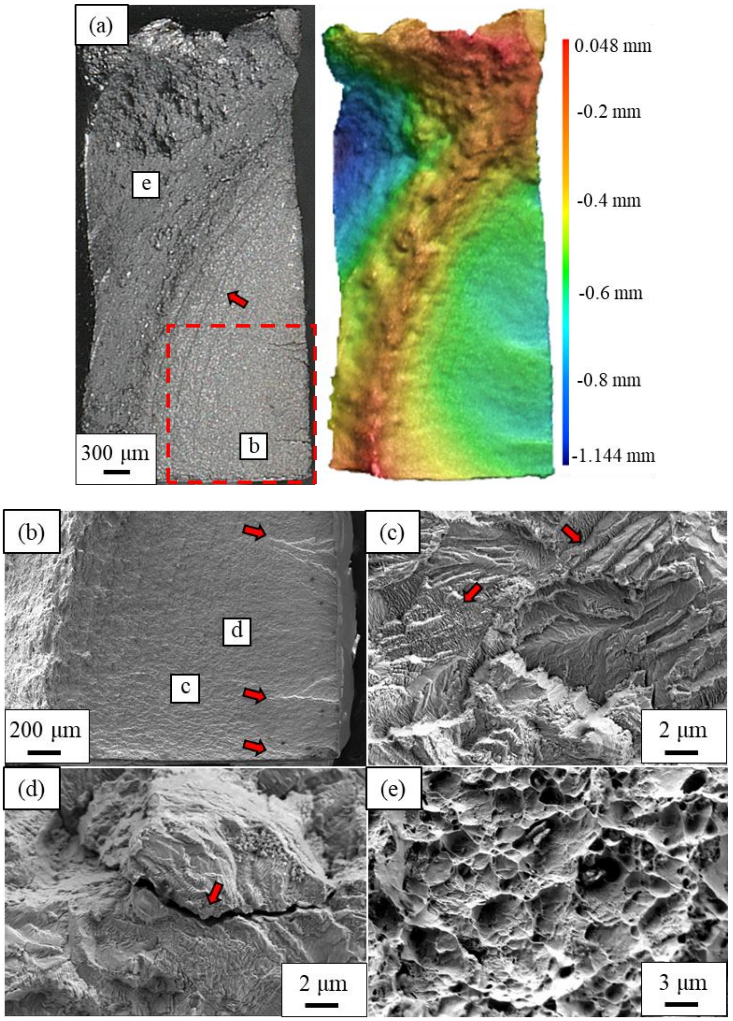

Figure 5.23 Fractography characteristics of weld toe fracture ($\Delta\sigma$ = 387 MPa , N_f = 240822)

Figure 5.24(a) shows the weld interface fracture of the LFW specimen corresponding to Figure 5.22. The fracture surface also consisted of an obvious fatigue propagation area and ductile fracture area. The flashes were on two sides of the fracture surface, and a clear shear lip corresponding to the final fracture can be observed. As elaborated in Section 5.5.2, the unbonded weld interface resulted in crack initiation at the first cycle, which is shown in Figure 5.24(b). The black area corresponds to the oxidized flash which was unbonded and opened under a low loading. The high stress concentration on the tip of the flash resulted in the monotonic fracture at the first cycle, which is shown in Figure 5.24(c). Figure 5.24(c) shows the flat brittle fracture surface with no dimples, because the weld interface consisted of a large fraction of bainite with very low ductility as seen in Figure 5.8(a). The length of the flash and the brittle fracture area was 0.730 mm which was roughly consistent with the crack length of the first cycle (0.713 mm) as measured in Figure 5.22.

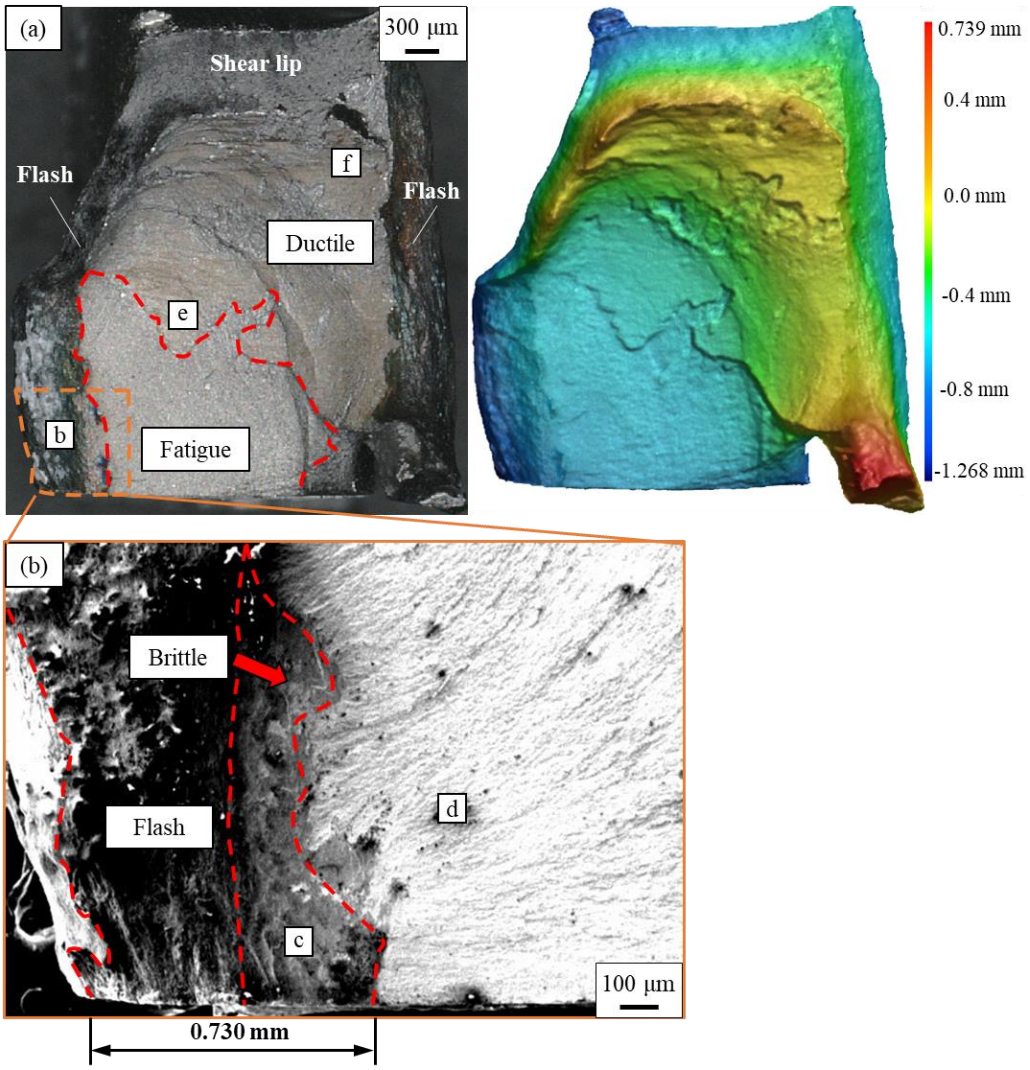

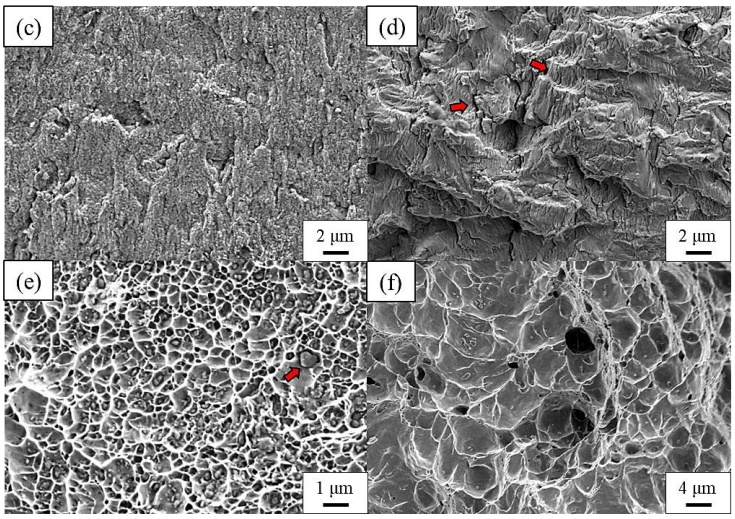

Figure 5.24 Fractography characteristics of weld interface fracture ($\Delta\sigma$ = 389 MPa , N_f = 62165)

Figure 5.24(d) shows the cleavage fracture surface with obvious plateaus, fatigue striations and secondary cracks. A large height difference can be observed for the ductile fracture surface in Figure 5.24(a), resulting in two different types of dimples illustrated in Figure 5.24(e) and (f). Figure 5.24(e) shows the fracture surface of the position near the weld interface, illustrating small and shallow dimples with a lot of second phase particles. This is because the area fraction of bainite is still high and the ductility is comparatively poor. In Figure 5.24(f) where the fracture surface is comparatively far from the weld interface, large and deep dimples can be observed due to the smaller area fraction of bainite and more favorable ductility.

5.5. Conclusions

In this chapter, the conventional weathering steels SMA490AW and SPA-H were joined by LFW above the A_3 temperature. The residual stress was measured and compared to that from references. The stress concentration factor of LFW joints was assessed by FEM corresponding to different positions of the flash. The microstructure characteristics, mechanical properties and fatigue behaviors of the as-welded and polished LFW joints were investigated. The specific conclusions are as follows:

(1) The bainite with high microhardness was formed at the WCZ. The area fraction of the

bainite is obviously decreased and that of the ferrite is increased at a very small distance from the WCZ, indicating the large welding temperature gradient. The larger area fraction of the bainite at the WCZ of SMA490AW results in the much higher microhardness than that of SPA-H.

(2) With the distance decreasing from the flash, the area fraction of bainite corresponding to the high microhardness is increased. This can be explained by the higher freedom of plastic flow of the materials at the edge of the workpieces which results in the larger friction heats.

(3) The LFW joints experienced two steps of yield due to the high microhardness and strength of WCZ. The ductile fracture of LFW joints occurred at the BM part for both polished and as-welded specimen. The tensile strength of polished and as-welded specimen is very close to that of BM, resulting in a joint efficiency close to 100%.

(4) The flash of the LFW joints usually illustrates a “mountain” shape which results in the fatigue fracture at the weld toe with a high stress concentration. However, the flash near the edge of the LFW joints shows a “wave” shape, causing the higher stress concentration at the weld interface where the fatigue fracture is prone to occur.

(5) The fatigue strength of the polished LFW specimens is close to that of the base metals due to the absence of welding defects and HAZ softening. The proposed *S-N* curves are very flat and illustrate a much higher fatigue strength compared to the FAT112 design curve.

(6) The flash greatly decreased the fatigue life of the LFW specimens due to the local stress concentration. Nevertheless, the proposed *S-N* curve of the as-welded LFW specimens still illustrated a much higher fatigue strength than the FAT90 design curve suggested by IIW.

(7) The possible unbonded flash at the edge caused the quick crack initiation and propagation at the weld interface, which greatly reduced the fatigue life of the LFW joints. It is suggested to remove the flash near the edge to ensure the high fatigue strength.

Chapter 6.

Conclusions and future works

6.1. Conclusions

In this dissertation, weathering steels with high wt.% P were successfully joined by FSW and LFW in the solid state. Weathering steels can significantly improve the anti-corrosion performance of steel structures, while the solidification cracks are prone to occur if joined by conventional fusion welding. FSW and LFW can join weathering steels at low temperature, which effectively inhibits the P segregation and solidification crack. The microstructure, geometry characteristics, residual stress, ductile properties and fatigue strength of conventional weathering steels joined by FSW and LFW were comprehensively studied. To give full play to potentials of friction welding, the new weathering steels with higher wt.% P and anti-corrosion performance were also developed and joined by FSW. The specific conclusions drawn from each chapter are summarized below.

In Chapter 1, a brief overview of weathering steels and friction welding, including development history, conceptualization, characteristics, advantages and potential industrial applications, was conducted. Also, the challenges and limitations were discussed to highlight the advantages of joining weathering steels by the friction welding, and the necessity of ensuring no solidification cracks and favorable mechanical properties.

In Chapter 2, the optimization of welding parameters and process of FSW and LFW was elaborated. The new weathering steels with higher wt.% P were developed and joined by FSW after the successful joining of conventional weathering steels. The experimental process to

investigate the microstructure, geometry characteristics, residual stress, ductile properties and fatigue strength of FSW and LFW joints was described. The anti-corrosion properties of conventional and high-phosphorus weathering steels assessed by the corrosion resistance index *I* is: Steel3 > Steel2 > SPA-H > Steel1 > SMA490AW. The global and local strain measured by DIC can result in a spatial resolution of about 7.1×10^{-3} mm^2/pixel and 1.1×10^{-5} mm^2/pixel, respectively.

In Chapter 3, conventional weathering steels (SMA490AW and SPA-H) were joined by FSW below A_1 temperature with no defects. The geometry and residual stress were measured, and the basin-shaped weldment with fine-grained ferrite and strengthening phase cementite was observed. No softening is observed at HAZ by the microhardness assessment. The yield and fracture characteristics of FSW were monitored by DIC, and FSW joints experienced two steps of yield due to the high microhardness and strength of weldment. The joint efficiency of SMA490AW and SPA-H by FSW can be as high as 100%. The fatigue tests were also conducted on the FSW joints under a stress ratio of 0.1. The BM and FSW specimens of weathering steels have almost identical fatigue strength due to the absence of HAZ softening and notches, indicating a favorable weldability. The fatigue strength of the FSW joints is much higher than the design curve FAT112.

In Chapter 4, three kinds of new weathering steels with higher wt.% P were developed and also joined by FSW below A_1 temperature. The welded joints with no defects and HAZ softening were obtained for all steels. Influence of wt.% P and other alloying elements on the microstructure characteristics and microhardness was discussed. Specifically, the increasing wt.% P improves the microhardness and strength of the friction stir welded joints but weakens the ductile behavior. The solid solution of alloying elements (Ni, Cr and Nb) into the ferrite can enhance the ductile behavior and mechanical strength at the same time. The monotonic and fatigue tests show that FSW can achieve a joint efficiency of 100% for three new weathering steels with high wt.% P. The fatigue strength of FSW and BM specimens was almost the same and much higher than the FAT112 design curve. The increasing wt.% P contributed to the enhancement of the anti-corrosion performance and fatigue strength. The alloying elements such as the Ni, Cr and Nb resulted in a further improvement of anti-corrosion performance and fatigue strength. The mechanical properties of FSW with solidification cracks due to the

inadequate downward load were also discussed. The weld defects resulted in the fatigue fracture at the weld nugget and decreased the fatigue life by as long as 14.7 times, but they barely had no influence on the tensile strength.

In Chapter 5, conventional weathering steels (SMA490AW and SPA-H) were joined by LFW above A_3 temperature. The residual stress was measured and compared to other steels joined by LFW, thus a general residual stress distribution for LFW joints was summarized. The stress concentration of LFW joints corresponding to various flash shapes was assessed by FEM. Due to the higher welding temperature, the bainite with high microhardness were formed at the WCZ. The area fraction of the bainite is obviously decreased and that of the ferrite is increased at a very small distance from the WCZ, indicating the large welding temperature gradient. Similar to the FSW joints, the LFW joints also experienced two steps of yield under the monotonic loading due to the high microhardness and strength of WCZ. The tensile strength of polished and as-welded specimen is very close to that of BM, resulting in a joint efficiency close to 100%. The fatigue strength of the polished LFW specimens is close to that of the BM specimens and much higher than the design curve, while that of the as-welded LFW specimens is greatly decreased due to the local stress concentration. In addition, the possible unbonded flash at the edge caused the quick crack initiation and propagation at the weld interface, and it is suggested to remove the flash near the edge to ensure the high fatigue strength.

In Chapter 6, this dissertation was concluded, and some suggestions for future work were proposed.

6.2. Recommendations for future works

The objective of this research is to join the weathering steels with high wt.% P by FSW and LFW at low temperature to inhibit P segregation and obtain the welded joints with no solidification cracks. Based on the successful joining of conventional and high-phosphorus weathering steels, the microstructure and mechanical properties of FSW and LFW joints were assessed. The high ductile strength and fatigue strength of FSW and LFW joints were confirmed. Although FSW was successfully conducted on the weathering steels below A_1

temperature, the discussion of mechanical properties was limited in the very thin plate (3 mm) and finely polished specimens. The steel plates in real engineering structures often have a larger thickness. Compared to the thin plate, a large temperature gradient can occur between the surface and interior of the thick plate during the welding, easily resulting in the large angular distortion and coarse grains. How to ensure sufficient heat input through the thickness of plates to promote the plastic flow of materials is also a major problem. Also, the thickness effects on mechanical properties of joints should also be seriously considered. The further works should focus on the FSW of thick plates and optimize the welding parameters to ensure no solidification cracks. On the other hand, steel structures often work in an as-welded state in the real engineering. The fatigue strength of welded joints can be significantly decreased due to the stress concentration of notches at the weldment. The notch effects of flashes on mechanical properties of FSW joints should be clarified.

In spite of the high ductile and fatigue strength, the LFW joints of weathering steels welded above A_3 temperature cannot give full play to the advantages of friction welding, i.e., achieving welded joints with high toughness and strength at the same time. The weathering steels with 0.3% P have been proved to be successfully joined by FSW below A_1 temperature, and the welded joints show favorable toughness with a DBTT as low as -175°C. But the toughness experiment conducted at the same temperature shows brittle fracture for the FSW joints welded above A_3 temperature. Similarly, the LFW joints welded above A_3 temperature, though have high tensile and fatigue strength, cannot have favorable toughness as that welded below A_1 temperature. Further efforts are needed to optimize the LFW parameters to join weathering steels below A_1 temperature and ensure no solidification cracks.

Moreover, the existing fatigue design curves of fusion welded joints often result in a very conservative assessment of fatigue life for the FSW and LFW joints in this research. The thickness effect is one of the most significant factors to be considered for the accurate fatigue life assessment. Besides, the recrystallization processes of fusion welding and friction welding are quite different, resulting in different microstructures and mechanical properties. Therefore, it is still not clear whether the existing fatigue design curves can be used to assess the friction welded steels. In addition, the bead geometry of FSW and LFW joints is also very different from that of fusion welded joints. It is well-known that stress concentration resulting from

various bead profile can have significant influence on the fatigue life. The novel method of fatigue life prediction for the FSW and LFW joints should be proposed to achieve a higher precision.

References

[1] Y. Wang, Z. Fu, H. Ge, *et al.*, Cracking reasons and features of fatigue details in the diaphragm of curved steel box girder, *Eng. Struct.*, 2019, 201, 109767.

[2] Y. Wang, B. Ji, Z. Fu, *et al.*, Fatigue repairing craftsmanship of deck-to-vertical stiffener weld in the steel bridge deck, *Adv. Steel Constr.*, 2019, 15(3), 232-241.

[3] S. Tsutsumi, R. Fincato, P. Luo, *et al.*, Effects of weld geometry and HAZ property on low-cycle fatigue behavior of welded joint, *Int. J. Fatigue*, 2022, 156, 106683.

[4] S. Tsutsumi & R. Fincato, Cyclic plasticity model for fatigue with softening behaviour below macroscopic yielding, *Mater. Des.*, 2019, 165, 107573.

[5] Q. Wang, B. Ji, Z. Fu, *et al.*, Evaluation of crack propagation and fatigue strength of rib-to-deck welds based on effective notch stress method, *Constr. Build. Mater.*, 2019, 201, 51-61.

[6] J. Leander, A. Andersson, & R. Karoumi, Monitoring and enhanced fatigue evaluation of a steel railway bridge, *Eng. Struct.*, 2010, 32(3), 854-863.

[7] M. Virlogeux, Recent evolution of cable-stayed bridges, *Eng. Struct.*, 1999, 21(8), 737-755.

[8] M. Kitagawa, Technology of the Akashi Kaikyo Bridge, *Struct. Control Heal. Monit.*, 2004, 11(2), 75-90.

[9] B. Cao, Y. Ding, Y. Song, *et al.*, Fatigue life evaluation for deck-rib welding details of orthotropic steel deck integrating mean stress effects, *J. Bridg. Eng.*, 2019, 24(2), 4018114.

[10] A. M. Abdel-Ghaffar & R. H. Scanlan, Ambient vibration studies of Golden Gate Bridge: I. suspended structure, *J. Eng. Mech.*, 1985, 111(4), 463-482.

[11] M. Tai & C. Miki, Improvement effects of fatigue strength by burr grinding and hammer peening under variable amplitude loading, *Weld. World*, 2012, 56, 109-117.

[12] I. Kim, Fatigue strength improvement of longitudinal fillet welded out-of-plane gusset

joints using air blast cleaning treatment, *Int. J. Fatigue*, 2013, 48, 289-299.

[13] Z. Li, T. Chan, & R. Zheng, Statistical analysis of online strain response and its application in fatigue assessment of a long-span steel bridge, *Eng. Struct.*, 2003, 25(14), 1731-1741.

[14] X. Liu, C. Zhou, D. Feng, *et al.*, Experimental study on interlayer shear properties of ERS pavement system for long-span steel bridges, *Constr. Build. Mater.*, 2017, 143, 198-209.

[15] Q. Al-Kaseasbeh, Z. Lin, Y. Wang, *et al.*, Electrochemical characterization of steel bridge welds under simulated durability test, *J. Bridg. Eng.*, 2018, 23(10), 4018068.

[16] C. Hun, L. Boyuan, P. Arun, *et al.*, Effect of local damage caused by overweight trucks on the durability of steel bridges, *J. Perform. Constr. Facil.*, 2016, 30(1), 4014183.

[17] Y. Jeong, S. Kainuma, & J. Ahn, Structural response of orthotropic bridge deck depending on the corroded deck surface, *Constr. Build. Mater.*, 2013, 43, 87-97.

[18] W. Yang, P. Yang, X. Li, *et al.*, Influence of tensile stress on corrosion behaviour of high-strength galvanized steel bridge wires in simulated acid rain, *Mater. Corros.*, 2012, 63(5), 401-407.

[19] J. Ahn, I. Kim, S. Kainuma, *et al.*, Residual shear strength of steel plate girder due to web local corrosion, *JCSR*, 2013, 89, 198-212.

[20] M. Macho, P. Ryjáček, & J. Matos, Static and fatigue test on real steel bridge components deteriorated by corrosion, *Int. J. Steel Struct.*, 2019, 19(1), 110-130.

[21] C. Corleto & M. Hoerner, Corrosion and remaining life assessment, *J. Fail. Anal. Prev.*, 2022, 22(1), 181-190.

[22] M. El Aghoury & G. Khaled, Corrosion-fatigue strain-life model for steel bridge girders under various weathering conditions, *J. Struct. Eng.*, 2014, 140(6), 4014026.

[23] J. Kayser & A. Nowak, Capacity loss due to corrosion in steel-girder bridges, *J. Struct. Eng.*, 1989, 115(6), 1525-1537.

[24] Y. Zhang, K. Zheng, J. Heng, *et al.*, Corrosion-fatigue evaluation of uncoated weathering steel bridges, *Appl. Sci.*, 2019, 9(17), 3461.

[25] Y. Sharifi & R. Rahgozar, Fatigue notch factor in steel bridges due to corrosion, *Arch.*

Civ. Mech. Eng., 2009, 9(4), 75-83.

[26] A. Lichtenstein, The Silver Bridge Collapse Recounted, *J. Perform. Constr. Facil.*, 1993, 7(4), 249-261.

[27] H. Salem & H. Helmy, Numerical investigation of collapse of the Minnesota I-35W bridge, *Eng. Struct.*, 2014, 59, 635-645.

[28] R. Stanley, Tower bridge: History, recent inspection, assessment and 1993 repairs, *Constr. Repair*, 1994, 8(1), 2-4, 6-9.

[29] X. Jun, Y. Qingmei, & G. Rui, Analysis on fatigue load effects of bridge cables based on traffic load simulation, in *2014 7th International Conference on Intelligent Computation Technology and Automation*, 2014, 905-907.

[30] Federal Highway Administration, Silver Bridge collapsed, 2007. [Online]. Available: https://en.wikipedia.org/wiki/Silver_Bridge.

[31] M. Wills, I-35W Mississippi River Bridge collapsed, 2007. [Online]. Available: https://en.wikipedia.org/wiki/I-35W_Mississippi_River_bridge.

[32] H. Shen, P. Chen, & L. M. Chang, Automated steel bridge coating rust defect recognition method based on color and texture feature, *Autom. Constr.*, 2013, 31, 338-356.

[33] P. Liu, G. Geng, Y. Wang, *et al.*, Life prediction on protective coating of steel bridge based on gray system theory, in *2007 IEEE International Conference on Grey Systems and Intelligent Services*, 2007, 712-717.

[34] J. Jiang, A. Ma, X. Fan, *et al.*, Sherardizing and characteristic of zinc protective coating on high-strength steel bridge cable wires, *Adv. Mater. Res.*, 2010, 97-101, 1368-1372.

[35] K. Liao & Y. Lee, Detection of rust defects on steel bridge coatings via digital image recognition, *Autom. Constr.*, 2016, 71, 294-306.

[36] P. Chen, Y. Yang, & L. M. Chang, Automated bridge coating defect recognition using adaptive ellipse approach, *Autom. Constr.*, 2009, 18(5), 632-643.

[37] P. Chen, H. Shen, C. Lei, *et al.*, Fourier-Transform-Based method for automated steel bridge coating defect recognition, *Procedia Eng.*, 2011, 14, 470-476.

[38] K. Liao & D. Cheng, Restoration of the distorted color to detect the discoloration status of a steel bridge coating using digital image measurements, *Adv. Eng. Informatics*, 2017,

33, 96-111.

[39] B. Michel & Z. S. Mehdi, Effect of severe corrosion on cyclic ductility of steel, *J. Struct. Eng.*, 1997, 123(11), 1478-1486.

[40] Y. H. Jin, M. G. Ha, S. H. Jeon, *et al.*, Evaluation of corrosion conditions for the steel box members by corrosion monitoring exposure test, *Constr. Build. Mater.*, 2020, 258, 120195.

[41] J. Jia, X. Cheng, X. Yang, *et al.*, A study for corrosion behavior of a new-type weathering steel used in harsh marine environment, *Constr. Build. Mater.*, 2020, 259, 119760.

[42] V. Křivý & P. Konečný, Real material properties of weathering steels used in bridge structures, *Procedia Eng.*, 2013, 57, 624-633.

[43] V. Urban, V. Krivy, & K. Kreislova, The development of corrosion processes on weathering steel bridges, *Procedia Eng.*, 2015, 114, 546-554.

[44] J. Wang, F. Wei, Y. Chang, *et al.*, The corrosion mechanisms of carbon steel and weathering steel in SO2 polluted atmospheres, *Mater. Chem. Phys.*, 1997, 47(1), 1-8.

[45] H. Kihira & M. Kimura, Advancements of weathering steel technologies in Japan, *Corrosion*, 2011, 67(9), 95002-95013.

[46] Nippon Steel, Performance of weathering steel. [Online]. Available: https://www.weld.nipponsteel.com/techinfo/weldqa/detail.php?id=27V4HDH.

[47] V. K. Bupesh Raja, K. Palanikumar, R. Rohith Renish, *et al.*, Corrosion resistance of corten steel - A review, *Mater. Today Proc.*, 2021, 46, 3572-3577.

[48] J. R. Deepak, V. K. Bupesh Raja, & G. S. Kaliaraj, Mechanical and corrosion behavior of Cu, Cr, Ni and Zn electroplating on corten A588 steel for scope for betterment in ambient construction applications, *Results Phys.*, 2019, 14, 102437.

[49] H. Mansouri, S. A. Alavi, & M. Fotovat, Microbial-influenced corrosion of Corten steel compared with carbon steel and stainless steel in oily wastewater by pseudomonas aeruginosa, *JOM*, 2015, 67(7), 1594-1600.

[50] J. R. Deepak, V. K. Bupesh Raja, H. Soundararajan, *et al.*, Laser welding of ASTM Corten A588 grade steel - a case study, *Mater. Today Proc.*, 2021, 47, 4820-4826.

[51] American Society for Testing and Materials International, *Standard specification for high-strength low-alloy structural steel, up to 50 ksi [345 MPa] minimum yield point, with atmospheric corrosion resistance*, 2019.

[52] American Society for Testing and Materials International, *Standard specification for high-strength low-alloy structural steel*, 2018.

[53] American Society for Testing and Materials International, *Standard specification for steel, sheet and strip, high-strength, low-alloy, hot-rolled and cold-rolled, with improved atmospheric corrosion resistance*, 2018.

[54] American Society for Testing and Materials International, *Standard specification for cold-formed welded and seamless high-strength, low-alloy structural tubing with improved atmospheric corrosion resistance*, 2021.

[55] American Society for Testing and Materials International, *Standard specification for high-strength low-alloy structural steel plate with atmospheric corrosion resistance*, 2020.

[56] American Society for Testing and Materials International, *Standard specification for structural steel for bridges*, 2021.

[57] Japanese Industrial Standard Committee, *Superior atmospheric corrosion resisting rolled steels. JISG3125*, 2021. (In Japanese)

[58] China Standardization Adiministration, *Structural steel for bridge*, 2015. (In Chinese)

[59] Q. Zhang, J. Wu, J. Wang, *et al.*, Corrosion behavior of weathering steel in marine atmosphere, *Mater. Chem. Phys.*, 2003, 77(2), 603-608.

[60] New River Gorge Bridge, 2009. [Online]. Available: https://en.wikipedia.org/wiki/File:New_River_Gorge_Bridge.jpg.

[61] T. Kawakubo, K. Ushioda, H. Fujii, *et al.*, Friction stir welding of weathering steel and influence of C and P, in *National meeting of Japan Welding Society*, 2020, .

[62] Y. Murakami, Material defects as the basis of fatigue design, *Int. J. Fatigue*, 2012, 41, 2-10.

[63] J. Schijve, *Fatigue of structures and materials*, Springer, 2001.

[64] J. Nowacki & P. Rybicki, The influence of welding heat input on submerged arc welded

duplex steel joints imperfections, *J. Mater. Process. Technol.*, 2005, 164-165, 1082-1088.

[65] H. Zhang & J. Liu, Microstructure characteristics and mechanical property of aluminum alloy/stainless steel lap joints fabricated by MIG welding-brazing process, *Mater. Sci. Eng. A*, 2011, 528(19), 6179-6185.

[66] M. Vasudevan, V. Arunkumar, N. Chandrasekhar, *et al.*, Genetic algorithm for optimisation of A-TIG welding process for modified 9Cr-1Mo steel, *Sci. Technol. Weld. Join.*, 2010, 15(2), 117-123.

[67] Y. Zhao, X. Shi, K. Yan, *et al.*, Effect of shielding gas on the metal transfer and weld morphology in pulsed current MAG welding of carbon steel, *J. Mater. Process. Technol.*, 2018, 262, 382-391.

[68] S. Ravikumar, J. Vishal, K. Vigram, *et al.*, Material characteristic study of cold rolled graded thin sheet by using TIG welding process for rail coaches, 2017, 12(19), 5527-5531.

[69] V. Vairamani, N. Mohan, S. K. Karthikeyan, *et al.*, Optimization and microstructure analysis of Corten steel joint in mag welding by post heat treatment, *Mater. Today Proc.*, 2020, 21, 673-680.

[70] A. Kondo, Y. Kentaro, & A. Ono, Fatigue tests of welded joints of weathering steel and structural steel weathered for 25 years, *Doboku Gakkai Ronbunshuu A*, 2007, 63(3), 434-443.

[71] M. B. Uday, M. N. Ahmad Fauzi, H. Zuhailawati, *et al.*, Advances in friction welding process: a review, *Sci. Technol. Weld. Join.*, 2010, 15(7), 534-558.

[72] M. Maalekian, Friction welding - critical assessment of literature, *Sci. Technol. Weld. Join.*, 2007, 12(8), 738-759.

[73] W. Li, A. Vairis, M. Preuss, *et al.*, Linear and rotary friction welding review, *Int. Mater. Rev.*, 2016, 61(2), 71-100.

[74] D. Kumar Rajak, D. D. Pagar, P. L. Menezes, *et al.*, Friction-based welding processes: friction welding and friction stir welding, *J. Adhes. Sci. Technol.*, 2020, 34(24), 2613-2637.

[75] S. D. Meshram, T. Mohandas, & G. M. Reddy, Friction welding of dissimilar pure metals, *J. Mater. Process. Technol.*, 2007, 184(1), 330-337.

[76] S. Fukumoto, H. Tsubakino, K. Okita, *et al.*, Friction welding process of 5052 aluminium alloy to 304 stainless steel, *Mater. Sci. Technol.*, 1999, 15(9), 1080-1086.

[77] M. Maalekian, E. Kozeschnik, H. P. Brantner, *et al.*, Comparative analysis of heat generation in friction welding of steel bars, *Acta Mater.*, 2008, 56(12), 2843-2855.

[78] A. Vairis & M. Frost, On the extrusion stage of linear friction welding of Ti 6Al 4V, *Mater. Sci. Eng. A*, 1999, 271(1), 477-484.

[79] A. R. McAndrew, P. A. Colegrove, C. Bühr, *et al.*, A literature review of Ti-6Al-4V linear friction welding, *Prog. Mater. Sci.*, 2018, 92, 225-257.

[80] I. Oukra, N. Hagisawa, M. Naruo, *et al.*, Faitgue behavior of aluminum deck fabricated by friction stir welding, *J. Japan Soc. Civ. Eng.*, 2002, 703, 255-266.

[81] S. Walbridge, A. De, & C. Maadi, Opportunities for the use of Aluminum in Vehicular Bridge Construction 1 - Introduction 2 - Past use of Aluminum in Vehicular Bridges, *aluminm Assoc. od Canada*, 2012, 1-19.

[82] Historical photo of double spindle machine, 2020. [Online]. Available: https://commons.wikimedia.org/wiki/File:Historical_photo_of_double_spindle_machine..jpg.

[83] M. Uzkut, B. S. Unlu, S. Yilmaz, *et al.*, Friction welding and its applications in today's world, in *Proceedings of the 2nd International Symposium on Sustainable Development*, 2010, 8-9.

[84] J. Lopera, K. Mucic, F. Fuchs, *et al.*, Linear friction welding of high strength chains: Modelling and validation, *Math. Model. weld Phenom.*, 2013, 10, 203-218.

[85] W. M. Thomas, E. D. Nicholas, J. C. Needhan, *et al.*, International Patent Application PCT/GB92/02203 and GB Patent Application 9125978.8, 1991.

[86] Y. G. Kim, H. Fujii, T. Tsumura, *et al.*, Three defect types in friction stir welding of aluminum die casting alloy, *Mater. Sci. Eng. A*, 2006, 415(1), 250-254.

[87] S. Jones, Low force friction welding-What is it?, 2020. [Online]. Available: https://blog.mtiwelding.com/low-force-friction-welding.

[88] A. Vairis, G. Papazafeiropoulos, & A. Tsainis, A comparison between friction stir welding, linear friction welding and rotary friction welding, *Adv. Manuf.*, 2016, 4(4), 296-304.

[89] N. S. Kalsi & V. S. Sharma, A statistical analysis of rotary friction welding of steel with varying carbon in workpieces, *Int. J. Adv. Manuf. Technol.*, 2011, 57(9), 957-967.

[90] A. Z. Sahin, B. S. Yibaş, M. Ahmed, *et al.*, Analysis of the friction welding process in relation to the welding of copper and steel bars, *J. Mater. Process. Technol.*, 1998, 82(1), 127-136.

[91] P. Sathiya, S. Aravindan, & A. Noorul Haq, Effect of friction welding parameters on mechanical and metallurgical properties of ferritic stainless steel, *Int. J. Adv. Manuf. Technol.*, 2007, 31(11), 1076-1082.

[92] P. Wanjara & M. Jahazi, Linear friction welding of Ti-6Al-4V: Processing, microstructure, and mechanical-property inter-relationships, *Metall. Mater. Trans. A*, 2005, 36(8), 2149-2164.

[93] H. C. Dey, M. Ashfaq, A. K. Bhaduri, *et al.*, Joining of titanium to 304L stainless steel by friction welding, *J. Mater. Process. Technol.*, 2009, 209(18), 5862-5870.

[94] Pierce Industries, Friction welding: everything you need to know. [Online]. Available: https://www.pierceindustries.com/resources/friction-welding-everything-need-know/.

[95] M. Şahin & H. E. Akata, Joining with friction welding of plastically deformed steel, *J. Mater. Process. Technol.*, 2003, 142(1), 239-246.

[96] V. V Satyanarayana, G. Madhusudhan Reddy, & T. Mohandas, Dissimilar metal friction welding of austenitic-ferritic stainless steels, *J. Mater. Process. Technol.*, 2005, 160(2), 128-137.

[97] T. Kawakubo, T. Nagira, K. Ushioda, *et al.*, Friction stir welding of high phosphorus weathering steel —weldabilities, microstructural evolution and mechanical properties, *ISIJ Int.*, 2021, 61(7), 2150-2158.

[98] K. Kumar & S. V Kailas, The role of friction stir welding tool on material flow and weld formation, *Mater. Sci. Eng. A*, 2008, 485(1), 367-374.

[99] Y. Zhang, X. Cao, S. Larose, *et al.*, Review of tools for friction stir welding and

processing, *Can. Metall. Q.*, 2012, 51(3), 250-261.

[100] The Welding Institute, What is friction stir welding (FSW)?-Process and applications. [Online]. Available: https://www.twi-global.com/technical-knowledge/faqs/faq-what-is-friction-stir-welding.

[101] Y. Wang, S. Tsutsumi, T. Kawakubo, *et al.*, Effects of phosphorus content on fatigue performance of friction stir welded mild steels, *Constr. Build. Mater.*, 2022, 324, 126682.

[102] J. Jordon, R. Amaro, P. Allison, *et al.*, *Fatigue in friction stir welding*, Elsevier, 2019.

[103] H. Fujii, L. Cui, N. Tsuji, *et al.*, Friction stir welding of carbon steels, *Mater. Sci. Eng. A*, 2006, 429, 50-57.

[104] A. Tiwari, P. Singh, P. Pankaj, *et al.*, FSW of low carbon steel using tungsten carbide (WC-10wt.%Co) based tool material, *J. Mech. Sci. Technol.*, 2019, 33(10), 4931-4938.

[105] A. Fleury, R. Ranjan, L. Shah, *et al.*, Fatigue design of friction stir welded joints in aluminium bridge decks, *Proceedings, Annu. Conf. Can. Soc. Civ. Eng.*, 2019.

[106] R. Gadallah, S. Tsutsumi, Y. Aoki, *et al.*, Investigation of residual stress within linear friction welded steel sheets by alternating pressure via X-ray diffraction and contour method approaches, 2021, 64, 1223-1234.

[107] The Welding Institute, Linear friction welding. [Online]. Available: https://www.twi-global.com/technical-knowledge/job-knowledge/linear-friction-welding-146.

[108] J. W. Choi, W. Li, K. Ushioda, *et al.*, Flat hardness distribution in AA6061 joints by linear friction welding, *Sci. Rep.*, 2021, 11(1), 11756.

[109] J. Yang, J. Li, J. Xiong, *et al.*, Effect of welding parameters on microstructure characteristics and fatigue properties of dissimilar joints prepared by linear friction welding on TC11 and TC17 titanium alloys, *Weld. World*, 2020, 64, 683-695.

[110] J. W. Choi, Y. Aoki, K. Ushioda, *et al.*, Linear friction welding of Ti-6Al-4V alloy fabricated below β-phase transformation temperature, *Scr. Mater.*, 2021, 191, 12-16.

[111] Y. Aoki, R. Kuroiwa, H. Fujii, *et al.*, Linear friction stir welding of medium carbon steel at low temperature, *ISIJ Int.*, 2019, 59(10), 1853-1859.

[112] P. S. Effertz, F. Fuchs, & N. Enzinger, Modelling the flash formation of linear friction welded 30CrNiMo8 high strength steel chains, *Int. J. Adv. Manuf. Technol.*, 2017, 92,

2479-2486.

[113] L. Fratini, G. Buffa, D. Campanella, *et al.*, Investigations on the linear friction welding process through numerical simulations and experiments, *J. Mater.*, 2012, 40, 285-291.

[114] W. Li, T. Ma, & S. Yang, Microstructure evolution and mechanical properties of linear friction welded Ti-5Al-2Sn-2Zr-4Mo-4Cr (Ti17) Titanium alloy joints, *Adv. Eng. Mater.*, 2010, 12(1-2), 35-43.

[115] D. S. Lachowicz, C. Bennett, D. A. Axinte, *et al.*, On the influence of tooling behaviour over axial shortening mechanisms in linear friction welding of titanium alloys and modelling plasticisation effects, *Int. J. Mach. Tools Manuf.*, 2021, 161, 103674.

[116] X. Wang, W. Li, T. Ma, *et al.*, Characterisation studies of linear friction welded titanium joints, *Mater. Des.*, 2017, 116, 115-126.

[117] H. Li, S. Yang, S. Zhang, *et al.*, Microstructure evolution and mechanical properties of friction stir welding super-austenitic stainless steel S32654, *Mater. Des.*, 2017, 118, 207-217.

[118] F. Liu, Y. Hovanski, M. P. Miles, *et al.*, A review of friction stir welding of steels: Tool, material flow, microstructure, and properties, *J. Mater. Sci. Technol.*, 2018, 34(1), 39-57.

[119] P. Asadi, R. A. Mahdavinejad, & S. Tutunchilar, Simulation and experimental investigation of FSP of AZ91 magnesium alloy, *Mater. Sci. Eng. A*, 2011, 528(21), 6469-6477.

[120] G. Buffa, L. Fratini, M. Schneider, *et al.*, Micro and macro mechanical characterization of friction stir welded Ti-6Al-4V lap joints through experiments and numerical simulation, *J. Mater. Process. Technol.*, 2013, 213(12), 2312-2322.

[121] P. Zolghadr, M. Akbari, & P. Asadi, Formation of thermo-mechanically affected zone in friction stir welding, *Mater. Res. Express*, 2019, 6(8), 086558.

[122] R. Kuroiwa, H. Liu, Y. Aoki, *et al.*, Microstructure control of medium carbon steel joints by low-temperature linear friction welding, *Sci. Technol. Weld. Join.*, 2020, 25(1), 1-9.

[123] I. Bhamji, M. Preuss, P. L. Threadgill, *et al.*, Linear friction welding of AISI 316L stainless steel, *Mater. Sci. Eng. A*, 2010, 528(2), 680-690.

[124] Y. Su, W. Li, X. Wang, *et al.*, The sensitivity analysis of microstructure and mechanical properties to welding parameters for linear friction welded rail steel joints, *Mater. Sci. Eng. A*, 2019, 764, 138251.

[125] P. Paillard, E. Bertrand, M. Allart, *et al.*, Microstructure, mechanical properties and microtexture of friction stir welded S690QL high yield steel, *Mater. Charact.*, 2016, 122, 183-188.

[126] P. K. Chaurasia, C. Pandey, A. Giri, *et al.*, A comparative study of residual stress and mechanical properties for fsw and tig weld on structural steel, *Arch. Metall. Mater.*, 2018, 63(2), 1019-1029.

[127] G. Sharma & D. K. Dwivedi, Structure and properties of friction stir weld joints of structural steel, *Trans. Indian Inst. Met.*, 2017, 70(1), 201-208.

[128] Y. Li, Y. Liu, C. Liu, *et al.*, Microstructure evolution and mechanical properties of linear friction welded S31042 heat-resistant steel, *J. Mater. Sci. Technol.*, 2018, 34(4), 653-659.

[129] P. Geng, G. Qin, J. Zhou, *et al.*, Nonuniformity in mechanical properties of linear friction welded mild steel joint, *J. Mater. Eng. Perform.*, 2019, 28(3), 1827-1841.

[130] A. P. Reynolds, W. Tang, T. Gnaupel-Herold, *et al.*, Structure, properties, and residual stress of 304L stainless steel friction stir welds, *Scr. Mater.*, 2003, 48(9), 1289-1294.

[131] ASM International, *ASM Handbook, Welding, Brazing and Soldering*, 1995.

[132] Y. S. Lim, S. H. Kim, & K. J. Lee, Effect of residual stress on the mechanical properties of FSW joints with SUS409l, *Adv. Mater. Sci. Eng.*, 2018, 9890234.

[133] S. A. A. Akbari Mousavi & R. Miresmaeili, Experimental and numerical analyses of residual stress distributions in TIG welding process for 304L stainless steel, *J. Mater. Process. Technol.*, 2008, 208(1), 383-394.

[134] S. Ragu Nathan, V. Balasubramanian, S. Malarvizhi, *et al.*, Effect of welding processes on mechanical and microstructural characteristics of high strength low alloy naval grade steel joints, *Def. Technol.*, 2015, 11(3), 308-317.

[135] G. Sorger, T. Sarikka, P. Vilaça, *et al.*, Effect of processing temperatures on the properties of a high-strength steel welded by FSW, *Weld. World*, 2018, 62(6), 1173-

1185.

[136] J. Beaudet, G. Rückert, & F. Cortial, Fatigue behavior of FSW high-yield strength steel welds for shipbuilding application, *Weld. World*, 2020, 72(4), 407-420.

[137] W. Wang, R. Xu, Y. Hao, *et al.*, Corrosion fatigue behavior of friction stir processed interstitial free steel, *J. Mater. Sci. Technol.*, 2018, 34(1), 148-156.

[138] H. Polezhayeva, A. I. Toumpis, A. M. Galloway, *et al.*, Fatigue performance of friction stir welded marine grade steel, *Int. J. Fatigue*, 2015, 81, 162-170.

[139] A. K. Lakshminarayanan & V. Balasubramanian, Assessment of fatigue life and crack growth resistance of friction stir welded AISI 409M ferritic stainless steel joints, *Mater. Sci. Eng. A*, 2012, 539, 143-153.

[140] S. Rajan, P. Wanjara, J. Gholipour, *et al.*, Fatigue behavior of linear friction welded Ti-6Al-4V and Ti-6Al-2Sn-4Zr-2Mo-0.1Si dissimilar welds, *Materials (Basel).*, 2021, 14(11), 3136.

[141] J. M. García, F. Gaslain, & T. F. Morgeneyer, Materials characterization on the effect of a thermal treatment on the tensile and fatigue properties of weak zones of similar Ti17 linear friction welded joints and parent material, *Mater. Charact.*, 2020, 169, 110570.

[142] G. Wen, W. Li, S. Wang, *et al.*, Strain-controlled fatigue properties of linear friction welded dissimilar joints between Ti-6Al-4V and Ti-6.5Al-3.5Mo-1.5Zr-0.3Si alloys, *Mater. Sci. Eng. A*, 2014, 612, 80-88.

[143] D. S. Lachowicz, C. T. Lachowicz, R. Gil, *et al.*, Characterisation of joint properties through spatial mapping of cracks in fatigue specimens, extracted from the linearly friction welded steel coupon, *Precis. Eng.*, 2021, 71, 78-89.

[144] M. Raffi, G. Madhusudhan Reddy, & K. Srinivasa Rao, Microstructure and pitting corrosion of shielded metal arc welded high nitrogen stainless steel, *Def. Technol.*, 2015, 11(3), 237-243.

[145] T. Kawakubo, K. Ushioda, & H. Fujii, Grain boundary segregation and toughness of friction-stir-welded high-phosphorus weathering steel, *Mater. Sci. Eng. A*, 2022, 832, 142350.

[146] Japanese Industrial Standard Committee, *Metallic materials -Tensile testing -Method of*

test at room temperature. JISZ2241, 2022. (In Japanese)

[147] Y. Wang, S. Tsutsumi, T. Kawakubo, *et al.*, Microstructure, mechanical properties and fatigue behaviors of linear friction welded weathering steels, *Int. J. Fatigue*, 2022, 159, 106829.

[148] Y. Wang, S. Tsutsumi, T. Kawakubo, *et al.*, Microstructure and mechanical properties of weathering mild steel joined by friction stir welding, *Mater. Sci. Eng. A*, 2021, 823, 141715.

[149] Y. Wang, S. Tsutsumi, T. Kawakubo, *et al.*, Fatigue performance of friction stir welded weathering mild steels joined below A1 temperature, *Int. J. Fatigue*, 2022, 156, 106667.

[150] J. T. Busby, M. C. Hash, & G. S. Was, The relationship between hardness and yield stress in irradiated austenitic and ferritic steels, *J. Nucl. Mater.*, 2005, 336, 267-278.

[151] A. F. Hobbacher, *Recommendations for fatigue design of welded joints and components*, Springer, 2016.

[152] G. Sorger, E. Lehtimäki, S. Hurme, *et al.*, Microstructure and fatigue properties of friction stir welded high-strength steel plates, *Sci. Technol. Weld. Join.*, 2018, 23(5), 380-386.

[153] S. Anandavijayan, A. Mehmanparast, J. Braithwaite, *et al.*, Material pre-straining effects on fatigue behaviour of S355 structural steel, *J. Constr. Steel Res.*, 2021, 183, 106707.

[154] Á. Dobosy & J. Lukács, Welding properties and fatigue resistance of S690QL high strength steels, *Mater. Sci. Forum*, 2015, 812, 29-34.

[155] A. I. Dmitriev, E. A. Kolubaev, A. Y. Nikonov, *et al.*, Study patterns of microstructure formation during friction stir welding, *Proc. XLII Int. Summer Sch. APM 2014*, 10-16.

[156] H. B. Sun, F. Yoshida, M. Ohmori, *et al.*, Effect of strain rate on Lüders band propagating velocity and Lüders strain for annealed mild steel under uniaxial tension, *Mater. Lett.*, 2003, 57(29), 4535-4539.

Achievements

Publications related to this study

[1] **Wang, Y.**, Tsutsumi, S.*, Kawakubo, T., Fujii, H. (2022). Microstructure, mechanical properties and fatigue behaviors of linear friction welded weathering steels. *International Journal of Fatigue*, 159, 106829.

[2] **Wang, Y.**, Tsutsumi, S.*, Kawakubo, T., & Fujii, H. (2022). Fatigue performance of friction stir welded weathering mild steels joined below A1 temperature. *International Journal of Fatigue*, 156, 106667.

[3] **Wang, Y.***, Tsutsumi, S., Kawakubo, T., & Fujii, H. (2021). Microstructure and mechanical properties of weathering mild steel joined by friction stir welding. *Materials Science and Engineering: A*, 823, 141715.

[4] **Wang, Y.**, Tsutsumi, S.*, Kawakubo, T., & Fujii, H. (2022). Effects of phosphorus content on fatigue performance of friction stir welded mild steels. *Construction and Building Materials*, 324, 126682.

[5] **Wang, Y.***, Tsutsumi, S., Kawakubo, T., & Fujii, H. (2022). Microstructure and mechanical properties of friction stir welded high phosphorus weathering steel. *Science and Technology of Welding and Joining*, 27(5), 388-397.

[6] **Wang, Y.**, Tsutsumi, S.*, Kawakubo, T., Fujii, H. (2022). Fatigue strength and fracture characteristics of linear friction welded joints of weathering mild steel. *Fatigue & Fracture of Engineering Materials & Structures*. (Online)

Presentations

(International conferences)

[1] **Wang, Y.**, Tsutsumi, S., Fu Zhongqiu., Effects of repair weld on the deck-to-vertical stiffener joint after fatigue cracking. In *The 8th International Conference of Welding Science and Engineering*, Nov 21-22, 2019 (MCJW-5).

[2] **Wang, Y.**, Tsutsumi, S., Fatigue life extension by additional weld and its assessment by high-performance SCF formula considering spline bead profile. In *IIW2021 On-line Assembly and International Conference*, Jul 7-21, 2021 (XIII-2907-2021).

(Domestic conferences)

[3] **Wang, Y.**, Tsutsumi, S., Parametric formula for stress concentration factor of fillet weld joints with spline bead shape. In *令和 2 年度土木学会全国大会年次学術講演会*. 一般社団法人 土木学会, Sep 9-11, 2020

Acknowledgments

Firstly, I would like to express my sincere gratitude to my supervisor Prof. Seiichiro Tsutsumi for offering me an international and competitive research environment and for his inspiring guidance and steady support to my Ph.D. study and related research. I am particularly grateful to Prof. Riccardo Fincato for his continuous support and encouragement.

Likewise, I would like to thank my dissertation committee members: Prof. Toshiro Kamada and Prof. Toru Inui, for their valuable suggestions and inspiring comments, as well as for asking inspiring questions that incented me to broaden my research from multiple perspectives.

I would like to thank Prof. Hidetoshi Fujii and Dr. Takumi Kawakubo for their technical support and professional advice on my research and publication activities. I thank all the members and alumni of Tsutsumi Laboratory, Dr. Pengjun Luo, Mr. Bo Li, Ms. Yunwen Guan, Mr. Qingzhi Yao, Mr. Ayan Burlihan, Mr. Gaku Daimon, Mr. Koyo Takata, Mr. Hirokazu Nagahama, Mr. Homare Shibata and Mr. Yuki Kiyokawa. Without their support and assistance, it would be impossible to complete this research. There are probably many more of my friends and colleagues who are not mentioned in the acknowledgments. I also want to thank you for every moment I spent with you, and I sincerely ask for your understanding.

I would also like to thank China Scholarship Council for granting me the scholarship (201906710058) which supports my daily life, and Osaka University for exemption of tuition fee which saves me from economic worries.

Last but not least, I would love to thank my family for inspiring me to realize my own potential and supporting me materially and spiritually throughout my life. All the encouragement, support, and love they have given me over the years are what have allowed me to pursue my dream.